PHOTOACOUSTIC SIGNAL DETECTION VIA ATOMIC FORCE MICROSCOPY CANTILEVERS

by

Aytaç Demirkıran

B.S., Physics, Yıldız Technical University, 2007,

M.S., Physics, Boğaziçi University, 2012

Submitted to the Institute for Graduate Studies in
Science and Engineering in partial fulfillment of
the requirements for the degree of
Doctor of Philosophy

Graduate Program in Physics

Boğaziçi University

2018

ACKNOWLEDGEMENTS

Despite all of the challenging moments, I have accomplished to complete my thesis and closed one chapter of my life which has been very didactic in all the aspects. During this journey I have had a lot of support from various companies some longer than others. First and foremost, I would like to express my sincere gratitude to my advisor Prof. Mehmet Burçin Ünlü who has never deprived himself from his students. I appreciate all his contributions of time, ideas, and funding to make my Ph.D. experience productive and stimulating. I would also like to thank Dr. Hakan Erkol for helping me solving problems both in my thesis and in my life. Luckily, I also had great people who accompanied me in the research lab. Nasire Uluç and Esra Aytaç-Kipergil have always supported me both as colleagues but mostly as friends and family.

My sincere thanks also goes to Agah Karakuzu for hours long Skype discussions, for his continues support in our researches and mostly for his exceptional sense of humor. I would like to acknowledge Prof. Hamdi Torun for guiding me while the AFM system was built, I also would like thank Luying Feng and Sevil Özer for helping me to build the AFM system, and Dr. Seydi Yavaş, Dr. Uğur Parlatan for their help, guidance and consultancy, and all the rest of my fellow labmates for their continues help. I thank Prof. Nesrin Özören and Açelya Yılmazer for providing the cancer cells.

Also, I would like to thank TUBITAK (Grant No: 213E033), Ministry of Development (Project No: 2009K120520), Boğaziçi University Research funding (Grant No: BAP 15B03TUG3) for letting us create an environment where our researches flourish and funding our projects to be able to move forward.

Last but not least, I would like to thank my family and friends and also my colleagues from outside of this university for being there for me in the good, in the bad and in the ugly. Also for helping me control my stress levels at minimum and my sanity preserved.

ABSTRACT

PHOTOACOUSTIC SIGNAL DETECTION VIA ATOMIC FORCE MICROSCOPY CANTILEVERS

In this thesis, we first present a custom-designed photoacoustic microscopy system (PAM) which includes two separate excitation lasers. One of these tools is a novel fiber-based laser system developed particularly for multiwavelength optical resolution photoacoustic microscopy. The fiber laser has adjustable properties including pulse duration (5-10 ns), pulse energy (up to 10 μJ) and repetition frequency (up to 1 MHz) independently from each other. The whole laser system covers a broad spectral region from 450 to 1100 nm by its supercontinuum output and also can emit wavelengths of 532, 355, and 266 nm from its harmonic generation unit. The other laser source in the PAM system is a commercial tunable optical parametric oscillator (OPO) laser. The lateral resolution of the PAM system is approximately 2 μm. We present various biological (horse hair, human red blood cells, Skmel-28 cancer cells) and non-biological (resolution test target, India inks, cadmium telluride quantum dots) photoacoustic images obtained with our PAM system. In addition, we present a custom-developed atomic force microscopy (AFM) head to detect both acoustic and photoacoustic signals using microcantilevers as the pressure sensor. Here, as a preliminary study for the AFM-head system, we analyzed microcantilevers to investigate their responses to pulsed-laser-induced photoacoustic waves. The results indicate that microcantilevers can be used as photoacoustic detection tools by presenting steady-state oscillations when the repetition frequency of the excitation laser matches to the resonant frequency of the cantilever. Finally, for the proof-of-concept studies, we utilized the AFM-head system to detect acoustic waves at various frequencies arising from a personal headset, and also photoacoustic waves from a black ink phantom illuminated by the OPO laser. The AFM-head system is compact, portable, and very sensitive to external forces.

ÖZET

ATOMİK KUVVET MİKROSKOBU MANİVELALARI İLE FOTOAKUSTİK SİNYAL ÖLÇÜMÜ

Bu tezde, öncelikli olarak, içinde iki ayrı fotoakustik uyarma lazeri bulunan özel tasarlanmış bir fotoakustik mikroskop (PAM) sistemi sunmaktayız. Birinci lazeri orijinal fiber tabanlı bir lazerdir ve özellikle çok dalgaboylu optik çözünürlüklü PAM için geliştirilmiştir. Bu fiber lazer atım süresi (5-10 ns), atım enerjisi (10 μJ'e kadar), ve atım tekrar sıklığı (1 MHz'e kadar) gibi birbirlerinden bağımsız şekilde değiştirilebilen özelliklere sahiptir. Bütün lazer sistemi ise 1064 nm dalgaboyundan genişletilmiş 450 ile 1100 nm arasını, ve ayrıca harmonik üretme modülünden üretilen 532, 355 ve 266 nm çıkışlarını kapsamaktadır. PAM sistemindeki diğer lazer ise dalgaboyu ayarlanabilenen ticari bir optik parametrik salınıcı (OPO) lazerdir. PAM sistemimiz yaklaşık 2 μm yanal çözünürlüğe sahiptir. Ayrıca, PAM sistemimiz ile elde ettiğimiz çeşitli biyolojik (at kılı, insan kan hücreleri, Skmel-28 kanser hücreleri) ve biyolojik olmayan (çözünürlük test hedefi, çeşitli reklerdeki Hint boyası, cadmium telluride kuantum dotları) fotoakustik görüntüleri sunmaktayız. Ayrıca, akustik ve fotoakustik sinyalleri mikromanivelalarla ölçmek için özel olarak geliştirilmiş bir atomik kuvvet mikroskop (AFM) başlığı da sunmaktayız. Bu hedefin bir ön çalışması olarak, darbeli lazer ile üretilmiş fotoakustik dalgaların, mikromanivelaların salınımı üzerindeki etkilerini incelemekteyiz. Sonuçlarımız micromanivelaların iyi bir fotoakustik sensör olarak kullanılabileceğini, hatta fotoakustik uyarma lazerininin atım tekrar sıklığı manivelanın rezonans frekansına eşit veya yakın değerdeyse, kararlı durum salınımları oluşturulabileceğini göstermektedir. En sonunda, kavram ispatı için, bir kulaklık ile gönderilen farklı frekanslardaki akustik dalgaları ve bir siyah boya örneğinden OPO lazer ile üretilen fotoakustik dalgaları geliştirmiş olduğumuz AFM başlığını kullanarak ölçtük. Bu AFM başlık sistemi kompakt, taşınabilir, ve dış kuvvetleri ölçmede çok hassastır.

TABLE OF CONTENTS

ACKNOWLEDGEMENTS iii
ABSTRACT iv
ÖZET v
LIST OF FIGURES viii
LIST OF TABLES xvi
LIST OF SYMBOLS xvii
LIST OF ACRONYMS/ABBREVIATIONS xx
1. INTRODUCTION 1
1.1. Laser Sources Used for Photoacoustic Excitation 2
1.2. The OPO Laser Used in This Thesis For Photoacoustic Excitation . . . 4
1.3. Thesis Statement 8
2. THEORETICAL BACKGROUND OF PHOTOACOUSTIC PHENOMENON 10
2.1. Initial Photoacoustic Pressure 10
2.2. Derivation of the Photoacoustic Wave Equation 12
2.3. Solution of the Photoacoustic Wave Equation for the Dirac Delta Pulse Excitation 14
2.4. Generation of the Photoacoustic Wave From a Spherical Absorber . . . 15
3. DEVELOPMENT OF A NOVEL FIBER LASER WITH INDEPENDENTLY ADJUSTABLE PROPERTIES FOR OPTICAL RESOLUTION PHOTOACOUSTIC MICROSCOPY 21
3.1. Methods 21
3.1.1. Oscillator and Preamplifier 22
3.1.2. Supercontinuum Generation 23
3.1.3. Harmonic Generation 25
3.2. Discussion 30
4. BUILDING A CUSTOM-DESIGNED PHOTOACOUSTIC MICROSCOPY SYSTEM 38
4.1. Photoacoustic Signal Generation: Preliminary Studies 38
4.2. Lateral Resolution of the PAM System 42

4.3. Multispectral PAM Applications 42
4.4. Discussion 53
5. MICROCANTILEVERS EXCITED BY PULSED-LASER-INDUCED PHOTOACOUSTIC WAVES 54
5.1. Theory and Method 56
5.1.1. The Creation of Consecutive Photoacoustic Waves 57
5.1.2. Microcantilevers Driven by Photoacoustic Pressure 57
5.1.3. Oscillating Cantilever in a Viscous Fluid 60
5.2. Results 62
5.3. Discussion 67
6. DEVELOPMENT OF A CUSTOM-DESIGNED ATOMIC FORCE MICROSCOPY HEAD FOR ACOUSTIC AND PHOTOACOUSTIC SIGNAL DETECTION 70
6.1. Materials and Methods 70
6.2. Sound Wave Detection Using the AFM-head System 72
6.3. Photoacoustic Signal Detection Using the AFM-head System 77
6.3.1. Sample Preparation 77
6.3.2. Experimental Setup 78
6.3.3. Air-coupled Photoacoustic Detection 80
6.3.4. Water-coupled Photoacoustic Detection 82
6.4. Discussion 84
7. CONCLUSION 86
REFERENCES 89

LIST OF FIGURES

Figure 1.1. The photograph of the experimental setup in which a commercial optical parametric oscillator (OPO) laser is used as the photoacoustic excitation source. 5

Figure 1.2. (a) The photography of the inside part of the OPO box, (b) The layout of the inside part by specifying the locations of the optics (This figure was taken from the manual of the laser). 6

Figure 2.1. The characteristic N-shaped photoacoustic waves generated from spherical absorbers by delta heating for 1, 25, 50, 100, and 250 μm in radius for an initial pressure of $p_0 = 75$ Pa, and at distance of $r = 8R$, (a)-(e) in air and (f)-(j) in water, respectively. PA: Photoacoustic. 16

Figure 2.2. The FFTs of the N-shaped photoacoustic waves generated from spherical absorbers by delta heating for 1, 25, 50, 100, and 250 μm in radius for an initial pressure of $p_0 = 75$ Pa, and at distance of $r = 8R$, (a)-(e) in air and (f)-(j) in water, respectively, indicating the broadband frequency spectrum. 18

Figure 2.3. (a) The characteristic N-shaped photoacoustic waves generated from a spherical light absorber of $R = 250$ μm for $p_0 = 75$ Pa. The amplitude of the photoacoustic wave decays with distance with respect to inverse distance law (see Equation 2.28), (b) Normalized power spectral density of this photoacoustic wave. 20

Figure 3.1. The schematic of the oscillator and preamplifier parts of the laser. SM: Single mode (fiber), FPGA: Field-programmable gate array, WDM: Wavelength division multiplexer, and ASE: Amplified spontaneous emission. 22

Figure 3.2. The schematic of the supercontinuum generation part of the fiber laser. 23

Figure 3.3. Optical spectrum of the supercontinuum output of the fiber laser measured by two optical spectrum analyzers (OSA) with different wavelength ranges; OSA 1 (Avaspec-3648-VIS, Avantes) and OSA 2 (QE65 Pro, Ocean Optics). The acquired spectra were digitally combined in a single figure. 24

Figure 3.4. The schematic of the amplifier just before the harmonic generation unit. MPC: Multi-mode pump combiner. 25

Figure 3.5. (a) Optical spectrum, (b) Temporal profile of a typical pulse at the end of PM-DC-Yb fiber. 26

Figure 3.6. The schematic of the harmonic generation unit. FM: Filiping mirror, DM: Dichroic mirror. 27

Figure 3.7. (a) Optical spectrum of the SHG output acquired by OSA 2, (b) The THG output acquired by OSA 1. 28

Figure 3.8. The photographies of the outputs of (a) the supercontinuum, and (b) the harmonic generation unit of the laser. 28

Figure 4.1. The schematic of the experimental setup of the PAM system. The tunable fiber-based laser and OPO laser are co-aligned in a same optical path through sample in which any of them could be made passive with the help of a flipping mirror when requested. 39

Figure 4.2. The screenshot of the DAQ indicating the photoacoustic signal generated from an ink-loaded fiber tube phantom. 40

Figure 4.3. A photoacoustic signal generated from a horse tail-hair with a diameter of 350 μm illuminated by a laser pulse. 40

Figure 4.4. (a) The photography of a phantom including two horse tail-hairs to form a cross shape, (b) The photoacoustic image of the phantom illuminated with an optical wavelength of 1064 nm, power of 5 mW, a number of averaging of 16. 41

Figure 4.5. (a) Optical microscopy image, (b) Photoacoustic microscopy image of USAF resolution test target (Group 6 and 7), (c) Photoacoustic microscopy image of Group 7 Element 6, (d) FWHM of a line at Group 7 Element 6 from Gaussian fit (blue) of raw data (black). 43

Figure 4.6. The photoacoustic image of Group 5 Element 6 scanned within an area of 56 x 101 μm^2 with steps of 1 μm acquired at optical wavelength (a) 532 nm from harmonic generation unit, (b) 650 nm, (c) 697 nm, (d) 732 nm, (e) 785 nm, and (f) 880 nm, respectively, from supercontinuum output. 43

Figure 4.7. The photoacoustic images of the phantoms comprising multiple polymide tubes filled with India inks of various colors (red, black, and green, respectively) with three different optical wavelengths of (a) 1064 nm, (b) 650 nm, and (c) 590 nm. 44

Figure 4.8. The photoacoustic image of the cadmium telluride (CdTe) quantum dots (in toluene) injected on a microscope well slide. The whiter region shows the quantum dots. The quantum dots are aggregated around the circular boundary of the well due to their aggregation property. 45

Figure 4.9. The photographies of the PDMS phantoms with different thicknesses (1 mm and 6 mm). 46

Figure 4.10. The photographies of the microchannels inside the PDMS phantoms. 46

Figure 4.11. Photoacoustic image of a microfluidic device in PDMS phantom injected with a black India ink. The optical wavelength is at 1064 nm filtered from the supercontinuum output. The imaging area is 4x1 mm^2. 47

Figure 4.12. (a) The photoacoustic, (b) CCD, and (c) Optical microscopy image of red blood cells injected in a microchannel created in a PDMS phantom. 47

Figure 4.13. (a) The photography of a PDMS phantom including six microchannels. Optical images of (b) 3^{rd} (Skmel-28 with 30x10^6 cells/ml), (c) 4^{th} (black ink), and (d) 5^{th} (Skmel-28 with 20x10^6 cells/ml) channel. Comparative signals for (e) 3^{rd} and 5^{th} and (f) 3^{rd} and 4^{th} channel, taken at 532 nm with 50 mW power. 48

Figure 4.14. (a) The noise in the system. The photoacoustic signals arising from Skmel-28 cells (mixed with PBS) injected in an agar phantom excited by the OPO laser at 630 nm for pulse energies of (b) 1 μJ and (2) 5 μJ. 49

Figure 4.15. The relative photoacoustic images of two wells inside an agar phantom, one of them belongs to (a) PBS and the other belongs to Skmel-28 cells mixed with PBS. 51

Figure 4.16. (a) Photography of human red blood cells inside a microtiter embedded in an agarose gel phantom, (b) Optical microscopy image, (c) Photoacoustic image of the region of interest, taken with an optical wavelength of 630 nm at 1 μJ using the OPO laser. 52

Figure 5.1. (a) The characteristic N-shaped photoacoustic waves generated from a spherical light absorber of $R = 250$ μm in radius for $p_0 = 75$ Pa. The amplitude of the photoacoustic wave decays with distance with respect to inverse distance law (see Equation 2.28), (b) Normalized power spectral density of this photoacoustic wave. 56

Figure 5.2. Two examples of numerically created consecutive photoacoustic waves comprising (a) 5 and (b) 50 waves, which are generated by a 100 kHz excitation laser for the values of $p_0 = 75$ Pa, $R = 250$ μm, and $r = 2R$. PA: Photoacoustic, PRP: Pulse repetition period. 57

Figure 5.3. Schematic illustration of the setup for the microcantilever excitation by pulsed-laser-induced photoacoustic waves generated from a spherical light absorber. 59

Figure 5.4. (a)-(b) Random oscillations of the cantilevers in time domain modeled by the Gaussian white noise with an RMS value of approximately 1 nm, (c)-(d) the corresponding normalized power spectral densities calculated by taking the FFT of these time domain random oscillations. PA: Photoacoustic. 62

Figure 5.5. (a)-(b) The responses of the cantilevers to the consecutive photoacoustic waves when the PRF of the excitation laser matches to the fundamental resonant frequency, (c)-(d) the corresponding normalized power spectral densities calculated by taking the FFT of these time domain oscillations. PRF: Pulse repetition frequency. 63

Figure 5.6. (a)-(b) Frequency response curves corresponding to the fundamental resonant frequencies and their lower harmonics up to 3^{rd} order for C1 and C2, respectively, (c) the time domain oscillations of C1 up to 0.4 ms driven by f_0, f_1, f_2, and f_3, in which the colored arrows show the inclusion of the photoacoustic waves. 64

Figure 5.7. (a)-(b) The responses of the cantilevers to the consecutive photoacoustic waves with a repetition frequency of 150 kHz that does not match to any harmonic values of both cantilevers, (c)-(d) the corresponding normalized power spectral densities calculated by taking the FFT of these time domain oscillations. 65

Figure 5.8. Frequency response curves of the microcantilevers simulated with and without noise. The correct positions for the vertical intersections for the data with noise were obtained by the data without noise. Then, the horizontal red lines correspond to $1/\sqrt{2}$ of the peak amplitude values of the curves. Q: Quality factor. 66

Figure 5.9. Oscillation amplitudes of the microcantilevers as a function of the distance between cantilever and the surface of the spherical absorber. 67

Figure 6.1. The photography of the AFM-head. 71

Figure 6.2. The photography of the AFM-head system for sound wave detection. 72

Figure 6.3. The responses of the microcantilever of ∼18 kHz to the various frequencies of sound waves arising from a headset. Maximum response occurs at 19 kHz. 74

Figure 6.4. The responses of the microcantilever of ∼15 kHz to the various frequencies of sound waves arising from a headset. Maximum response occurs at 14 kHz. 75

Figure 6.5. The black ink phantom used for photoacoustic generation in the AFM-head. 77

Figure 6.6. The schematic illustration of the experimental setup of photoacoustic signal detection by microcantilevers using our AFM-head system. 78

Figure 6.7. The screenshot image of the oscilloscope used for monitoring showing the values of the parameters, trigger signal, cantilever oscillation in the absence of photoacoustic waves (PA off). 79

Figure 6.8. Random oscillations of the microcantilever (∼15 kHz) in (a) air and (b) water with no averaging and 4 averaging. 79

Figure 6.9. Photoacoustic signals arising from black ink phantom detected in air medium by using the AFM-head. Here, the z-parameter stands for the distance between the ink surface and the microcantilever (14 kHz in air), and the pulse energy is 1 μJ at 630 nm. 81

Figure 6.10. Photoacoustic signals arising from black ink phantom detected by a microcantilever (14 kHz in air) in air medium by using the AFM-head at pulse energies of (a) 100 nJ, (b) 200 nJ, (c) 400 nJ, and (d) 1 μJ at 630 nm. The distance between the ink surface and the microcantilever was adjusted as 1 mm. 82

Figure 6.11. Photoacoustic signals arising from black ink phantom detected in water medium by using the AFM-head. Here, the z-parameter stands for the distance between the ink surface and the microcantilever (∼6 kHz in water), and the pulse energy is 1 μJ at 630 nm. 83

Figure 6.12. Photoacoustic signals arising from black ink phantom detected in water by a microcantilever (∼6 kHz in water) using the AFM-head at pulse energies of (a) 100 nJ, (b) 200 nJ, (c) 400 nJ, and (d) 600 nJ at 630 nm. The distance between the ink surface and the microcantilever was adjusted as 1 mm. 84

LIST OF TABLES

Table 1.1. The descriptions of the optic components in the layout of the OPO shown in Figure 1.2b. 7

Table 3.1. The output specifications of the laser. 29

Table 3.2. The average power and pulse energy values for several wavelengths filtered from the supercontinuum output of the fiber laser. 30

Table 3.3. Comparison of the output specifications of the lasers reported in the literature utilizing PCF to broaden the spectrum. 31

Table 3.4. Comparison of the output specifications of the lasers reported in the literature utilizing SRS or four-wave mixing techniques to obtain multiwavelength spectrum. 33

Table 3.5. Comparison of the output specifications of the fiber-based pump lasers reported in the literature in which SRS is used to obtain multiwavelength. PM-SMF: Polarization Maintaining Single Mode Fiber, PRF: Pulse repetition frequency. 35

Table 5.1. Cantilevers used for simulations. 61

LIST OF SYMBOLS

A_e	Specific optical absorption
A_{lever}	One-side surface area of cantilever
a_1, a_2, a_3, a_4	Parameters in hydrodynamic functions
C_P	Specific heat capacity at constant pressure
C_V	Specific heat capacity at constant volume
d_c	Characteristic dimension of the heated region
E	Young's modulus for cantilever material
F	Optical fluence
F_{PA}	Force due to photoacoustic pressure
f	Resonance frequency of cantilever
f_{fluid}	Resonance frequency of cantilever in viscous fluid
f_{vacuum}	Resonance frequency of cantilever in vacuum
G	Green's Function
H	Heating Function
h	Thickness of cantilever
k_{eff}	Effective spring constant of cantilever
L	Length of cantilever
m_{added}	Additional mass term
m_{eff}	Effective mass of cantilever
m_{lever}	Mass of cantilever
$P(t)$	Photoacoustic wave as a function of time t at a certain distance distance $\mathbf{r}$
p	Change in pressure
p_0	Initial photoacoustic pressure
$p(\mathbf{r}, t)$	Photoacoustic wave at distance $\mathbf{r}$ and time t
R	Radius
$\mathbf{r}$	Distance in three dimensions
r	Radial Distance
T	Change in temperature

U	Heaviside step function
t	Time
V	Volume
$\tilde{W}_N$	Gaussian white noise
w	Width of cantilever
x	Vertical displacement of the free end of cantilever
α_{th}	Thermal diffusivity
β	Thermal coefficient of volume expansion
Γ	Gruneisen parameter
Γ_{hydro}	Hydrodynamic function
Γ'	A parameter forming the real part of hydrodynamic function
Γ''	A parameter forming the complex part of hydrodynamic function
γ	Damping coefficient for cantilever
δ	A length parameter corresponding to fluid
$\delta(\mathbf{r}), \delta(t)$	Dirac delta functions
η	Fluid viscosity
η_{th}	Percentage of absorbed energy converted to heat
κ	Isothermal compressibility
λ	Wavelength
μ_a	Optical absorption coefficient
∇	Gradient
ξ	Medium displacement
ρ	Mass density
ρ_{fluid}	Density of fluid
ρ_{lever}	Density of cantilever material
τ_s	Stress relaxation time
τ_{pp}	Peak-to-peak interval of an N-shaped photoacoustic wave
τ_{th}	Thermal relaxation time
υ_s	Speed of sound
Φ	Optical fluence rate

ω_{fluid}	Angular frequency of cantilever in fluid

LIST OF ACRONYMS/ABBREVIATIONS

2D	Two Dimensional
3D	Three Dimensional
AFM	Atomic Force Microscopy
ASE	Amplified Spontaneous Emission
BBO	Barium Borate
CdTe	Cadmium Telluride
CCD	Charge Coupled Device
DAQ	Data Acquisition Card
DC	Double Clad
FFT	Fast Fourier Transform
FHG	Fourth Harmonic Generation
FPGA	Field Programmable Gate Array
FWHM	Full Width At Half Maximum
LBO	Lithium Triborate
LMA-PCF	Large Mode Area Photonic Crystal Fiber
MAP	Maximum Amplitude Projection
MOPA	Master Oscillator Power Amplifier
MPC	Multi-Mode Pump Combiner
NCPM	Non-Critical Phase Matching
Nd:YAG	Neodymium Yttrium Aluminum Garnet
OPO	Optical Parametric Oscillator
OR-PAM	Optical Resolution Photoacoustic Microscopy
OSA	Optical Spectrum Analyzer
PA	Photoacoustic
PAI	Photoacoustic Imaging
PAM	Photoacoustic Microscopy
PBS	Phosphate-Buffered Saline
PCF	Photonic Crystal Fiber

PDMS	Polydimethylsiloxanes
PM-SMF	Polarization Maintaining Single Mode Fiber
PRF	Pulse Repetition Frequency
PRP	Pulse Repetition Period
PSD	Power Spectral Density
RBCs	Red Blood Cells
ROI	Region of Interest
SHG	Second Harmonic Generation
SNR	Signal to Noise Ratio
SRS	Stimulated Raman Scattering
THG	Third Harmonic Generation
UV	Ultra Violet
WDM	Wavelength-Division Multiplexer
Yb	Yterrbium-doped

1. INTRODUCTION

Photoacoustic imaging (PAI) is an emerging modality which is based on an old phenomenon, called photoacoustic effect that was first presented by Alexander Graham Bell in 1880 [1]. Photoacoustic generation can be resulted from either intensity modulated continuous wave lasers [1–4], or pulsed lasers [5, 6]. The latter is a profoundly efficient [3, 7–9] method in the photoacoustic generation in which a short-pulsed laser is used to irradiate an optical absorber. Once the light is absorbed by the absorber, temperature increases followed by an adiabatic volume expansion. This expansion triggers a pressure wave out of the irradiated absorber, that is called the photoacoustic effect. Although the photoacoustic effect has been discovered long before, the improvements in ultrasonic detection methods, laser technologies, computers and image reconstruction algorithms, have made its application as an imaging modality. Today, PAI, which utilizes a non-ionizing radiation to produce photoacoustic waves, has become one of the fastest developing modality proving itself over the last decade by presenting from submicron resolution up to organelles [10–14], on the other hand, whole-body small animal imaging [15, 16] with a highly resolved brain mapping [17, 18].

High optical contrast and low acoustical scattering in tissue are the key factors for PAI owing to its hybrid nature combining the optical excitation with acoustic detection. Besides, image resolution and contrast of PAI depend primarily on the laser parameters used for photoacoustic excitation. Therefore, a laser needs to produce short enough pulses, i.e., several nanoseconds, in order to generate photoacoustic signals efficiently and emit wavelengths in the visible range covering the absorption peaks of tissue chromophores in their spectra [19–21]. To obtain adequate penetration depth, it is also desirable to utilize a wavelength in the near infrared range, from 600 to 1200 nm, where biological tissues are relatively transparent [22, 23].

In a PAI system, a precise detection of the photoacoustic signals is essential to acquire the correct image corresponding to the tissue characteristic. From this point of view, the improvement of the minimum detectable photoacoustic signal level is one of

the keys to broaden its boundaries. In the literature, ultrasonic waves generated by the photoacoustic effect are generally detected by various types of ultrasonic piezoelectric transducers [24–27] due to its availability and easy implementation in the system [28]. On the other hand, there are various types of optic-based ultrasound detection methods including Fabry-Perot polymer film sensor [29–32], optical resonator-based detections such as polymer ring resonators [33–36], silicon/silicon nitride ring resonator [37, 38], and fused silica microresonators [39, 40]. All of these methods basically aim at an ultrasound detection in a highly sensitive way providing low noise equivalent pressure.

1.1. Laser Sources Used for Photoacoustic Excitation

In literature, several kinds of lasers have been used for photoacoustic excitation. Pulsed laser diodes draw researchers' attention by being compact and inexpensive. While the peak power is relatively modest [22, 41], it is sufficient to obtain an adequate signal-to-noise ratio for in-vivo optical resolution photoacoustic microscopy (OR-PAM), as demonstrated in several publications [42–46]. On the other hand, they found only limited place in photoacoustic applications due to their lack of continuous tunability in wavelength. Q-switched Nd:YAG lasers operating at 1064 nm (and/or acquiring 532 nm by frequency doubling) are frequently utilized for PAM [22, 47]. They are generally preferred because of their easy accessibility. However, their fixed wavelength output is a serious drawback for multispectral photoacoustic applications which quantify unique spectral features of each absorber by a set of wavelengths. On the other hand, Q-switched Nd:YAG pumped dye lasers, Ti:Sapphire lasers, and optical parametric oscillators (OPOs) are usually preferred for providing necessary wavelength tuning with high pulse energies (>1 mJ) [21, 48–58]; yet, they have some major limitations of their practical applications such as having low pulse repetition rate (generally less than 50 Hz, recently up to several kHz for OPOs [59, 60]), being bulky and expensive, and requiring external cooling units [28].

In order to obtain better measurements, multiwavelength spectrum is obtained from a single wavelength emitting Q-switched Nd:YAG microchip laser, either through stimulated Raman scattering (SRS) or nonlinear broadening by coupling its output to

a fiber [61–70]. For lasers utilizing SRS, the major energy is distributed on a series of fixed individual wavelength peaks that result from the nonlinear interaction between incoming photons through the fiber and the molecules in the fiber itself, thus offers a limited wavelength tunability [71]. Koeplinger *et al.* [65] reported four bands in a polarization maintaining single mode fiber (PM-SMF), and Loya *et al.* [66] improved the system with a broader wavelength tuning range also with a higher repetition rate and pulse energy per band. It was also demonstrated that both discrete lines and a continuum can be produced by using four-wave mixing in a unique fiber (SMF-28e) [67]. As a different technique, Buma *et al.* [68] used a birefringent optical fiber and produced discrete spectral bands in near-infrared region.

Much broader wavelength tuning can potentially be achieved by a supercontinuum source such as photonic crystal fiber (PCF), which relies on spectral broadening through nonlinear processes [61, 72–74]. PCF is a silica optical fiber with an ordered array of microscopic air holes running along its length [75, 76]. Billeh *et al.* [61] utilized PCF for developing spectroscopic photoacoustic microscopy system. Lee *et al.* [62] also built a supercontinuum laser system for both PAM and optical coherence tomography. Afterwards, Lee *et al.* [63] determined oxygen saturation of hemoglobin and hemoglobin concentration via the same laser source. Whensoever the applications by coupling the output of Q-switched Nd:YAG microchip to PCF are considered, the energy per band is reported to be lower in supercontinuum case than SRS, which may be a drawback for many applications [71]. In order to achieve wider tunability in the wavelength with a high energy per band, Shu *et al.* [64] proposed a master oscillator power amplifier (MOPA) laser system with a homebuilt yterrbium-doped (Yb) fiber amplifier for a power boost. The amplifier was coupled to a specially designed PCF taper that connects a large-core fiber that has much more resistance to high-pulse energy at the input to a small-core PCF for spectrum broadening. Pulse energy per band increased dramatically and became comparable to the ones produced through SRS [64, 70].

Apart from wavelength tunability, a laser system with a high pulse repetition frequency (PRF) is also desired for fast image acquisition. The repetition frequencies of solid-state lasers are limited up to several kHz; but recently, fiber lasers with high

repetition rates emerge as an alternative excitation source for PAM. Through their high repetition rate, near real and real-time imaging can be achieved [71, 77–79]. It has already been reported that in comparison to conventional systems with solid state lasers, the ones with fiber lasers are at least two orders of magnitude faster without compromising lateral resolution [77, 80]. Fiber laser sources are also used for in vivo and in vitro studies also including flow cytometry applications [77, 79–83]. The main disadvantage of these systems is that their fixed wavelength does not allow for multispectral functional imaging. To overcome the limitations, a fiber laser technology seeking for tunability in wavelength is put forward. Hajireza *et al.* [84] developed an SRS fiber laser source for photoacoustic imaging. They coupled the output of a Yb fiber laser into a PM-SMF in varying lengths at different PRFs and extended the number of wavelengths at SRS peaks that were previously limited [71, 85]. In recent years, due to high power capabilities, MOPA laser systems have been developed [86–88]. The first demonstration of a short pulse MOPA fiber laser at 1 μm was the study by Ilday *et al.* [89]. Allen *et al.* [86] produced a fiber laser system with a high repetition frequency in MOPA configuration with a single emission wavelength of 1064 nm. Mahmud *et al.* [87] demonstrated an OR-PAM system by using a commercial picosecond MOPA laser system consisting of a fiber-based tunable oscillator and three amplifier stages with a high power booster amplifier. However, the wavelength tunability was limited with 50 nm bandwidth.

1.2. The OPO Laser Used in This Thesis For Photoacoustic Excitation

In this section, we give information about a commercial OPO laser (Continuum, Surelite II-10 Horizon I) which was used as the photoacoustic excitation source in our PAM system. The photography of the experimental setup is shown in Figure 1.1. The OPO system is pumped by a Q-switched pulsed Nd:YAG laser at 355 nm light. In fact, the Nd:YAG laser produces a high energy light at 1064 nm with a repetition frequency of 10 Hz, but the output is converted into 355 nm by harmonic generation processes using a doubling and tripling crystals located just before the output. Pulse energy, beam shape, precise alignment, output energy and wavelength are some of the key

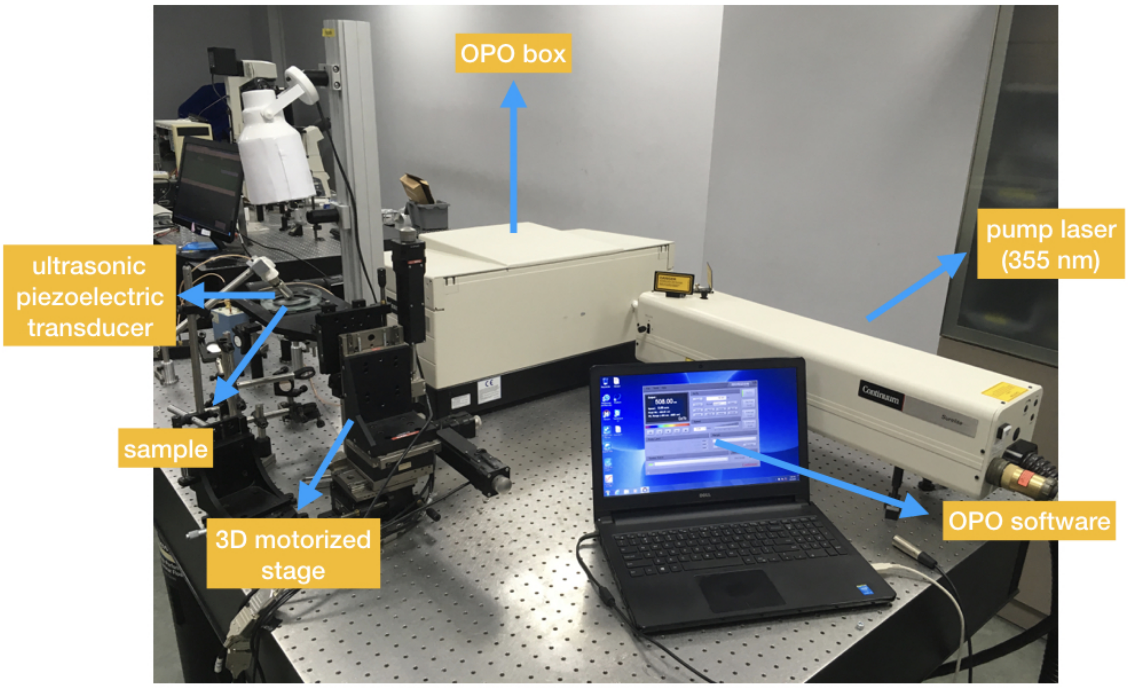
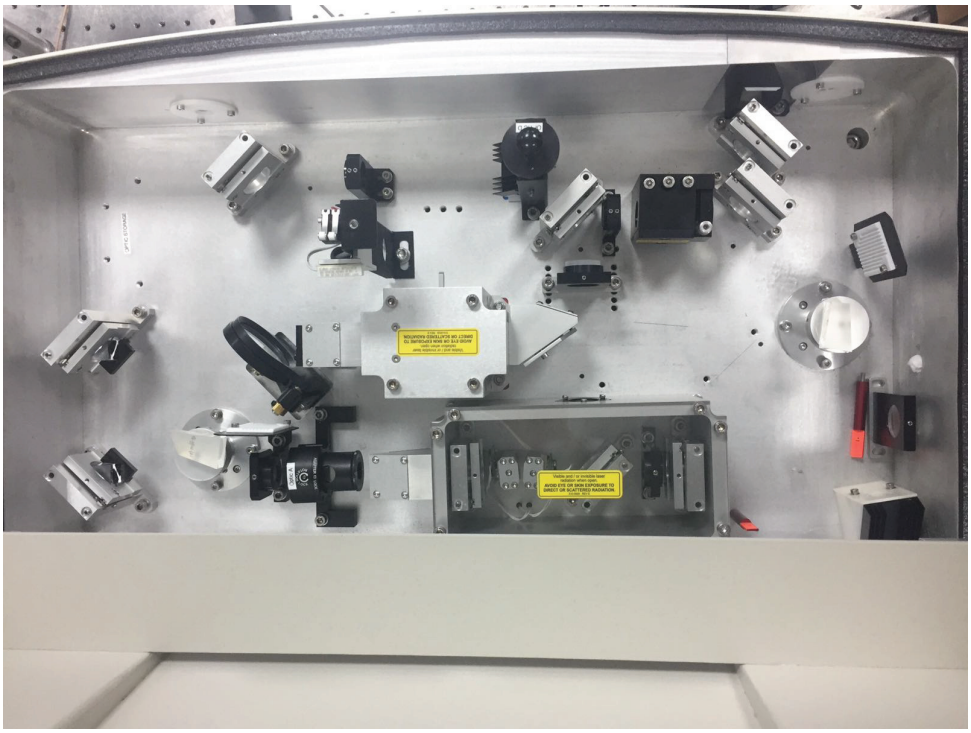


Figure 1.1. The photograph of the experimental setup in which a commercial optical parametric oscillator (OPO) laser is used as the photoacoustic excitation source.

factors for the performance of the OPO. In this connection, the pump laser produces coherent, ultrafast, and high peak power laser pulses within a good beam quality and proper alignment. Another critical parameter is the pulse-to-pulse stability that the dual pump pulses should have the same spatial overlap, energy, and symmetry. The pump laser provides these requirements. The Q-switched delay which can be adjusted by user is the basic parameter to increase or decrease the output energy. The energy adjustment is also possible by the voltage value, but it is not preferable. Two of the measured energy values from the output of the pump laser are 160 μJ and 190 μJ for Q-switched delays of 240 μs and 185 μs, respectively, at 355 nm and 10 Hz.

The OPO part is particularly designed to be pumped by the aforementioned N:YAG laser. The position and the leg adjustment of the OPO box are important for the alignment procedure. First, the pump light at 355 nm enters the OPO box from the

(a)



(b)

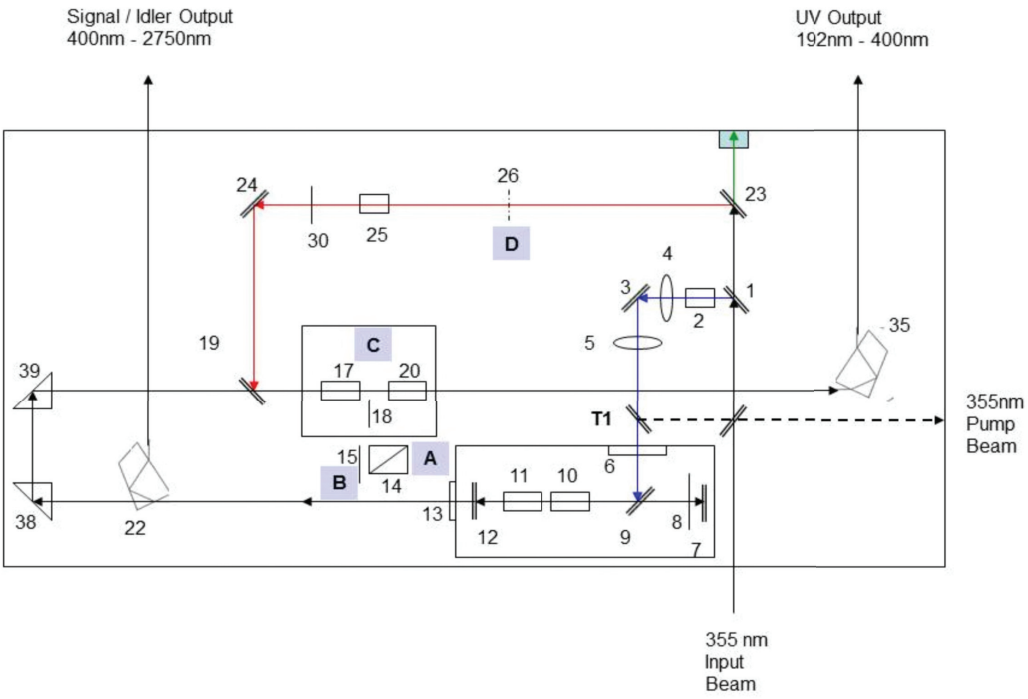


Figure 1.2. (a) The photography of the inside part of the OPO box, (b) The layout of the inside part by specifying the locations of the optics (This figure was taken from the manual of the laser).

Table 1.1. The descriptions of the optic components in the layout of the OPO shown in Figure 1.2b.

Item #	**Description**	**Item #**	**Description**
1, 3, T1	Mirror dichroics, 355 nm	16	Window
2a	Half wave plate (option)	17	Crystal, BBO
2b	Polarizer 355 nm (option)	18 (C)	Waveplate
4	Lens	19	Mirror
5	Lens	20	Crystal, BBO
6	Window	21	Window
7	Porro Prism	22	Pelin Broca
8	Half wave plate	23	Mirror
9	Injection pump mirror	24, 29	Mirror
10	#1 Crystal BBO Type 1	25a	Half wave plate
11	#2 Crystal BBO Type 1	25b	Polarizer
12	Mirror	30	Half wave plate
13	Window	26 (D)	Beam dump assy
14 (A)	Polarizer	35	Pelin Broca
15 (B)	Half wave plate	38, 39	Prism 90 deg

back input port. The precise alignment procedure of the OPO is performed with the help of two alignment jigs at various specified locations at low pulse energy (around 1 mJ). Figure 1.2a and Figure 1.2b show the photograph of the inside part of the box and the layout of the inside part by specifying the optics, respectively. The descriptions of the components inside the OPO box are given in Table 1.1. 355 nm light reaches the closed box OPO oscillator part passing through the some optical components such as dichroic mirrors, half-wave plate, and lenses. The oscillator part in the OPO includes two beta-barium borate (BBO) crystals which are controlled by motors. A wide range of wavelength between 400 nm and 2750 nm from the input of 355 nm is generated by utilizing these two BBO crystals. The calibration of the crystals and some other optics are advanced by computer control system using the OPO software. Additionally, the OPO has a closed box ultraviolet (UV) module including two other BBO crystals which

are also controlled by the software. The wavelength range of the UV output ranges between 192 nm and 400 nm. Some of the measured energy values from the relevant outputs of the OPO are 50 μJ, 8 μJ, 3 μJ, 2 μJ, and 1 μJ for the wavelengths of 425 nm, 340 nm, 260 nm, 220 nm, and 200 nm, respectively.

In this thesis, we use the aforementioned OPO laser system for photoacoustic excitation in the PAM system which is presented in Chapter 4. In the PAM system, we also use our custom-developed fiber laser which is presented in Chapter 3. Besides, the OPO laser is also used as the photoacoustic excitation source in the custom-designed atomic force microscopy (AFM) head system for photoacoustic signal detection presented in Chapter 6.

1.3. Thesis Statement

In Chapter 2, we review the theoretical background of the photoacoustic phenomenon including the derivation of the photoacoustic wave equation and its solutions. In the light of these analyses, we obtain information about the characteristic of the laser-induced photoacoustic waves. This chapter is essential because we use the solution and mention about its implications in the following chapters. Chapter 3 presents our custom fiber laser which is particularly developed for OR-PAM. This laser is unique and has adjustable parameters such as pulse repetition frequency between 65 kHz and 1 MHz, pulse duration between 5 ns and 10 ns, pulse energy up to 10 μJ, and wavelength between 450 nm and 1100 nm by its supercontinuum output, and 532 nm, 355 nm, and 266 nm from its harmonic generation unit by a separate output of 1064 nm. It is very compact, portable, relatively cheap, and do not require external cooling unit. Besides, when we take the low damage threshold of fibers into account, the output specifications of this laser from the supercontinuum output is remarkably high. The pulse energy values are higher than the PCF-coupled supercontinuum cases and comparable to the output values of specially designed fiber laser with tapered PCF cases mentioned in Section 1.1. Additionally, our laser system with high PRF provides fast imaging including in vivo real-time imaging, and its adjustability opens new application areas in which fixed PRF is undesirable. It is also largely immune to mechanical and thermal

perturbations as well as being misalignment free. All in all, our fiber laser having maximum flexibility on its parameters may pave the way for spectroscopic PAM applications via widely tunable fiber laser technologies. Subsequently, Chapter 4 comprises of our custom-designed PAM system in which the fiber laser and the OPO laser are used for photoacoustic excitation. Our PAM system is very stable so that we report a lateral resolution of around 2 μm and spectroscopic images by utilizing the supercontinuum output of the fiber laser. Herein, we also show various biological (horse hair, human red blood cells, Skmel28 cells) and non-biological (resolution test target, India inks, quantum dots) photoacoustic images obtained from our PAM system. The developed system is very useful for preclinical research studies requiring multiwavelength data within a good resolution. Chapter 5 presents investigations of microcantilevers excited by the photoacoustic waves induced by a pulsed-laser. This study is a requirement for our objective of photoacoustic signal detection utilizing microcantilevers as the photoacoustic sensor. At the same time, it is also essential for AFM actuation studies in which microcantilevers are excited by photoacoustic waves. Here, we investigate the cumulative effects of the consecutive photoacoustic waves on the oscillation of microcantilever. This study shows us microcantilevers can be excited by photoacoustic waves within steady-state oscillations when PRF matches to the fundamental resonant frequency of the microcantilever or equals to its lower harmonics. Following this study, in Chapter 6, we present custom-designed atomic force microscopy (AFM) head system providing the detection of both acoustic and photoacoustic signals both in air and water. In the former case, we use a headset to generate sound waves with various frequencies to observe the response of cantilever both in time and frequency domains. For the former case, we use a black ink phantom to generate photoacoustic waves upon cantilever in the AFM head. In these measurements, we present photoacoustic signals successfully detected via AFM cantilevers. We provide various results obtained both in air and water indicating the feasibility of our AFM-head system on photoacoustic signal detection.

2. THEORETICAL BACKGROUND OF PHOTOACOUSTIC PHENOMENON

2.1. Initial Photoacoustic Pressure

There are two important timescale factors in laser heating [5]. The first one is the *thermal relaxation time* determining the thermal diffusion, which is described by

$$\tau_{th} = \frac{d_c^2}{\alpha_{th}} \tag{2.1}$$

where α_{th} and d_c are the thermal diffusivity (m^2/s) and the characteristic dimension of the heated region, respectively. Here, this characteristic dimension d_c can be either the dimension of the structure of interest or the decay constant of the optical energy deposition depending on the fact that which one is smaller. The second one is the *stress relaxation time* characterizing the pressure propagation, that is given by

$$\tau_s = \frac{d_c}{\upsilon_s} \tag{2.2}$$

where υ_s is the speed of sound in the medium.

When the thermal relaxation time, τ_{th}, is much longer than the pulse duration of the laser, the excitation is in thermal confinement, and heat conduction can be ignored during the interaction of the absorber with the laser pulse. Similarly, when the stress relaxation time, τ_s, is much longer than the pulse duration, the excitation is in stress confinement. So, the stress propagation can be ignored during the interaction.

The fractional volume expansion, dV/V, due to the laser heating can be described by

$$\frac{dV}{V} = -\kappa p + \beta T \tag{2.3}$$

where κ, β, p, and T stand for the isothermal compressibility (Pa^{-1}), the thermal coefficient of volume expansion (K^{-1}), change in pressure (Pa), and change in temperature (K), respectively. The isothermal compressibility κ is given by

$$\kappa = \frac{C_P}{\rho v_s^2 C_V} \tag{2.4}$$

where ρ, C_P and C_V are the mass density (kg/m^3), the specific heat capacities at constant pressure and volume (J/(kgK)), respectively.

If there exist the thermal and stress confinements for the laser excitation, the fractional volume expansion can be ignored so that the local increase in pressure, p_0, just after the laser pulse can be obtained from Equation 2.3 as follows:

$$p_0 = \frac{\beta T}{\kappa}, \tag{2.5}$$

which can also be expressed as

$$p_0 = \frac{\beta}{\kappa \rho C_V} \eta_{th} A_e \tag{2.6}$$

where A_e and η_{th} are the specific optical absorption (J/m^3) and the percentage converted into heat, respectively. Here, the dimensionless Gruneisen parameter is defined by

$$\Gamma = \frac{\beta}{\kappa \rho C_V} = \frac{\beta v_s^2}{C_P}. \tag{2.7}$$

Combining Equation 2.6 with Equation 2.7 and using $A_e = \mu_a F$ yields

$$p_0 = \Gamma \eta_{th} \mu_a F \tag{2.8}$$

where μ_a and F are the optical absorption coefficient (mm^{-1}) and the optical fluence (J/cm^2), respectively.

2.2. Derivation of the Photoacoustic Wave Equation

There are two fundamental equations to derive the photoacoustic wave equation [5], which are thermal expansion equation (generalized Hooke's law)

$$\nabla \cdot \xi(\mathbf{r}, t) = -\kappa p(\mathbf{r}, t) + \beta T(\mathbf{r}, t), \tag{2.9}$$

and the linear inviscid force equation (the equation of motion)

$$\rho \frac{\partial^2}{\partial t^2} \xi(\mathbf{r}, t) = -\nabla p(\mathbf{r}, t), \tag{2.10}$$

respectively, where ξ is the medium displacement. The left-hand side of the thermal expansion equation (Equation 2.9) expresses the fractional volume expansion as the right-hand side of the equation includes the two factors which are related to the volume expansion. The left-hand side of the linear inviscid equation (Equation 2.10) describes the product of the mass density and the acceleration while the right-hand side of the equation describes the applied force per unit volume. Therefore, Equation 2.10 is indeed an expression of Newton's second law.

The divergence of Equation 2.9 and the substitution of this result into Equation 2.10 leads to

$$\frac{\partial^2}{\partial t^2}(-\kappa\rho p(\mathbf{r}, t) + \rho\beta T(\mathbf{r}, t)) = \nabla^2 p(\mathbf{r}, t). \tag{2.11}$$

Equation 2.11 takes the following form

$$(\nabla^2 - \frac{1}{\upsilon_s^2}\frac{\partial^2}{\partial t^2})p(\mathbf{r}, t) = -\rho\beta \frac{\partial^2}{\partial t^2} T(\mathbf{r}, t) \tag{2.12}$$

where $\upsilon_s = \frac{1}{\sqrt{\rho\kappa}}$. Therefore, we reach the photoacoustic wave equation by using $\rho = \frac{1}{\kappa\upsilon_s^2}$

$$(\nabla^2 - \frac{1}{\upsilon_s^2}\frac{\partial^2}{\partial t^2})p(\mathbf{r}, t) = -\frac{\beta}{\kappa\upsilon_s^2}\frac{\partial^2}{\partial t^2} T(\mathbf{r}, t) \tag{2.13}$$

which describes the propagation of the photoacoustic wave. The left hand side of Equation 2.12 represents the wave propagation while the right-hand side is the source term, where $p(\mathbf{r},t)$ and $T(\mathbf{r},t)$ are the photoacoustic wave and the temperature rise at position $\mathbf{r}$ and time t, respectively.

If a laser pulse is sufficiently short which satisfies the thermal confinement condition, the heat diffusion can be omitted so that the thermal equation becomes

$$\rho C_v \frac{\partial T(\mathbf{r},t)}{\partial t} = H(\mathbf{r},t) \tag{2.14}$$

where $H(\mathbf{r},t)$ is the heating function which describes the heat per unit volume and per unit time, and it is given by $H(\mathbf{r},t) = \eta_{th}\mu_a\Phi$ where Φ is the optical fluence rate. Then, by writing Equation 2.14 into Equation 2.12, the photoacoustic wave equation has the following form

$$(\nabla^2 - \frac{1}{v_s^2}\frac{\partial^2}{\partial t^2})p(\mathbf{r},t) = -\frac{\beta}{C_P}\frac{\partial H(\mathbf{r},t)}{\partial t}. \tag{2.15}$$

It is important to note that the source term is proportional to the time derivative of the Heating function H, and photoacoustic wave is produced by only time-variant heating.

Solutions of the photoacoustic wave equation have been presented for both point source described by the Dirac delta function [5,90,91] and a source which has Gaussian spatiotemporal profile [92]. In the following section, we discuss the former case which is mentioned in the rest of this thesis study.

2.3. Solution of the Photoacoustic Wave Equation for the Dirac Delta Pulse Excitation

The solution of the following wave equation can be obtained by utilizing the Green's function method

$$(\nabla^2 - \frac{1}{\upsilon_s^2}\frac{\partial^2}{\partial t^2})p(\mathbf{r},t) = S(\mathbf{r},t) \tag{2.16}$$

where $S(\mathbf{r},t) = -\frac{\beta}{C_P}\frac{\partial H(\mathbf{r},t)}{\partial t}$ is the source term. In photoacoustic effect, the laser pulse is very confined in both time and space so that the source term can be described by the Dirac delta function, $S(\mathbf{r},t,\mathbf{r}',t') = \delta(\mathbf{r}-\mathbf{r}')\delta(t-t')$. In this case, we obtain

$$(\nabla^2 - \frac{1}{\upsilon_s^2}\frac{\partial^2}{\partial t^2})G(\mathbf{r},t;\mathbf{r}',t') = \delta(\mathbf{r}-\mathbf{r}')\delta(t-t'). \tag{2.17}$$

Therefore, the solution becomes the Green's function and it is given by [5]

$$G(\mathbf{r},t;\mathbf{r}',t') = \frac{\delta(t-t'-\frac{|\mathbf{r}-\mathbf{r}'|}{\upsilon_s})}{4\pi\,|\mathbf{r}-\mathbf{r}'|} \tag{2.18}$$

for unbounded space. Here, $\mathbf{r}'$ and t' stand for the source location and time, respectively. Hence, the solution of Equation 2.13 can be found by evaluating the following integral expression

$$p(r,t) = \int_{-\infty}^{t^+} dt' \int dr' G(\mathbf{r},t;\mathbf{r}',t')\frac{\beta}{\kappa\upsilon_s^2}\frac{\partial^2}{\partial t^2}T(\mathbf{r}',t'). \tag{2.19}$$

Substituting Equation 2.18 into Equation 2.19 gives

$$p(r,t) = \frac{\beta}{4\pi\kappa\upsilon_s^2}\int dr' \frac{1}{|\mathbf{r}-\mathbf{r}'|}\frac{\partial^2}{\partial t^2}T(\mathbf{r}',t') \tag{2.20}$$

where $t' = t - \frac{|\mathbf{r}-\mathbf{r}'|}{\upsilon_s}$. Next, writing Equation 2.14 into Equation 2.20 yields

$$p(r,t) = \frac{\beta}{4\pi C_P}\int dr' \frac{1}{|\mathbf{r}-\mathbf{r}'|}\frac{\partial}{\partial t'}H(\mathbf{r}',t'). \tag{2.21}$$

Substituting $t' = t - \frac{|\mathbf{r}-\mathbf{r}'|}{\upsilon_s}$ into Equation 2.21 leads to

$$p(r,t) = \frac{\beta}{4\pi C_P}\frac{\partial}{\partial t}\int dr' \frac{1}{|\mathbf{r}-\mathbf{r}'|} H(\mathbf{r}', t - \frac{|\mathbf{r}-\mathbf{r}'|}{\upsilon_s}). \tag{2.22}$$

The heating function, $H(r,t)$, can be treated as a product of radial and temporal parts as follows

$$H(r',t') = A(r')H(t') \tag{2.23}$$

where $\int H'_t dt' = 1$. Now, Equation 2.22 becomes

$$p(r,t) = \frac{\beta}{4\pi C_P}\frac{\partial}{\partial t}\int dr' \frac{A(r')}{|\mathbf{r}-\mathbf{r}'|} H(t - \frac{|\mathbf{r}-\mathbf{r}'|}{\upsilon_s}). \tag{2.24}$$

Writing $H_t(t') = \delta(t')$ yields

$$p(r,t) = \frac{\partial}{\partial t}\frac{\beta}{4\pi C_P}\frac{1}{\upsilon_s t}\int dr' A(r')\delta(t - \frac{|\mathbf{r}-\mathbf{r}'|}{\upsilon_s})]. \tag{2.25}$$

By using the Gruneisen parameter given by Equation 2.7 and the initial pressure rise $p_0(\mathbf{r}) = \Gamma A(r')$ [93, 94], the photoacoustic pressure has its final form

$$p(r,t) = \frac{1}{4\pi\upsilon_s^2}\frac{\partial}{\partial t}[\frac{1}{\upsilon_s t}\int dr' p_0(r')\delta(t - \frac{|\mathbf{r}-\mathbf{r}'|}{\upsilon_s})]. \tag{2.26}$$

2.4. Generation of the Photoacoustic Wave From a Spherical Absorber

When a spherical object of radius R is illuminated with a laser pulse, the resultant initial pressure p_0 occurs inside the object. Next, the photoacoustic wave expression can be obtained from Equation 2.26. Here, three cases need to be considered based on the propagation time if the observation point is outside the object [5]. The first case is that the spherical object does not intersect with the spherical shell of radius $\upsilon_s t$ centered at the observation point so that the photoacoustic signal is zero if $r - R > \upsilon_s t$.

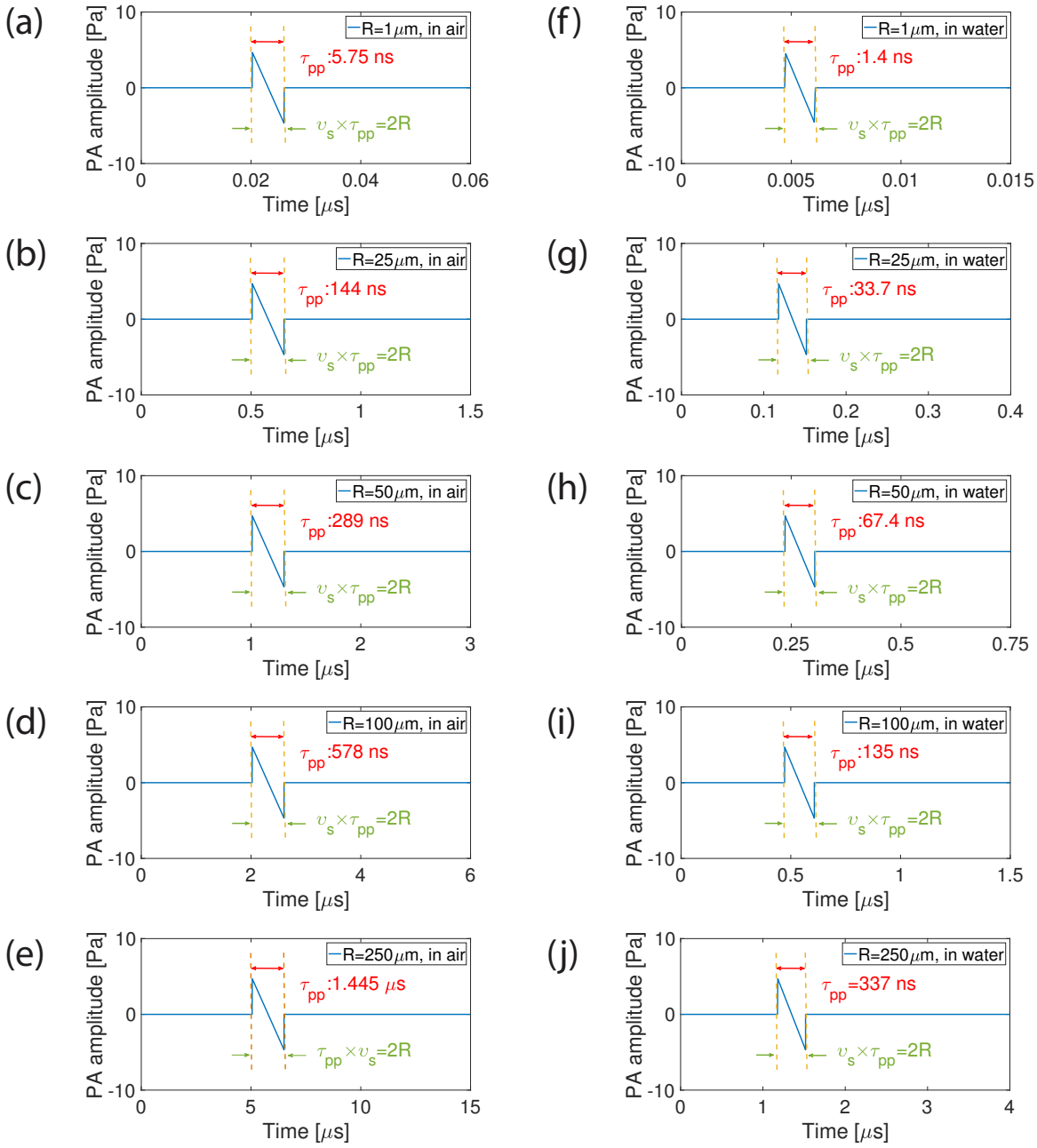


Figure 2.1. The characteristic N-shaped photoacoustic waves generated from spherical absorbers by delta heating for 1, 25, 50, 100, and 250 μm in radius for an initial pressure of $p_0 = 75$ Pa, and at distance of $r = 8R$, (a)-(e) in air and (f)-(j) in water, respectively. PA: Photoacoustic.

The second case is that upon the heating, the spherical object touches the spherical shell of radius $v_s t$ so that the pressure is $p(r,t) = \frac{p_0}{2r}(r - v_s t)$ if $v_s t$ is inside $[r - R, r + R]$. The third case is that the spherical object cannot intersect with the spherical shell and hence $p(r,t)$ is zero if $r + R < v_s t$. On the other hand, the other three cases need to be considered if the observation point is inside the spherical object ($r < R$). The first case is that when $v_s t < R - r$, the spherical shell is surrounded completely by the excited spherical object so that $p(r,t) = p_0$. The second case is that when $v_s t$ is inside $[R-r, R+r]$, the spherical shell comes out of the excited object and the pressure wave is $p(r,t) = \frac{p_0}{2r}(r - v_s t)$. The final case is that when $R + r < v_s t$, spherical shell surrounds the spherical object and $p(r,t)$ becomes zero [5].

By introducing the Heaviside step function, U, and taking into consideration the aforementioned cases, the photoacoustic signal is expressed by the following equation

$$p(r,t) = p_0[U(R - v_s t - r) + \frac{r - v_s t}{2r} U(r - |R - v_s t|)U(R + v_s t - r)]. \tag{2.27}$$

If the initial pressure distribution can be described by $p_0(r) = p_0 U(r)U(-r + R)$ for r is inside $[0, R]$, the following photoacoustic pressure wave expression is obtained

$$p(\mathbf{r},t) = \frac{r + v_s t}{2r} p_0(r + v_s t) + \frac{r - v_s t}{2r} p_0(-r + v_s t) + \frac{r - v_s t}{2r} p_0(r - v_s t). \tag{2.28}$$

In Equation 2.28, the first term on the right-hand side describes a converging spherical wave while the second term describes a diverging spherical wave, which is resulted from the initially converging wave propagating through the center. The last term on the right-hand side in Equation 2.28 also describes a diverging spherical wave. Upon the delta heating, a constant initial pressure wave through the entire sphere is created. This pressure wave consists of two spherical waves with the same magnitude. One of them moves inward (as a converging spherical wave, the first term in Equation 2.28 as the other one moves outward (as a diverging spherical wave the second term in Equation 2.28). The convergent spherical wave turns to a divergent spherical wave when it reaches the center of the object (the last term in Equation 2.28). Therefore,

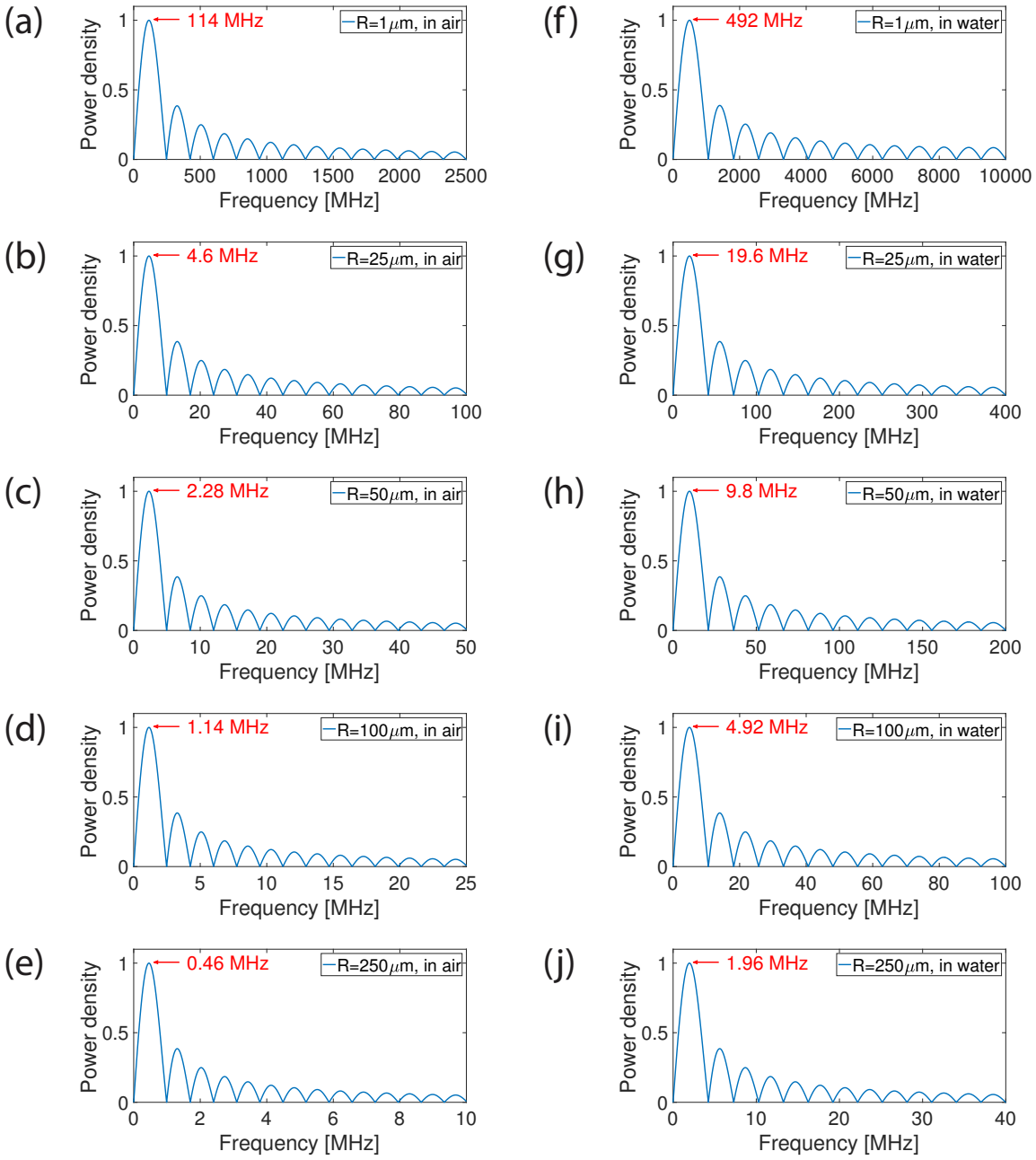


Figure 2.2. The FFTs of the N-shaped photoacoustic waves generated from spherical absorbers by delta heating for 1, 25, 50, 100, and 250 μm in radius for an initial pressure of $p_0 = 75$ Pa, and at distance of $r = 8R$, (a)-(e) in air and (f)-(j) in water, respectively, indicating the broadband frequency spectrum.

the photoacoustic pressure wave resulted from a delta heating has an N-shaped form.

In order to better understand the characteristic of the photoacoustic wave arising from spherical optical absorbers, we did some time domain and frequency domain

analyses using the solution of the photoacoustic wave equation. Figure 2.1 shows a set of photoacoustic waves generated from spherical absorbers by delta heating for 1, 25, 50, 100, and 250 μm in radius, as a function of time in the forward direction that is relative to the pulsed laser incident. The left column of Figure 2.1 belongs to photoacoustic waves generated in air while the right column in water. The results indicates that both the size of the absorber and the medium properties have dominant effects on the photoacoustic waveform. For example, while the peak-to-peak interval, τ_{pp} [95], for the N-shaped waveform (bipolar; positive followed by negative) of the photoacoustic wave from 1 μm size absorber is 5.75 ns in air, it is 1.4 ns in water. This is due to the effect of speed of sound on the propagation of the photoacoustic wave. The peak-to-peak interval is inversely proportional to speed of sound, which was taken as 346 and 1482 m/s for air and water, respectively, in this study (Figure 2.1a and Figure 2.1f). That is to say, the increase in the speed of sound leads to a decrease in the time duration of the photoacoustic wave, but still keeping the validity of the relation, $\upsilon_s \times \tau_{pp} = 2R$, regardless of what the medium is. Furthermore, when the size of the absorber increases the peak-to-peak duration also increases that can be seen from the left column and the right column of Figure 2.1. The value of 5.75 ns for an absorber of 1 μm becomes 1.445 ns for an absorber of 250 μm, again keeping the validity of the relation, $\upsilon_s \times \tau_{pp} = 2R$. Thus, the larger the radius of the absorber, the longer the peak-to-peak interval τ_{pp} of the photoacoustic wave. In addition, the increase in the speed of sound leads to a decrease in the value of τ_{pp}, but still keeping the validity of the relation, $\upsilon_s \times \tau_{pp} = 2R$, regardless of what the medium is. It should be noted here that the speed of sound in the absorber and the surrounding medium was considered the same. Thus, purely N-shaped photoacoustic waves can be generated only when the optical absorber has the same acoustic impedance with the surrounding medium.

On the other hand, analyses in frequency domain of the N-shaped photoacoustic wave (induced by especially short pulses) indicate the fact that the photoacoustic wave has a broadband frequency spectrum, shown in Figure 2.2. In other words, the wave packet contains relatively low frequency components with dominant amplitudes together with the high frequency components with decreasing amplitudes. For example, the absorber of 1 μm size generates photoacoustic waves having a maximum power

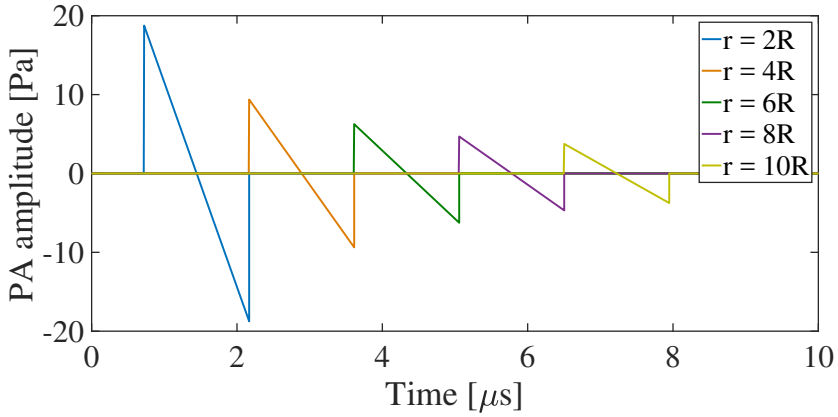


Figure 2.3. (a) The characteristic N-shaped photoacoustic waves generated from a spherical light absorber of $R = 250$ μm for $p_0 = 75$ Pa. The amplitude of the photoacoustic wave decays with distance with respect to inverse distance law (see Equation 2.28), (b) Normalized power spectral density of this photoacoustic wave.

density at 114 MHz together with higher components up to GHz order in air which is shown in Figure 2.2a. Besides, the maximum frequency value becomes 492 MHz in water (Figure 2.2f). Thus, the increase in the speed of sound leads to an increase in the frequency values in accordance with the increase in speed of sound In addition, the larger the radius of the absorber, the lower the frequency of the generated photoacoustic wave as can be seen on the left column and the right column of Figure 2.2.

Moreover, we also observe that the amplitude of generated photoacoustic wave decreases with the distance from the absorber. Figure 2.3 shows the photoacoustic waves as a function of time at certain distances of $r = 2R$, $4R$, $6R$, $8R$, and $10R$ in air, in accordance with the inverse distance law seen in Equation 2.28. The decrease behavior of the photoacoustic wave with respect to distance is same in water, as well.

3. DEVELOPMENT OF A NOVEL FIBER LASER WITH INDEPENDENTLY ADJUSTABLE PROPERTIES FOR OPTICAL RESOLUTION PHOTOACOUSTIC MICROSCOPY

In this chapter, we present a novel fiber based MOPA laser system which produces nanosecond pulses, covering spectrum from 450 nm to 1100 nm, specifically for PAM [6]. The supercontinuum part is all fiber-integrated; guided-beam-propagation renders its misalignment free and largely immune to mechanical perturbations. Free space harmonic generation creates higher pulse energy for a specific band, i.e. 532 nm, and also generates ultra violet (UV) light with wavelengths of 355 and 266 nm. Total supercontinuum output power is over 1 W and visible output power is around 270 mW at 65 kHz repetition rate corresponding to 4 μJ pulse energy. One of the novelties here is the improvement of wavelength tunability, output power and pulse energy when fiber-based lasers are benchmarked. This is the first demonstration of spectroscopic PAM by developing a supercontinuum all-fiber based MOPA source. The tunability of the laser parameters allows using only one laser for many different PAM applications, and also high repetition rate enables fast scanning. The coverage of near-UV spectrum gives an opportunity to image cell nuclei. Certain morphological changes such as size and shapes irregularities in the nuclei are known indicators of various cancers [56,96,97], and we believe our laser may also be useful for cell nuclei studies as well.

3.1. Methods

A widely tunable fiber laser system was designed in MOPA configuration. The output of the MOPA configuration seeds two arms; the first one is used for supercontinuum generation via spectrum broadening and the second is for harmonic generation through nonlinear crystals. It should be noted that pulses with sufficiently narrow bandwidths are required for harmonic generation (second, third, and fourth) [98] through nonlinear crystals. The increase in the length of the crystal results in more ef-

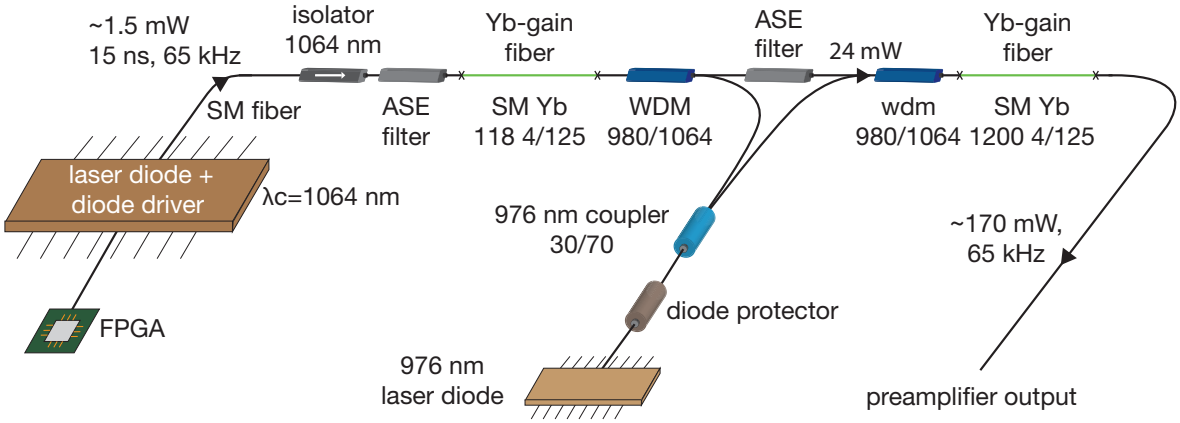


Figure 3.1. The schematic of the oscillator and preamplifier parts of the laser. SM: Single mode (fiber), FPGA: Field-programmable gate array, WDM: Wavelength division multiplexer, and ASE: Amplified spontaneous emission.

ficient wavelength conversion; yet, longer crystals bring along phase shifts proportional to the bandwidth of the laser, and decrease the efficiency [99]. For this reason, a 1064 nm fiber-coupled diode laser (I-IV Laser Enterprise) with a very narrow bandwidth (0.3 nm) is used and driven by a nanosecond diode driver (PicoLas, LDP-V 03-100 UF V3). Pulse width of the laser diode was adjusted through a field programmable gate array (FPGA) card (BASYS2, Xilinx). 15 ns long pulses at 65 kHz repetition rate were generated and sent to Yb-doped gain fiber after passing through an isolator and an amplified spontaneous emission (ASE) filter. As a pump source, a 976 nm laser diode (II-VI Laser Enterprise) delivering a maximum power of 540 mW was used. The pump is first passed through a pump protection filter with a maximum power handling of 300 mW, followed by a 30:70 coupler allotting two stages of preamplifier.

3.1.1. Oscillator and Preamplifier

In the first stage, Yb-doped fiber is backward-pumped by 30% of the output of the laser diode, then combined with the signal through a wavelength division multiplexer (WDM). Backward pumping is crucial for decreasing ASE generation rate, and hence it prevents possible damage to the pump diodes and other fiber components. Another ASE filter is used between preamplifier stages to prevent the first from ASE that may be produced in the second. A WDM is used to combine 70% of the output of the laser

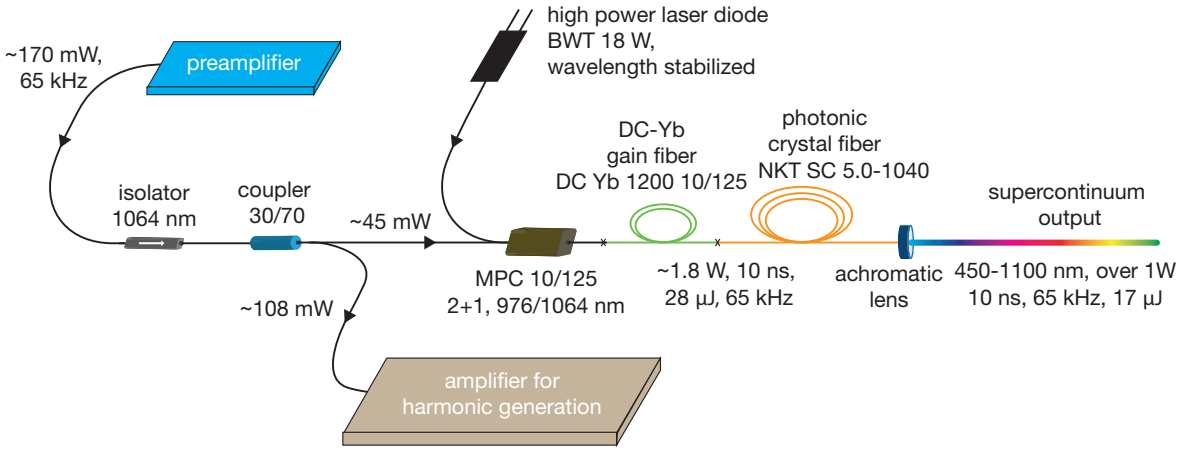


Figure 3.2. The schematic of the supercontinuum generation part of the fiber laser.

diode pump and the first stage of the preamplifier. For amplification, an Yb-doped fiber is used and the output power is measured as 170 mW at 65 kHz repetition rate. The last component of the second preamplifier is an isolator with a maximum power handling of 2 W in order to protect it from back reflections. The schematics of the oscillator and preamplifier parts are shown in Figure 3.1. At the end of the preamplifier, a 30:70 coupler separates the signal, 30% is utilized for supercontinuum and 70% is for harmonic generation.

3.1.2. Supercontinuum Generation

Following the amplifier output, 30% of the signal having an average power of 45 mW was firstly amplified for supercontinuum generation using a high power laser diode having a maximum power of 18 W and a double clad (DC) Yb-doped fiber (Yb-1200 20/125 PM, nLight Liekki). Here, the signal and the pump were combined by a multi-mode pump combiner (MPC) (10-125, 2+1, 976/1064 nm) before the gain fiber. The schematic of the supercontinuum generation part is shown in Figure 3.2. A 15 m long PCF (SC 5.0–1040, NKT) with 5 μm core size is spliced to the end of Yb-doped fiber (Yb-1200 20/125 PM, nLight Liekki). It should be noticed here that the core size of the Yb-doped fiber is 20 μm which is larger than the core size of the PCF. For this reason, a special splice was used in between the Yb-doped fiber and PCF by a suitable splicer (FSM-100M, Fujikura). Optical spectrum of the supercontinuum was measured by two optical spectrum analyzers (OSA) with different wavelength ranges;

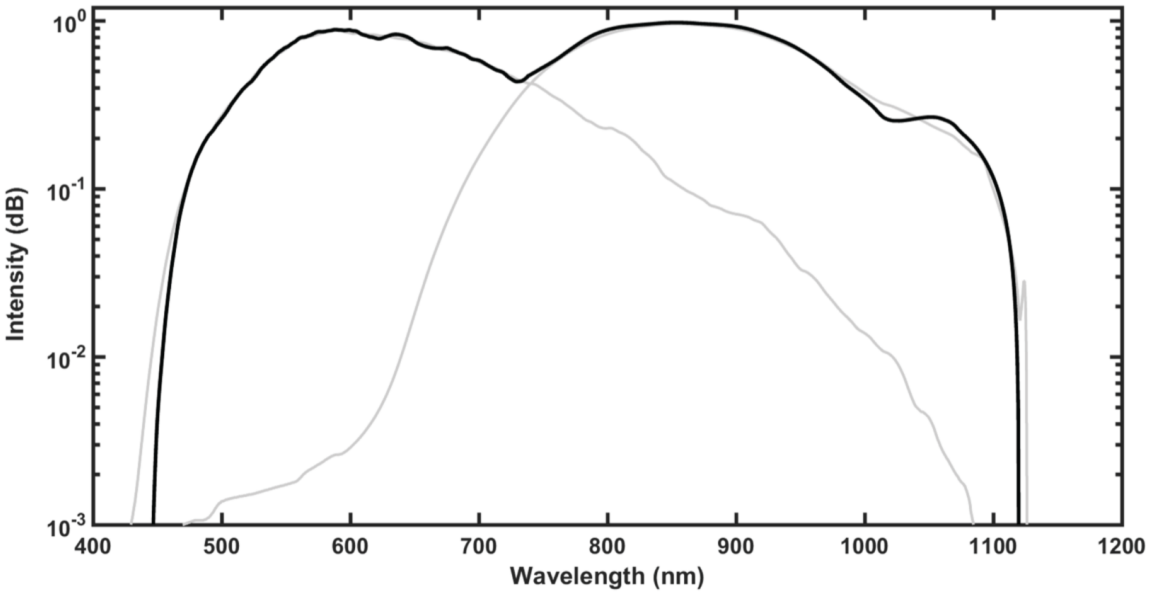


Figure 3.3. Optical spectrum of the supercontinuum output of the fiber laser measured by two optical spectrum analyzers (OSA) with different wavelength ranges; OSA 1 (Avaspec-3648-VIS, Avantes) and OSA 2 (QE65 Pro, Ocean Optics). The acquired spectra were digitally combined in a single figure.

OSA 1 (Avaspec-3648-VIS, Avantes) and OSA 2 (QE65 Pro, Ocean Optics). The acquired spectra were digitally combined in a single figure shown in Figure 3.3. In the first spectrum, the intensity of near infrared region appears lower than its actual level due to the decrease in the response of the analyzer while approaching to the edges of the measurable spectra region. It may also be caused by the difficulty of collecting all the beam with broad spectrum which is collimated by a single lens. Although the lens is an achromatic lens, it may still not be enough to eliminate slight divergence for different wavelengths and thus amplitude measurement variation throughout this broad spectrum range. In the second one, the intensity of the region between 450 to 650 nm lowered to noise level as a result of using neutral density filters in order to prevent saturation of the detector for the remaining spectrum. Pulse duration of the laser is 10 ns for supercontinuum output.

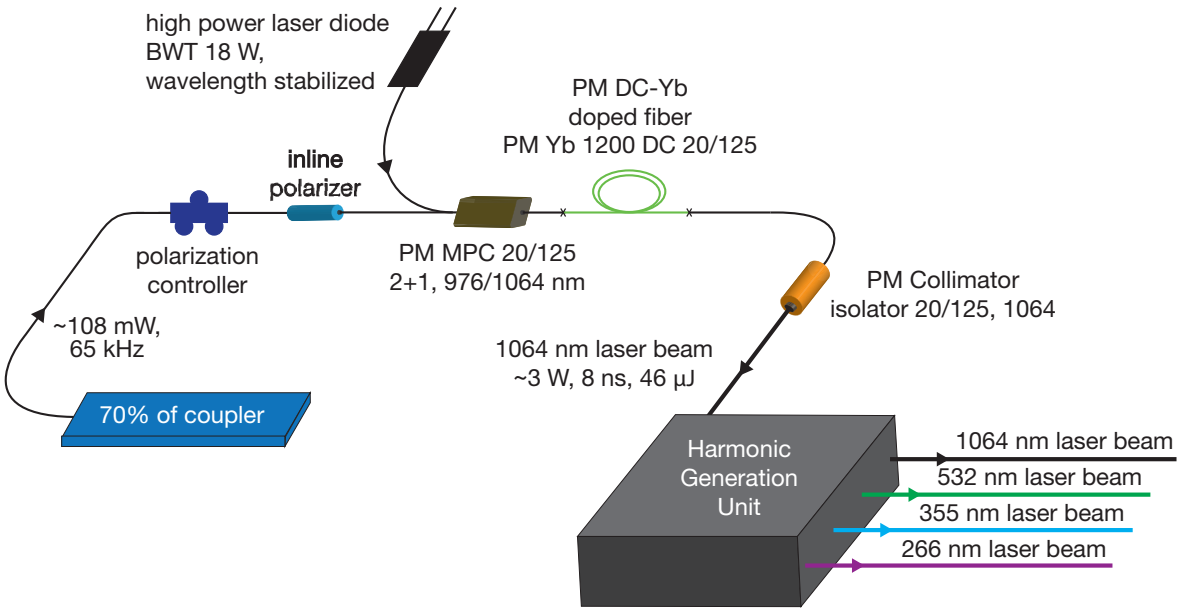


Figure 3.4. The schematic of the amplifier just before the harmonic generation unit. MPC: Multi-mode pump combiner.

3.1.3. Harmonic Generation

Polarization of light is crucial for frequency multiplication; thus, 70% of the allocated signal is passed through a polarizer and all fiber components beyond this point are polarization maintaining. The schematics of the oscillator and preamplifier parts are shown in Figure 3.4. A 976 nm diode laser is used and a multi-mode pump combiner (MPC) combines the pump and signal. A polarization maintaining double cladding Yb-doped (PM-DC-Yb) fiber is spliced to the end of the MPC for amplification of the signal and pulses with 8 ns duration with an average power of 3 W at 65 kHz repetition rate are acquired. Figure 3.5a shows the optical spectrum and Figure 3.5b shows the temporal profile of a pulse at the end of the amplification. In the temporal profile, the leading edge of the pulse is sharpened, or self-steepened, as the gain is partially saturated by each individual pulse and consequently less gain is available for the trailing edge. The temporal structure in the trailing edge is a static structure, which does not vary from pulse to pulse, originating primarily from the dynamically varying impedance of the semiconductor diode that seeds the system.

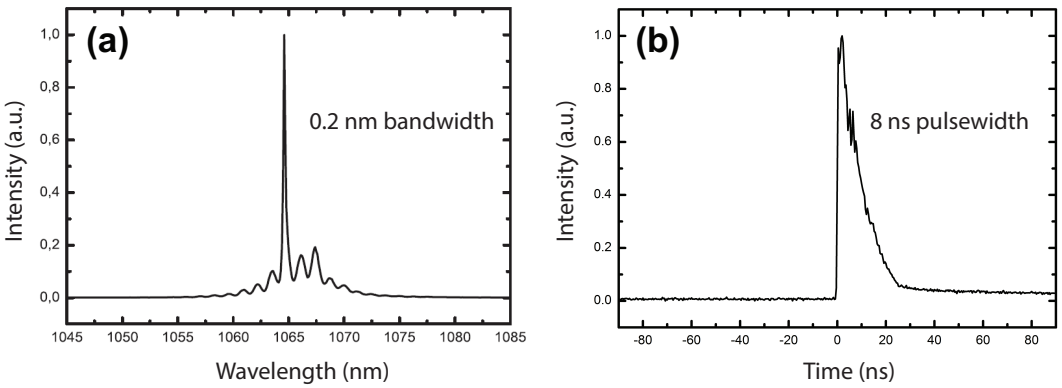


Figure 3.5. (a) Optical spectrum, (b) Temporal profile of a typical pulse at the end of PM-DC-Yb fiber.

For frequency multiplication process, a half wave plate is employed to match the polarization between the isolator and crystals. An anti-reflection coated (for 1064 nm wavelength) lens with a focal length of 30 mm is used to focus light into crystal. For SHG, a 20 mm long Lithium Triborate (LBO) crystal (Eksma, LBO-405) is used. For non-critical phase matching (NCPM), a crystal oven and a proportional-integral controller is added to maintain the temperature at 150.8 °C that results in maximum power. The light is passed through an anti-reflection coated (for 532/1064 nm) lens for collimation. Two dichroic mirrors separate the generated SHG beam (532 nm light) from the 1064 nm beam. Here, the output power is measured as 500 mW for 532 nm light. A mirror hold including a dichroic mirror reflecting 532 nm wavelength is added to the system. When the mirror is flopped, beam including 532 and 1064 nm wavelengths pass through a lens to enter a crystal (Eksma LBO- 407) for THG. The crystal is maintained at 40 °C for NCPM. The output power is around 3 mW for 355 nm light. Another flip mirror mount with a dichroic mirror that is transmitting 1064 nm and reflecting 532 nm beam is added to direct the beam toward a lens with a focal distance of 30 mm. This lens focuses the beam into a Barium Borate (BBO) crystal (Eksma BBO-700, thickness = 6 mm) that generates the second harmonic of the 532 nm beam (fourth harmonic generation), which results in around 10 mW of 266 nm light. The output of the crystal is filtered via a dichroic mirror reflecting 266 nm light and collimated by using a UV-coated lens with a focal distance of 50 mm. Pulse duration of the laser is 8 ns for harmonic generation output. Figure 3.6 shows the schematic of the harmonic generation module.

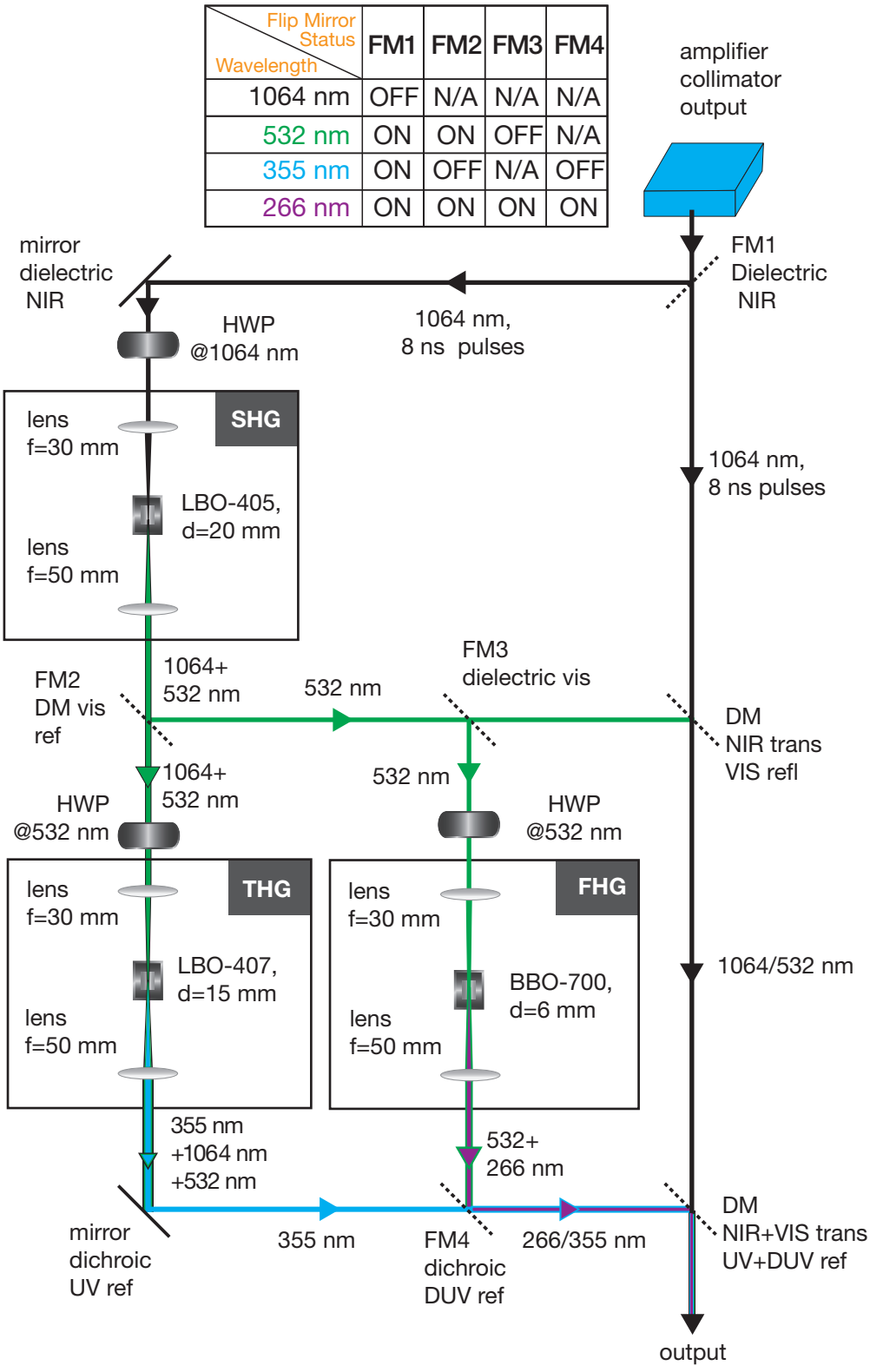


Figure 3.6. The schematic of the harmonic generation unit. FM: Filiping mirror, DM: Dichroic mirror.

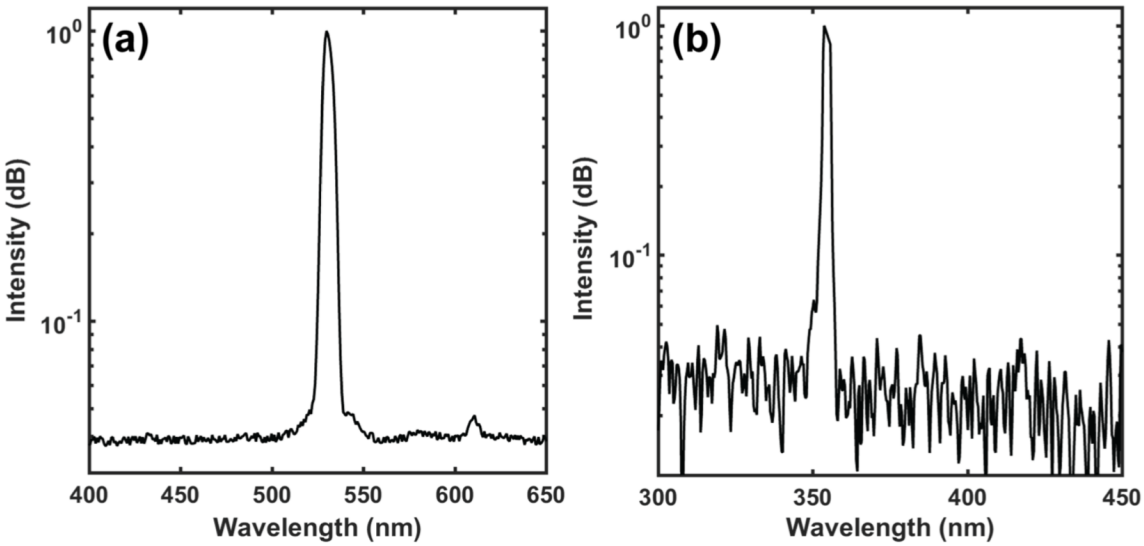


Figure 3.7. (a) Optical spectrum of the SHG output acquired by OSA 2, (b) The THG output acquired by OSA 1.

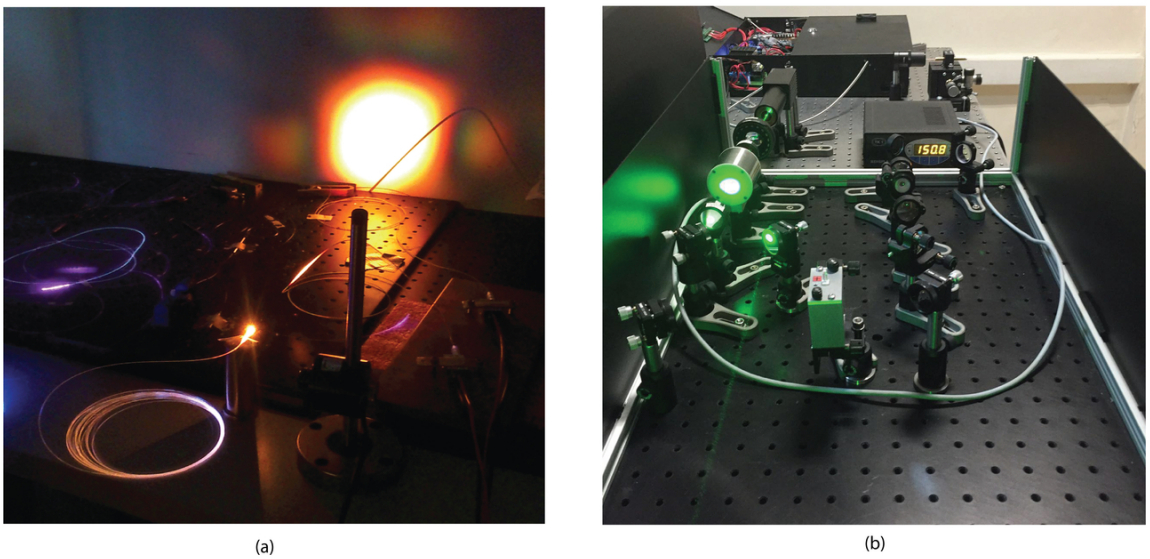


Figure 3.8. The photographies of the outputs of (a) the supercontinuum, and (b) the harmonic generation unit of the laser.

Table 3.1. The output specifications of the laser.

Output	**Average Power**	**Pulse Energy (at 65 kHz)**
Supercontinuum	Total: 1 W	17 μJ
	Visible: 270 mW	4 μJ
Harmonic Generation	1064 nm: 5 W	66 muJ
	532 nm: 500 mW	8.5 muJ
	266 nm: 10 mW	170 nJ
	355 nm: 3 mW	56 nJ

The optical spectrum of the SHG is shown in Figure 3.6a and of THG in Figure 3.6b. The spectra are acquired with OSA 2 and OSA 1, respectively. Figure 3.8a and Figure3.8b show the photograph of the outputs of the supercontinuum and the harmonic generation units, respectively.

Our tunable fiber-based laser system has three outputs; supercontinuum (from 450 to 1100 nm), 1064 nm from single-wavelength emitting port, and harmonic generation (532, 355, and 266 nm). The average power of 1064 nm output is around 3 W which seeds harmonic generation unit but also can be used for its own applications. The maximum average power values of SHG (532 nm), third harmonic generation (THG, 355 nm), and fourth harmonic generation (FHG, 266 nm) are 500, 3, 10 mW, respectively. Total output power of supercontinuum was measured over 1 W with visible output power around 270 mW with a powermeter (S314C, Thorlabs) at 65 kHz repetition rate that corresponds to 15 μJ total and 4 μJ visible energy. Table 3.1 shows all these specifications with the corresponding pulse energy values. Furthermore, various bandpass filters were used to obtain wavelength of interest from supercontinuum output and power measurements were performed to compare with the values in the literature given in Discussion section of this chapter. In order not to damage bandpass filters, a 1000 nm shortpass filter was firstly employed. Average power values at wavelengths of 680 and 830 nm with 10 nm bandwidths were measured as 5 and 11 mW by a powermeter (S142C, Thorlabs) after a achromatic lens that corresponds to 76 and 169 nJ pulse energy. For wider bandwidths, average power values for wavelengths of 650, 697, 732, 785, and 880 nm with 80, 75, 68, 62, and 70 nm bandwidths were measured

Table 3.2. The average power and pulse energy values for several wavelengths filtered from the supercontinuum output of the fiber laser.

Wavelength (nm)	**Bandwidth (nm)**	**Average Power mW**	**Pulse Energy at 65 kHz**
650	80	92	1.4 μJ
680	10	5	76 μJ
697	75	93	1.4 μJ
732	68	82	1.3 μJ
785	62	84	1.3 μJ
830	10	11	169 μJ
880	70	142	22 μJ

as 92, 93, 82, 84, 142 mW, that corresponds pulse energies 1.4, 1.4, 1.3, 1.3, 2.2 μJ, respectively. Table 3.2 summarizes all these power values with the corresponding pulse energy values.

3.2. Discussion

In order to evaluate the performance of our laser system, pulse energy, average power and repetition rate values were compared with the ones in existing systems within the literature including fiber components and independent of seeding laser type, mentioned in Section 1.1. Billeh *et al.* [61] sent the output of a Q-switched Nd:YAG microchip laser with a repetition frequency of 6.6 kHz to a 7 m-long PCF and reported seven wavelengths of 575, 625, 675, 725, 775, 825, and 875 nm with a bandwidth of 40 nm for each wavelength and pulse energies were measured as 7, 15, 24, 31, 31, 31, and 33 nJ, respectively. Lee *et al.* [63] also sent the output of the same type of laser to a 10 m-long PCF and stated pulse energy of the generated supercontinuum light as 500 nJ. The pulse energies of two bands, 500 to 560 and 560 to 660 nm were measured as 0.6 and 1.8 nJ, respectively. As can be seen, these pulse energies are quite low despite the wide bandwidths. There are many attempts to develop multiwavelength laser systems generating higher pulse energies from the output of an integrated fiber for various photoacoustic imaging applications [61, 64–66, 70]. However, this condition

Table 3.3. Comparison of the output specifications of the lasers reported in the literature utilizing PCF to broaden the spectrum.

	Pump Laser	**Pulse Duration (ns)**	**Output Wavelength (nm)**	**Measured Wavelength (nm)**	**Bandwidth (nm)**	**Energy (nJ)**	**PRF (kHz)**	**Fiber Type**
Billeh *et al.* 2010 [61]	Q-switched Nd:YAG Microchip Laser	0.6	500-1300	575, 625, 675, 725, 775, 825, 875	40	7, 15, 24, 31, 31, 31, 33	6.6	7 m PCF
Lee *et al.* 2014 [63]	Q-switched Nd:YAG Microchip Laser	0.7	500-1700	530, 610	60-100	0.6, 1.8	21	10 m PCF
Shu *et al.* 2016 [64]	Q-switched Nd:YAG Microchip Laser	2	500-2300	NA	NA	NA	25	PCF tapper
Bondu *et al.* 2016 [70]	Q-switched Nd:YAG Microchip Laser	4	500-1600	Total ——— Visible	NA ——— <850nm	22000 ——— 6000	1	15 m PCF tapper

requires PCFs to withstand such high energies. Since nonlinearity increases as the effective mode area of fiber gets smaller; thus, it is advantageous to decrease core diameter for generation of more efficient supercontinuum. Yet, energy per surface area of the fiber has a major effect on the maximum optical pulse peak power which a fiber can withstand [100–102]. Therefore, there is a trade-off between supercontinuum efficiency and energy to be coupled into the fiber. In order to overcome this limitation, tapered fibers are designed. Bondu *et al.* [70] used a nonlinear fiber that combines a large-core fiber for high-pulse energy handling with a small-core fiber for efficient spectral broadening. They used five different PCFs with varying core diameters, two of them were tapered for supercontinuum generation. They also demonstrated that total energy at the output of the straight PCF with core diameters of 5, 9, and 10 μm as 10, 29.5, and 30 μJ, respectively with visible output energies of 1.7, 5.4, and 4.6 μJ. Total output energy of tapered PCF of length of 1 m with an input core diameter of 10 μm tapered down to 5 μm was stated as 22 μJ with visible output energy of 6 μJ [64, 70]. Table 3.3 summarizes the specifications of the aforementioned lasers including the pump laser source, pulse duration, output range, measured wavelengths, bandwidths, PRF, and fiber types.

As we discussed in Section 1.1, taking advantage of SRS inside a fiber is another method to increase the number of wavelengths from a fixed wavelength output. Polarization-maintaining single-mode fiber (PM-SMF) as well as PCF has been used for generation of SRS peaks [65, 66, 71, 84, 85]. Koeplinger *et al.* [65] sent the output of a Q-switched Nd:YAG microchip laser with a repetition frequency of 7.5 kHz to a frequency-doubling KTP crystal. Then, this output was sent to a 6 m-long PM-SMF and acquired four distinct bands 546, 560, 574, and 600 nm with a pulse energy of 80 nJ for the each wavelength. Loya *et al.* [66] coupled the output of a Q-switched Nd:YAG laser operating at 30 kHz repetition rate to a 30 m-long large mode area photonic crystal fiber (LMA-PCF) and individual pulse energies were reported as 270, 360, 520, 530, and 400 nJ at wavelengths of 532, 546, 568, 589, and 600 nm, respectively. Buma *et al.* [68] also used PM-SMF of 20 m-long to generate SRS peaks and reported pulse energies of 1170, 250, 390, 480, 430, and 200 nJ for optical wavelengths of 1064, 1097, 1150, 1215, 1275, and 1325 nm, respectively. In addition, Ferrari *et al.* [67] utilized the

Table 3.4. Comparison of the output specifications of the lasers reported in the literature utilizing SRS or four-wave mixing techniques to obtain multiwavelength spectrum.

	Pump Laser	**Pulse Duration (ns)**	**Output Wavelength (nm)**	**Measured Wavelength (nm)**	**Bandwidth (nm)**	**Energy (nJ)**	**PRF (kHz)**	**Fiber Type**
Koeplinger *et al.* 2011 [65]	Q-switched Nd:YAG Microchip Laser	0.6	532, 546, 560, 574, 600		NA	80	7.5	6 m PM-SMF
Loya *et al.* 2012 [66]	Q-switched Nd:YAG	1.8	532 610	532, 546, 568, 589, 600	NA	NA	30	30 m LMA-PCF
Buma *et al.* 2015 [68]	Q-switched Nd:YAG Microchip Laser	0.6	1064 110 1175 1225 1275 1375	1064 1097 1150 1215 1275 1325	NA 4 4.5 10 20 55	1170 250 390 480 430 200	7.4	20 m PM-SMF
Ferrari *et al.* 2015 [67]	Q-switched Nd:YAG	2	532 900	532, 546, 590, 600, 650, 700, 750, 800, 850	NA	up to 100	20	100 m SMF-28e

four-wave mixing technique to generate multiwavelength and reported pulse energy up to 100 nJ for several wavelengths. Table 3.4 summarizes the output specifications of the above mentioned lasers, as well. Hajireza *et al.* [71, 84, 85] coupled an Yb-doped fiber laser into a PM-SMF in varying lengths at different PRFs and extended the number of wavelengths at SRS peaks. The acquired pulse energies were in between 100 to 500 nJ. Allen *et al.* [86] produced an all-fiber laser source with a PRF up to 2 MHz but the output wavelength was fixed. Mahmud *et al.* [87] also reported a fiber based laser source. By means of electronic modulations in the oscillator, tuning the repetition rate (0.1–120 MHz), the pulse-width (0.1–5 ns) and the wavelength (1030–1080 nm) were carried out. Green light was also generated through frequency doubling. The output power was reported up to 1.1 W and pulse energy up to 500 nJ. However, wavelength cannot be tuned in a broad range which does not allow for various spectroscopic photoacoustic applications. Table 3.5 summarizes the output specifications of the above mentioned lasers with high repetition frequencies.

On the other hand, the energy values of our fiber laser are higher than the ones produced through coupling the output of Q-switched Nd:YAG microchip laser to PCF which is at most 33 nJ (see Table 3.3). As mentioned above, for the special case of tapered PCFs, visible output energy (<850 nm) was reported as 6 μJ at 1 kHz, for our system that is 4 μJ at 65 kHz and comparable to that output [64, 70]. In addition to that, our laser source can provide higher pulse repetition rate, up to 1 MHz, at the expense of lower pulse energies. For the systems utilizing SRS, the energies per band were reported as several hundreds of nJ with an utmost energy of 500 nJ [71, 85]. Here, SRS peaks are produced with a bandwidth around 10 nm, pulse energies are higher than our system for such narrow bandwidths for visible region. However, when filters with wider bandwidths are selected, pulse energies become higher than ones that SRS peaks possess. To be also noted, pulse energies of SRS peaks decreases (estimated around 100 nJ) elongating near-infrared spectral region. The edge of peaks was noted as 788 nm [71], our spectrum covers up to 1100 nm. There are many other advantages of our system. All the laser parameters, which are reported as independently adjustable, could be achieved by changing FPGA configuration and currents to the pump diodes electronically without any mechanical intervention. The only exception to this is the

]

Table 3.5. Comparison of the output specifications of the fiber-based pump lasers reported in the literature in which SRS is used to obtain multiwavelength. PM-SMF: Polarization Maintaining Single Mode Fiber, PRF: Pulse repetition frequency.

	Pump Laser	**Pulse Duration (ns)**	**Output Range (nm)**	**Measured Wavelengths (nm)**	**Bandwidth (nm)**	**Energy (nJ)**	**PRF (kHz)**	**Fiber Type**
Hajireza *et al.* 2013 [84]	Yb-doped fiber laser	1	532, 543, 560, 590,600		10	300-500	40	3 m PM-SMF
Hajireza *et al.* 2014 [71]	Yb-doped fiber laser	1	545, 550, 558, 570, 580, 590, 600		NA	136, 76, 151, 21, 105, 213, 116	160	6 m PM-SMF
Mahmud *et al.* 2015 [87]	Fiber-based laser (MOPA	0.1-5	1030-1080, 515-540	1064	NA	500	100-120000	NA

switching among the supercontinuum and harmonic generation ports, which is achieved by a mechanically switchable mirror, that can also readily be motorized, if desired. In addition to this, it is very compact with dimensions of 40x40x9 cm3 except from free-space harmonic generation unit and does not require any big cooling unit. Thanks to its high PRF, it may be a promising source for cytometry as well [82].

In our system, the light is transmitted through the splice between Yb-doped fiber and PCF for rendering all-fiber integrity with an efficiency of 40%. One of the disadvantages of current configuration is the heating at the splice point. Despite the cooling fan, the splice should be renewed once in a while in order to compensate for decreasing power in time. In order to handle the issue for robust and long-term operation, the splicing between the gain fiber and the PCF is optimized for low-loss and high tensile strength (using GPX-3000 series splicer, Vytran, Inc.), as demonstrated in the context of in-situ absorption spectroscopy of plasmas using a similar supercontinuum source and the same type of fibre [103]. Free space coupling is also possible between Yb-doped fiber and PCF; in that case transmission can be performed with higher efficiency and higher pulse energies can be produced if all-fiber integrity is disregarded. The present limitations to the continuously and independently adjustable laser parameters arise from the requirement of simultaneous satisfaction of the following conditions during laser design: ensuring that each amplification stage is seeded with sufficient power to prevent generation of laser noise in the form of amplified spontaneous emission (ASE), ensuring that the targeted, final pulse duration will depend on the seed pulse duration in a complex manner due to gain saturation and that there is sufficient peak power to accomplish the supercontinuum generation in the PCF. We believe that even a large range of parameters are possible, albeit at the cost of increased system complexity (by adding a second acousto-optic modulator and additional amplifier stages). The present parameter range was decided based on the balance between system complexity and sufficiency for most typical OR-PAM applications.

To sum up, when all-fiber based laser systems are taken into consideration, the developed system improves the wavelength tunability with a repetition rate up to 1 MHz. For laser systems having fiber components, pulse energies of this system are

higher from PCF coupled supercontinuum cases and comparable to the outputs of special tapered PCF designs. The system also offers all-fiber integrity and higher PRF by means of custom developed FPGA electronics that controls laser diode. Pulse energies of SRS peaks can be surpassed at near-infrared region with same bandwidth, at visible region only by using filters with wider bandwidths. This paper presents the potential of a tunable fiber laser system in MOPA configuration for multiwavelength OR-PAM. We believe that the system may provide the means of spectroscopic photoacoustic microscopy applications via widely tunable fiber laser technologies.

4. BUILDING A CUSTOM-DESIGNED PHOTOACOUSTIC MICROSCOPY SYSTEM

One of the objectives of this dissertation was to build a custom designed photoacoustic microscopy (PAM) system in which ultrasonic piezoelectric transducers are used as pressure sensors. In this microscopy system, we used both the OPO laser mentioned in Section 1.2 and the custom-developed fiber laser mentioned in Chapter 3 as the photoacoustic excitation source. We first co-aligned the outputs of these two lasers in a same optical path through sample in which any of them could be made passive with the help of a flipping mirror when requested. Thus, we were able to generate photoacoustic signals by using these two lasers without sacrificing the alignment of anyone. Besides, this provided us quick laser selection and also equivalent measurement conditions. The sample holder was fixed on a 3D motorized translational stage (LNR50SEK1, Thorlabs) which could be controlled by a computer. The transducer was fixed above the sample location through optomechanical components connected to a 3D manual translational stage to adjust the source/detector distance. Thus, we have built the system called transmission mode PAM system by utilizing a transducer angle of 45 degree to the laser path. Photoacoustic detection was performed by various transducers at different frequencies. The signals were initially amplified by 40 dB using a preamplifier (5678, 40 MHz bandwidth, Olympus) and then 39 dB via a pulser/receiver (5073PR, Olympus). The collected signals were digitized through a data acquisition card (DAQ) (Razor Express CompuScope 1422, Gage Applied Technologies, Inc.) then data processing and reconstruction were performed in MATLAB. The schematic of the PAM system is shown in Figure 4.1.

4.1. Photoacoustic Signal Generation: Preliminary Studies

To test the performance of our PAM system, we first concentrated on the detection of photoacoustic signals arising from the black India ink (Dr. Ph. Martin's Bombay Black, Salis International Inc., Golden, CO). This sample was particularly

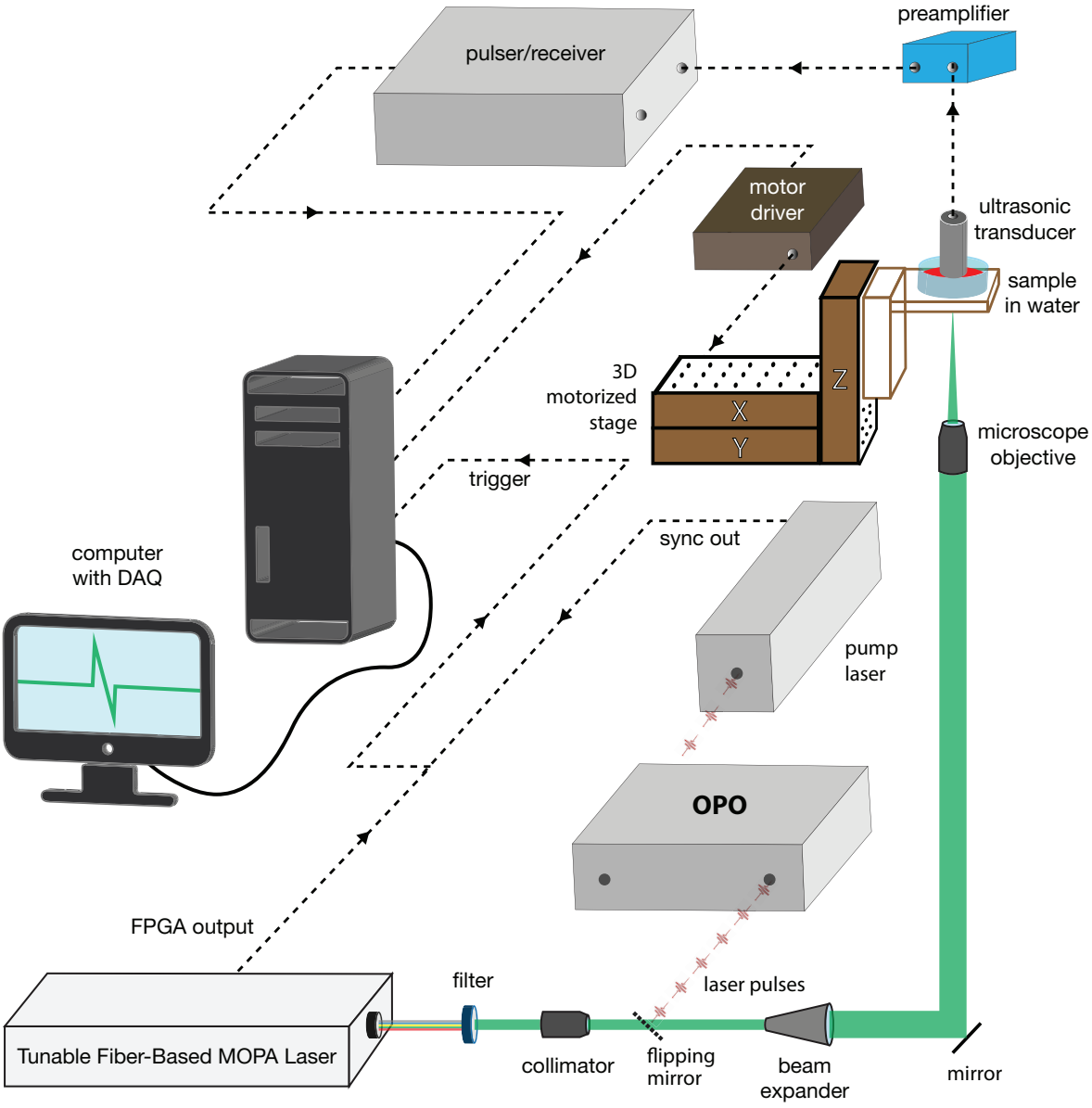


Figure 4.1. The schematic of the experimental setup of the PAM system. The tunable fiber-based laser and OPO laser are co-aligned in a same optical path through sample in which any of them could be made passive with the help of a flipping mirror when requested.

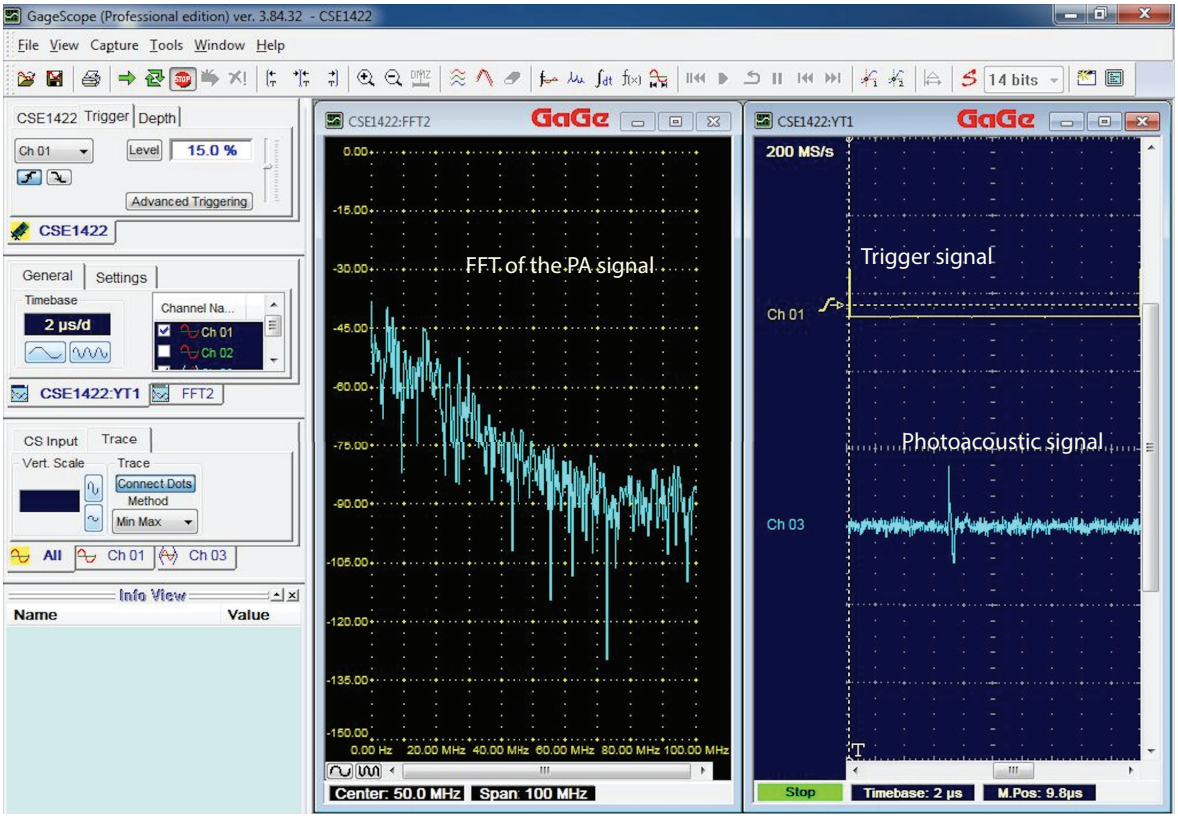


Figure 4.2. The screenshot of the DAQ indicating the photoacoustic signal generated from an ink-loaded fiber tube phantom.

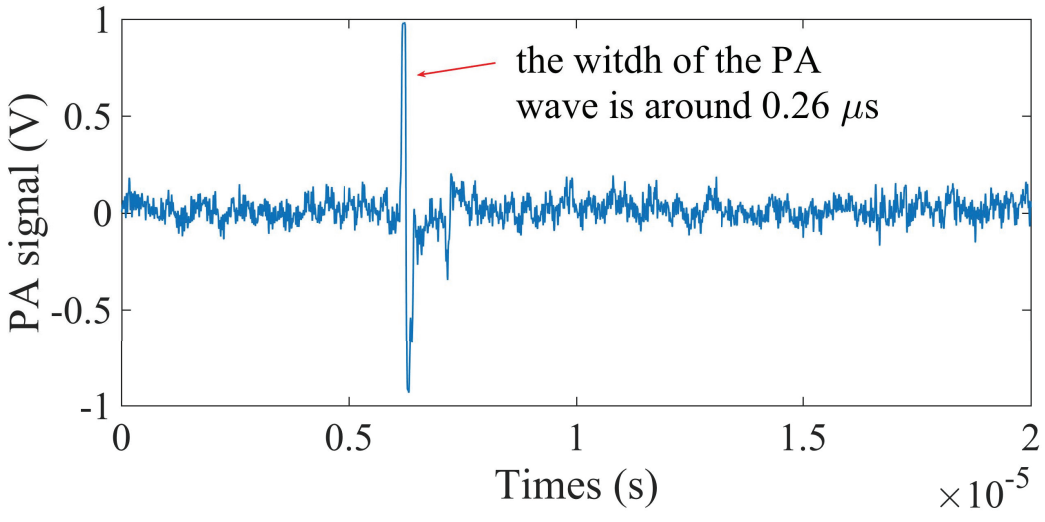


Figure 4.3. A photoacoustic signal generated from a horse tail-hair with a diameter of 350 μm illuminated by a laser pulse.

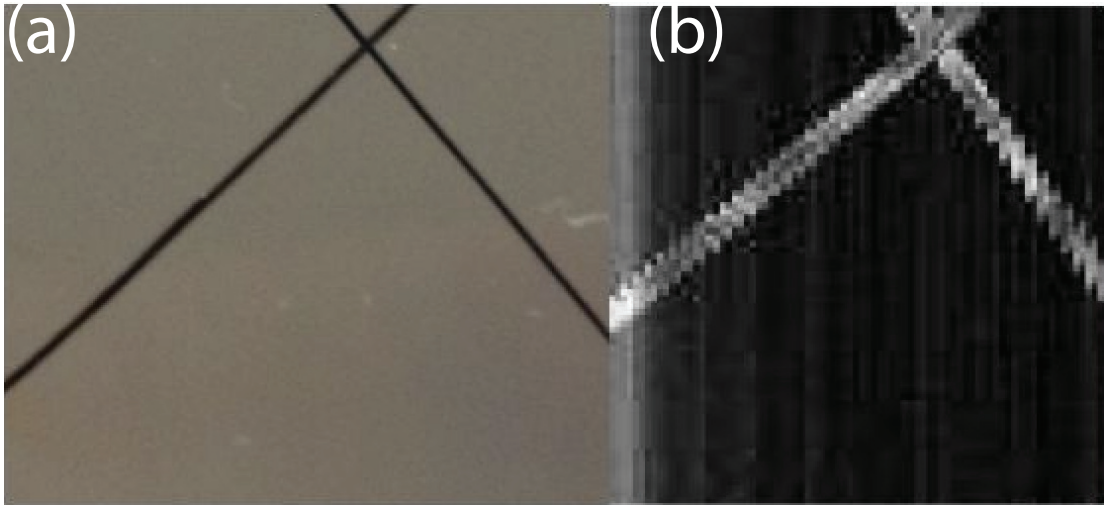


Figure 4.4. (a) The photography of a phantom including two horse tail-hairs to form a cross shape, (b) The photoacoustic image of the phantom illuminated with an optical wavelength of 1064 nm, power of 5 mW, a number of averaging of 16.

chosen due to its high optical absorption property providing ease of signal generation. The black ink was injected into a fiber tube with a diameter of 1 mm then it was fixed on a petri dish. The sample and a piezoelectric transducer (V384, Panametrics) with a 10 MHz center frequency were immersed in water with a source-detector distance of approximately 1 cm. We triggered the signal with an FPGA output of the fiber laser. After providing a stable experimental setup, we excited the sample with the fiber laser source at the optical wavelength of 1064 nm filtered from the supercontinuum output to generate photoacoustic waves. We used a 5x objective (LMH-5x-1064, Thorlabs) to focus the excitation light. Figure 4.2 shows an example of the generated photoacoustic signals from this sample. Furthermore, we used a horse tail-hair with a diameter of 375 μm again located in a petri dish to generate photoacoustic waves. An example of the generated signals is shown in Figure 4.3.

Apart from signal generation, we utilized the maximum amplitude projection (MAP) technique to reconstruct the image of an horse hair phantom. We prepared a phantom including two horse tail-hairs to form a cross shape inside a petri dish. Then, we scanned the phantom along the x-y plane with a step size of 100 μm. We averaged the signals over 16 consecutive signal cycles. We adjusted the optical power as 5 mW at 1064 nm from the supercontinuum output of the fiber laser. Figure 4.4a and Figure

4.4b show the photography of the phantom and the photoacoustic image corresponding to the phantom, respectively. This is a very early photoacoustic image obtained by our PAM system. The resolution of the image is not very high probably due the unstable experimental conditions, low number of averaging, and high step size in the scan. After this stage, we optimized the system in order to achieve higher resolved photoacoustic images.

4.2. Lateral Resolution of the PAM System

In order to determine the lateral resolution of our PAM system, we used the similar experimental setup mentioned in previous section and obtained the MAP image of a standardized resolution test target (USAF-1951, Thorlabs). We used the 5x objective to focus the light on Group 7 Element 6 of the target. A 2D raster scanning along the x-y plane in steps of 1 μm for an area of 300x330 μm^2 was performed for the region of interest (ROI) of the target. The acquired photoacoustic signals were averaged over 128 consecutive signal cycles. We again used the FPGA output to trigger the DAQ for synchronization. The data processing and image reconstruction were performed through a self-written MATLAB code. Figure 4.5a shows the optical microscopy image of the ROI and Figure 4.5b shows the photoacoustic image of the same region. The lateral full width at half-maximum (FWHM) value from the imaged highlighted well resolved bars (in Figure 4.5c) was determined as 2.68 μm, as shown in Figure 4.5d.

4.3. Multispectral PAM Applications

In this section, for the demonstration of our multiwavelength PAM system, Group 5 Element 6 of the test target was imaged with six different wavelengths of 532, 650, 697, 732, 785, and 880 nm that can be seen in Figure 4.6a, 4.6b, 4.6c, 4.6d, 4.6e, and 4.6f, respectively. These wavelength values except from 532 nm which was obtained by second harmonic generation (SHG), were filtered from the supercontinuum output of the laser for each experiment. A 10x objective (Plan Achromat, 0.25 NA, Olympus) was used to focus the light onto the relevant area. For comparison of the multiwavelength data, we have normalized each data set internally and used the same color palette for

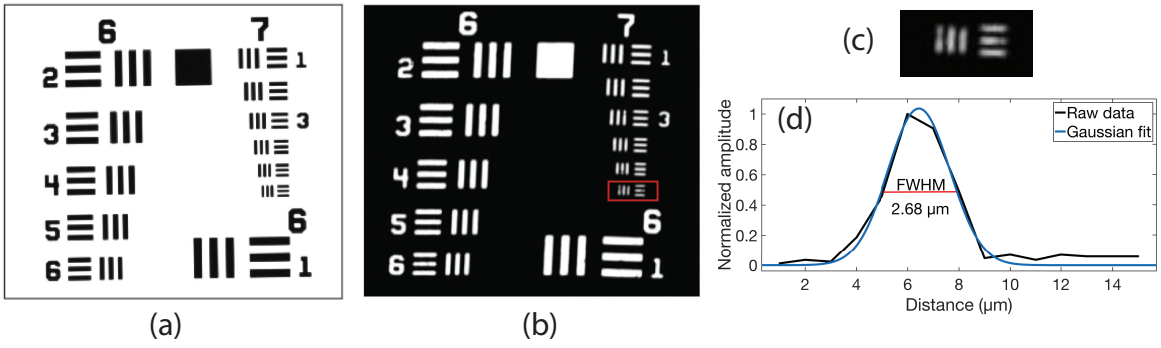


Figure 4.5. (a) Optical microscopy image, (b) Photoacoustic microscopy image of USAF resolution test target (Group 6 and 7), (c) Photoacoustic microscopy image of Group 7 Element 6, (d) FWHM of a line at Group 7 Element 6 from Gaussian fit (blue) of raw data (black).

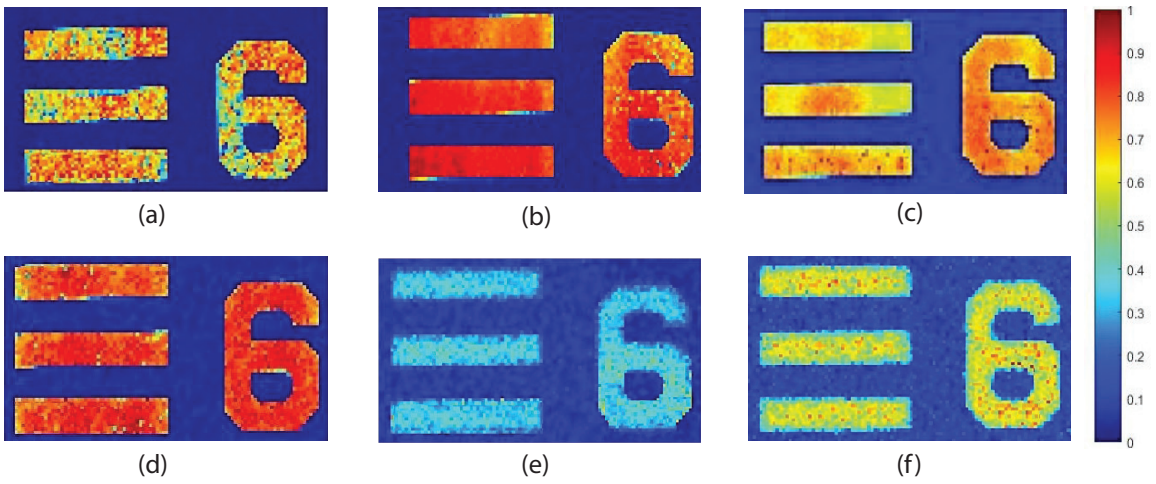


Figure 4.6. The photoacoustic image of Group 5 Element 6 scanned within an area of 56 x 101 μm^2 with steps of 1 μm acquired at optical wavelength (a) 532 nm from harmonic generation unit, (b) 650 nm, (c) 697 nm, (d) 732 nm, (e) 785 nm, and (f) 880 nm, respectively, from supercontinuum output.



Figure 4.7. The photoacoustic images of the phantoms comprising multiple polymide tubes filled with India inks of various colors (red, black, and green, respectively) with three different optical wavelengths of (a) 1064 nm, (b) 650 nm, and (c) 590 nm.

all images, nevertheless, the variation in the absolute optical signal is around 15%.

Furthermore, we performed multiwavelength imaging on phantoms comprising multiple polymide tubes with different diameters filled with India inks of various colors (red, black, and green). The supercontinuum was sent through a bandpass filter of intended wavelength before being focused onto the object. For focusing, the 10x objective was used. The tubes and the transducer of 3.5 MHz were immersed in water, then the sample was scanned along a line of length of 10 mm in steps of 10 μm. The reconstructed images of these phantoms are shown in Figure 4.7. The intensities of the generated photoacoustic signals from these three tubes were not same because of the fact that the absorption spectra of the inks with different colors are not same. Therefore, the photoacoustic images obtained with various wavelengths (1064 nm, 650 nm, and 590 nm, respectively) differ from each other, as expected. The system allows for spectral separation of signals from different absorbers based on their characteristic absorption spectra and can be used for functional imaging.

Quantum dots are also used as emerging contrast agents particularly in biomedical imaging applications [104–106] including photoacoustics [107, 108]. For this thesis, we concentrated on photoacoustic measurement of cadmium telluride (CdTe) quantum dots in toluene. We injected the quantum dots on a microscope well slide and closed it by a cover glass, then glued both glasses from their edges to prevent outflow of the solution. Here, we observed that the quantum dots aggregated to form a circular shape around the well leaving the inner area empty. Using the similar experimental setup

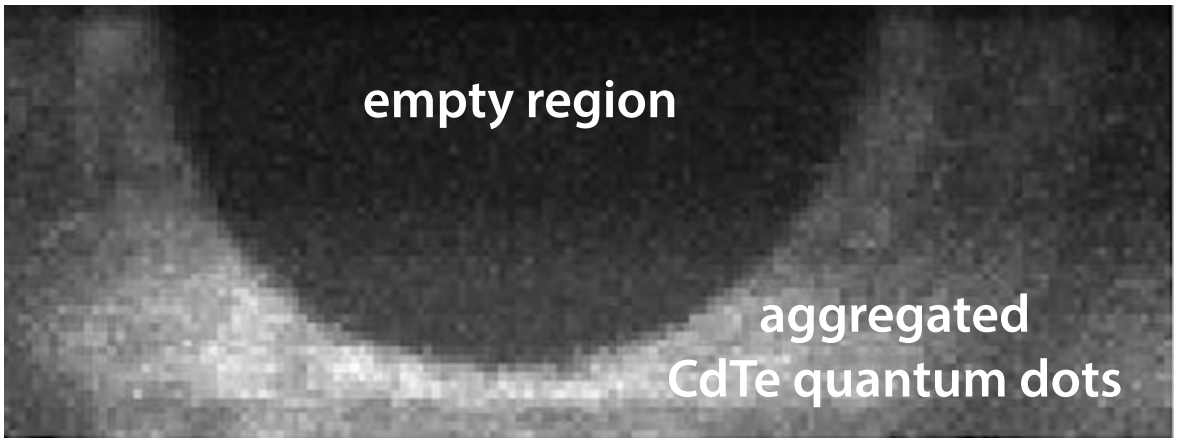


Figure 4.8. The photoacoustic image of the cadmium telluride (CdTe) quantum dots (in toluene) injected on a microscope well slide. The whiter region shows the quantum dots. The quantum dots are aggregated around the circular boundary of the well due to their aggregation property.

as in the ink case, we scanned the ROI including one half of the circular well and its surrounding. Figure 4.8 shows the photoacoustic image of the quantum dots in which they are aggregated on the circular boundary of the well, as expected.

We also worked with tissue-simulating phantoms prepared by agarose gel and polydimethylsiloxanes (PDMS) material. While the former is widely used in various experimental applications, the latter is a promising material for phantom studies to be used in PAM [109–111]. Although the acoustic attenuation in PDMS is high and it requires challenging preparation procedure by soft lithography, it has many advantages such as having a long-term stability with structural rigidity and allowing creation of microchannels within the material. In this thesis, we used two different PDMS-based microfluidic devices for our photoacoustic applications, particularly for the photoacoustic measurements of biological cells. The photographies of these two PDMS phantoms with different thicknesses (1 mm and 6 mm) and microchannel geometries are shown in Figure 4.9. To show the channels within the PDMS phantoms, we obtained the optical microscopy images of both that are shown in Figure 4.10.

To test the performance of the PDMS phantom on photoacoustic measurements, we have first conducted some experiments to image the black ink injected in a mi-

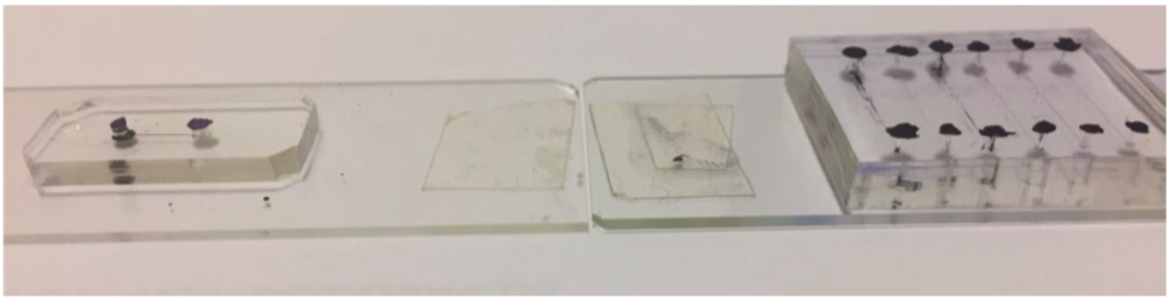


Figure 4.9. The photographies of the PDMS phantoms with different thicknesses (1 mm and 6 mm).

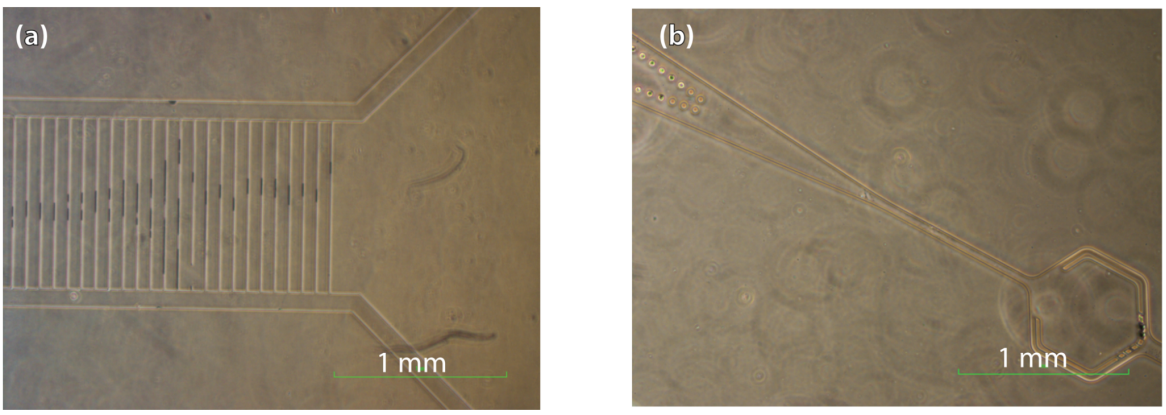


Figure 4.10. The photographies of the microchannels inside the PDMS phantoms.

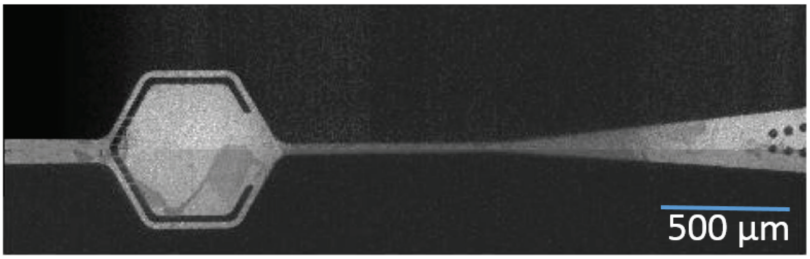


Figure 4.11. Photoacoustic image of a microfluidic device in PDMS phantom injected with a black India ink. The optical wavelength is at 1064 nm filtered from the supercontinuum output. The imaging area is 4x1 mm^2.

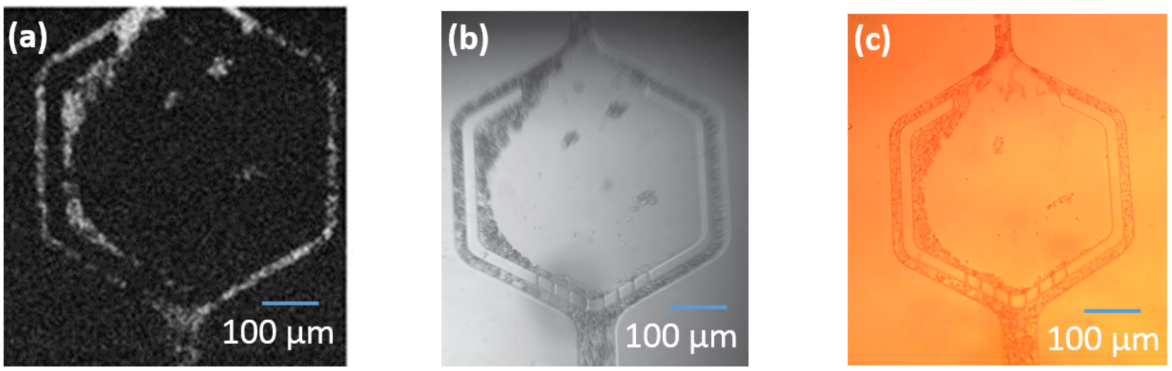


Figure 4.12. (a) The photoacoustic, (b) CCD, and (c) Optical microscopy image of red blood cells injected in a microchannel created in a PDMS phantom.

crochannel. After a careful sample preparation procedure, the phantom and the 3.5 MHz transducer were immersed in water with a 5 mm source-detector distance. We used the fiber laser for photoacoustic excitation at an optical wavelength of 1064 nm filtered from the supercontinuum output. Here, we used the 5x microscope objective to focus the light of 10 mW on the sample. Then, we performed a 2D raster scanning for an area of 4x1 mm^2 to collect the photoacoustic signals to obtain the image. Figure 4.11 shows the photoacoustic image of the microchannel loaded with the ink. Here, we collected the data by taking an average over 128 consecutive signals. Thus, we estimated the lateral resolution to be around 5 μm, the size of the pillars within the microchannel, by referencing the fact that they are distinguishable.

After this stage, we injected red blood cells (RBCs) into the microchannel to obtain the photoacoustic image using our PAM system. This time we used an optical wavelength of 532 nm from the harmonic generation unit of the fiber laser, with an

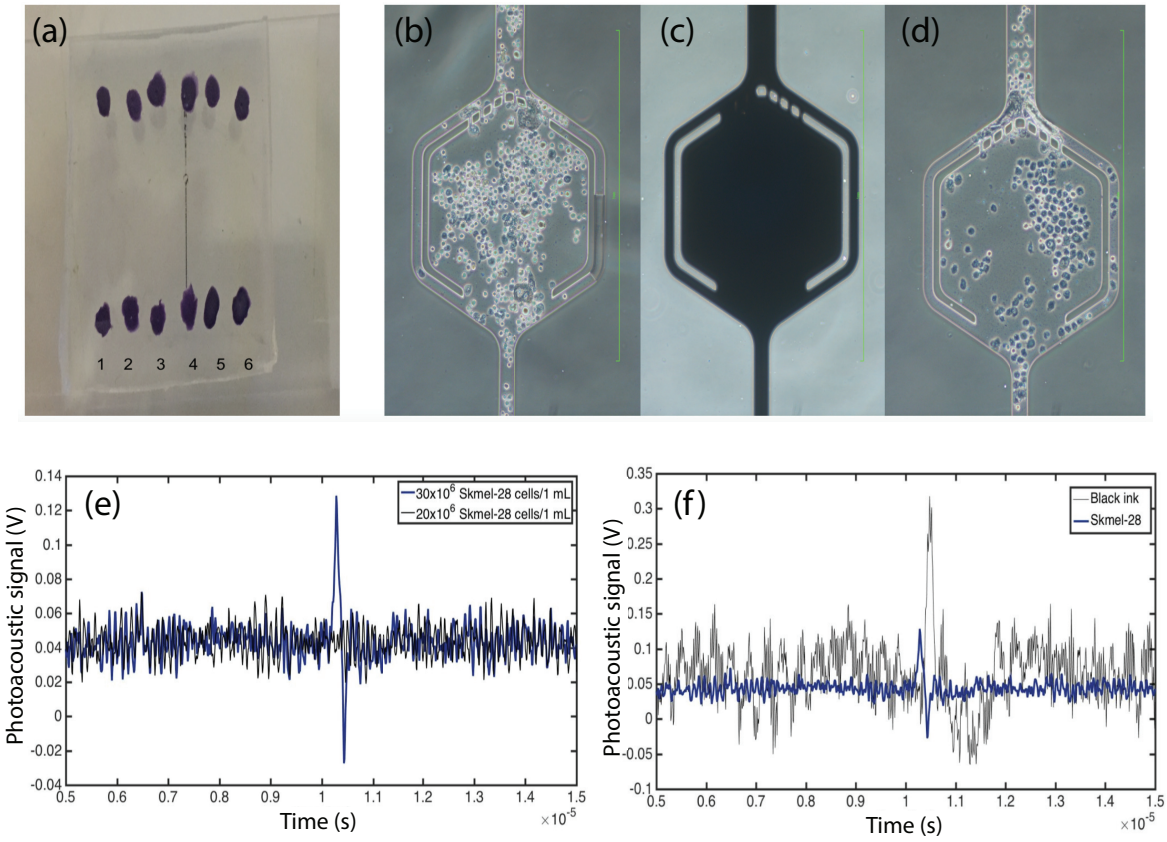


Figure 4.13. (a) The photography of a PDMS phantom including six microchannels. Optical images of (b) 3^{rd} (Skmel-28 with 30x10^6 cells/ml), (c) 4^{th} (black ink), and (d) 5^{th} (Skmel-28 with 20x10^6 cells/ml) channel. Comparative signals for (e) 3^{rd} and 5^{th} and (f) 3^{rd} and 4^{th} channel, taken at 532 nm with 50 mW power.

optical power of 15 mW. We used the 10x objective for focusing and scanning the ROI of the channel with an area of 600x600 μm^2. Figure 4.12a, Figure 4.12b, and Figure 4.12c show the photoacoustic image, CCD (charge coupled device) image, and optical microscopy image, respectively. Here, we recognize that the acoustic attenuation in PDMS material is high and causes a low SNR in the photoacoustic image.

In addition to all these applications, we also aimed at detecting the photoacoustic signals from Skmel-28 human malignant melanoma cells in which both the fiber laser and the OPO laser mentioned in Section 1.2 were used for photoacoustic excitation. Skmel-28 cell line was purchased from the American Type Culture Collection. Dulbecco's modified Eagle's medium containing 10% fetal bovine serum was used as the medium to grow the cells. In order to increase cell growth and viability, MEM

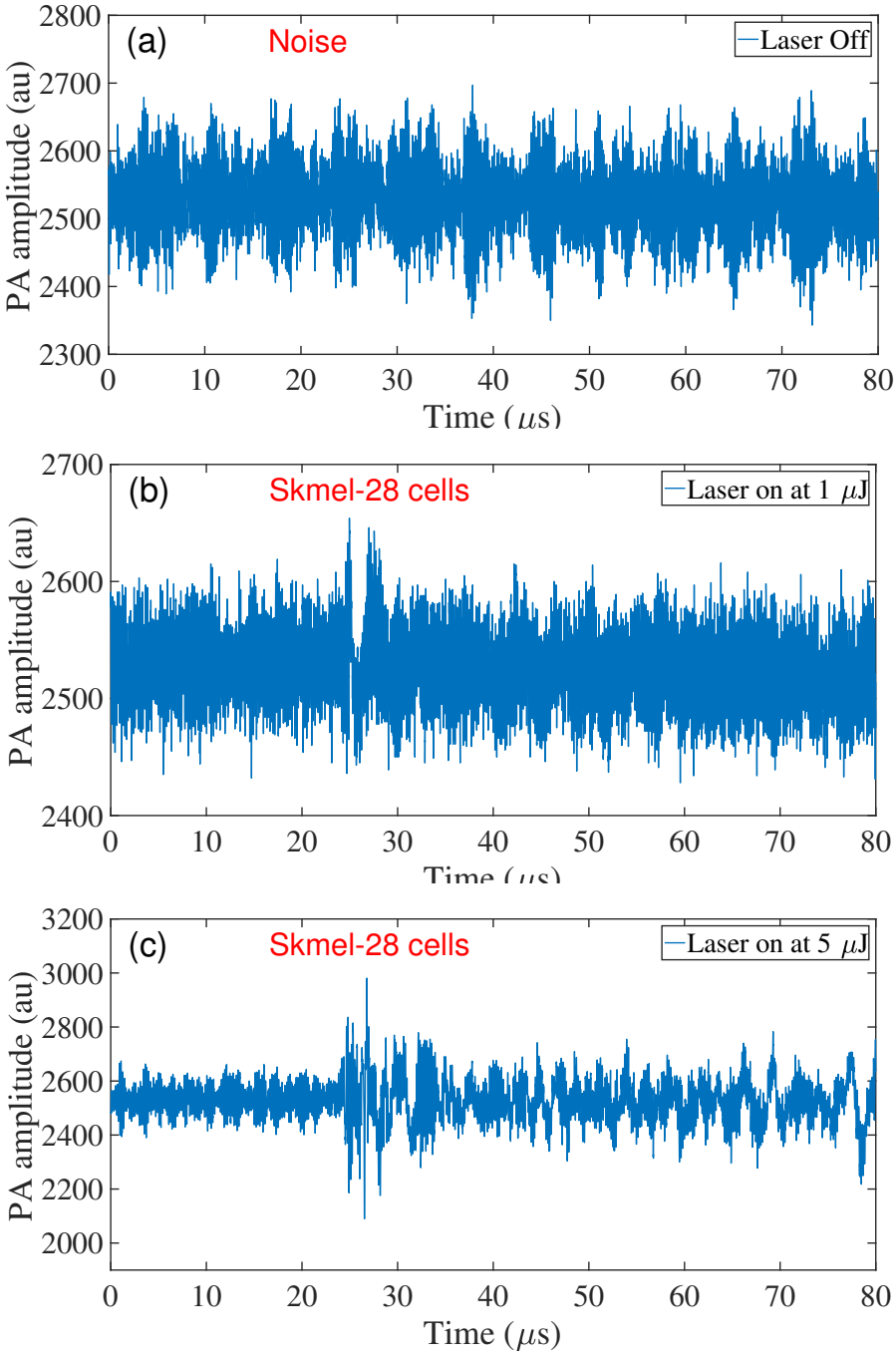


Figure 4.14. (a) The noise in the system. The photoacoustic signals arising from Skmel-28 cells (mixed with PBS) injected in an agar phantom excited by the OPO laser at 630 nm for pulse energies of (b) 1 μJ and (2) 5 μJ.

non-essential amino acids solution was added to the medium. Besides, a penicillin-streptomycin mixture was also added to prevent possible contamination. The cells were cultured in 100-mm tissue culture dishes with 10 mL growth medium at 37 °C within a 5% CO_2 humidified atmosphere for maintenance. Cell passaging was performed every two days with 0.05% trypsin/0.02% EDTA. The cells were counted with the help of an automated hemocytometer (Countess II FL Automated Cell Counter), then, in order to obtain certain concentrations, the counted cells were centrifuged at 2000 rpm for 2 minutes and diluted with corresponding volume of PBS (phosphate-buffered saline). Here, we again used PDMS phantoms to inject the cells. Figure 4.13a shows the PDMS phantom which includes six microchannels. We injected the Skmel-28 cells in four channels (1^{st}, 2^{nd}, 3^{rd}, and 6^{th}) with a concentration of 30x10^6, and in 5^{th} channel with a concentration of 20x10^6. Besides, we filled the 4^{th} channel with black India ink (Dr. Ph. Martin's Bombay Black, Salis International Inc., Golden, CO) to ensure the optical focus and compare the generated signals. Figure 4.13b, Figure 4.13c, and Figure 4.13d show the optical microscopy image of the 3^{rd}, 4^{th}, and 5^{th} channel, respectively. First, we used the fiber laser for the excitation at an optical wavelength of 532 nm with an optical power of 50 mW from the harmonic generation unit. Taking the 4^{th} channel including the black ink as reference for signal generation, we obtained photoacoustic signals from Skmel-28 cells. Figure 4.13e shows the recorded signals from the 3^{rd} and 5^{th} channels in which the later did not have enough number of cells to generate detectable photoacoustic signals. On the other hand, we detected photoacoustic signals from the former which had an higher concentration of Skmel-28 cells. Obviously, the amplitude of the signal depends on the number of cells within the microchannel.

In the experiments that we utilized the OPO laser for the excitation of Skmel-28 cells, we prepared an agarose gel phantom to house the cells. We formed several holes inside the agar with the help of microtiter plates during the cooling process of the gel. Then, we removed the plates from the agar, and injected the cells into the wells that formed after the plates were removed. Here, we injected only PBS into a well for signal comparison with the well of Skmel-28 cells. We filled the remaining gaps again with the agarose gel and waited about half an hour for the phantom to reach a stable

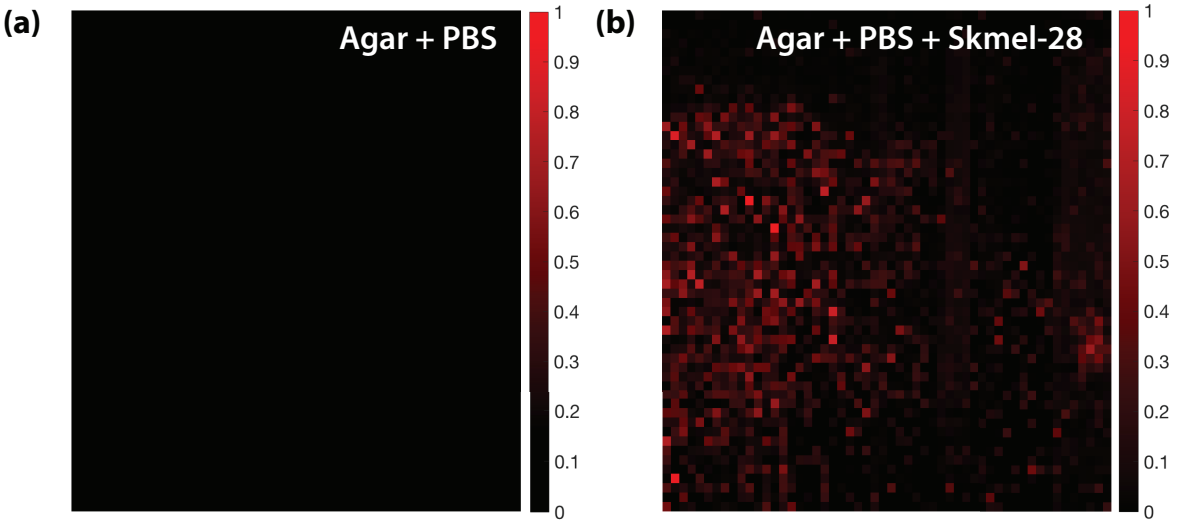


Figure 4.15. The relative photoacoustic images of two wells inside an agar phantom, one of them belongs to (a) PBS and the other belongs to Skmel-28 cells mixed with PBS.

structure. The sync-out of the power/cooling unit of the Nd:YAG laser was used to trigger the signal. The output of the OPO was adjusted to an optical wavelength of 630 nm. After the alignment procedure, we excited the cells to generate photoacoustic waves. The noise in the system is shown in Figure 4.14a. Figure 4.14b and Figure 4.14c show two separate photoacoustic signals obtained by pulse energies of 1 μJ and 5 μJ, respectively. Furthermore, we scanned the phantom to obtain its photoacoustic image which is shown in Figure 4.15. Here, Figure 4.15a and Figure 4.15b are the relative images while the former belongs to the well injected with only PBS, the latter belongs to the well of Skmel-28 cells mixed with PBS.

Additionally, we performed some photoacoustic measurements to image human red blood cells excited by the OPO laser. For this purpose, we embedded the RBCs into an agarose gel phantom in a petri dish. We formed a hole inside the agar again with the help of a microtiter plate during the cooling process of the gel. Then, we injected the RBCs within the plate and filled it with agar. Figure 4.16a shows the photography of the phantom while Figure 4.16b shows the optical microscopy image of the left part of the sample. Using an optical wavelength of 630 nm at 1 μJ, we scanned the ROI to obtain the photoacoustic image of the blood which is shown in 4.16c.

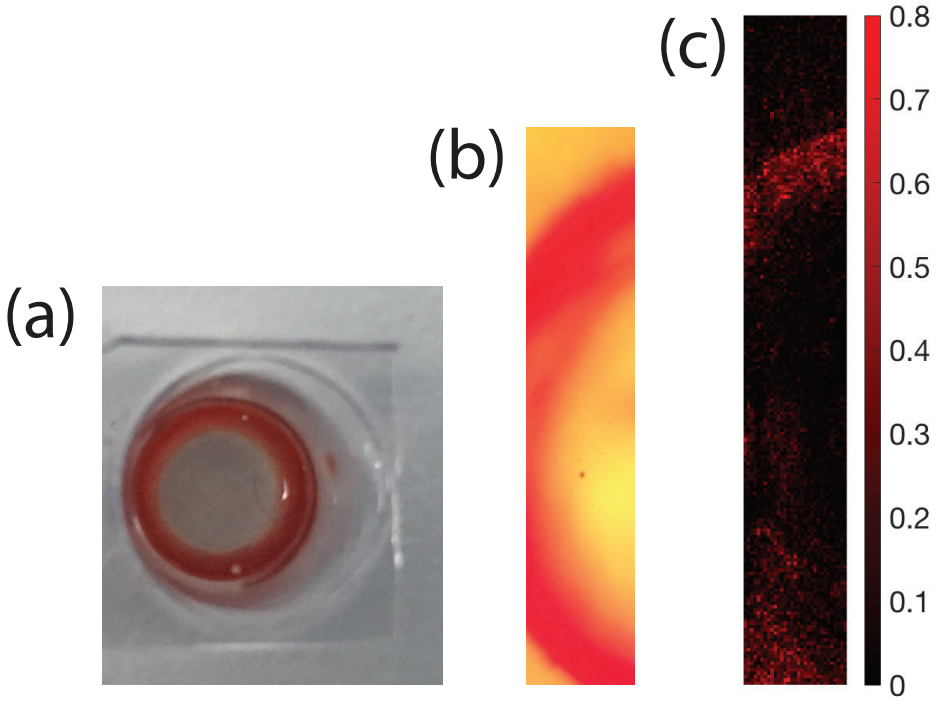


Figure 4.16. (a) Photography of human red blood cells inside a microtiter embedded in an agarose gel phantom, (b) Optical microscopy image, (c) Photoacoustic image of the region of interest, taken with an optical wavelength of 630 nm at 1 μJ using the OPO laser.

4.4. Discussion

Custom designed PAM systems are mostly advantageous to expand its application area because they allow to change the components within and to adjust the parameters of the system in accordance with the application type. Since both the excitation lasers and the detection devices are adjustable in our PAM system, we were able to conduct various applications presenting multispectral photoacoustic images of different types of samples having different sizes and absorption spectra. On the other hand, the lateral resolution of approximately 2 μm is quite good to be able to image single cells, which is a very challenging issue in photoacoustic applications. Single cell imaging requires using high frequency ultrasonic transducers [112, 113] and may be one of the future goals of our PAM system. In addition, we performed photoacoustic measurements of human RBCs and Skmel-28 cancer cells to test the performance of our system on in vitro applications, but different types of cells can also be measured in our PAM system thanks to its broadband frequency spectrum and other adjustable properties.

5. MICROCANTILEVERS EXCITED BY PULSED-LASER-INDUCED PHOTOACOUSTIC WAVES

Excitations of microcantilevers by laser-induced photoacoustic waves have recently been reported [114]. This excitation technique typically relies on the generation of photoacoustic waves from an optical absorber, followed by effective delivery of these propagating photoacoustic waves on the lever surface through the medium. An effective response of the microcantilever to the photoacoustic waves holds promise to actuate and characterize atomic force microscopy (AFM) cantilevers. Moreover, it may enable microcantilevers to be used as photoacoustic sensors, a substitute method for detecting small signals. Nonetheless, these potential applications call on a comprehensive understanding of the microcantilever response to the laser-induced photoacoustic waves.

Piezoelectric actuation [115–117] is a commonly used base-driven AFM actuation model in vacuum and ambient conditions. However, its applications are confounded by its peculiar limitations such as utilization of a bulky piezo-actuator mounted to the cantilever holder. This may cause spurious resonance vibrations [118] especially in liquid environment, mostly due to the resultant motion of the surrounding fluid. Although there are rigorous attempts [119] to eliminate or reduce these spurious peaks, it still remains as a difficult problem to be dealt with. Another common AFM actuation technique is the photothermal excitation [120], which is based on the direct illumination of the lever surface. However, this approach causes undesired thermal effects to occur on the microcantilever oscillation [114] and on the samples [121], making them be exposed to the laser beams and to the heat as well. Several attempts [122] have been done to eliminate this problem by situating the laser focus on a substrate at a distance from the clamped end, which is not possible with standard cantilevers. Electrostatic [123] and magnetic excitations [124] are other demonstrated techniques, but they require surface modifications, sophisticated microfabrication processes, and include bulky units, hampering the cost-effectiveness and practical utilization. Furthermore, an efficient alternative is the base-integrated piezoelectric actuator, but it requires high voltages

for actuation [125] and may suffer from repeatability and passivation problems [126]. In addition, acoustic actuation method either by a piezoelectric transducer [127] or an acoustic radiation pressure actuator [128] to generate acoustic waves is of particular interest, providing the advantage of non-contact interactions. Although constituting a promising approach, this technique is also hinged on the utilization of bulky units. In view of all that has been mentioned so far, one may appreciate why microcantilever actuation by laser-induced photoacoustic waves has taken its own place as an alternative technique. This method does not impose direct laser illumination onto the lever surface without sacrificing its non-contact interaction property that is provided by generation of the photoacoustic waves from an optical absorber.

On the other hand, the present literature shows the usage of cantilevers (with few millimeters in length and width, 5 to 10 microns in thickness) as photoacoustic sensors particularly in the photoacoustic trace gas analysis [129–131]. In these studies, photoacoustic generation is commonly based on a modulated laser light in which the source term for the excitation of cantilever is simply defined by a sinusoidal force [129]. However, when using pulse laser illumination to generate photoacoustic waves to be detected by cantilevers (for AFM actuation or photoacoustic detection), there remains a lack of knowledge about the response of microcantilever to the consecutive photoacoustic waves to achieve a more realistic model.

In this chapter, we investigated the excitations of two rectangular microcantilevers with different resonant frequencies (16.9 kHz and 505.7 kHz) in air medium using photoacoustic waves induced by a pulsed laser [132]. Instead of using a sinusoidal force for the excitation source, we used a purely N-shaped photoacoustic wave from an ideal spherical light absorber. A specific objective of the present study was to analyze the cumulative effect of these waves on the microcantilever oscillation characteristics by combining them consecutively with respect to pulse repetition frequency (PRF) of the excitation laser. This novel approach was expected to yield a better understanding of the response of microcantilever to the pulse-laser-induced photoacoustic waves.

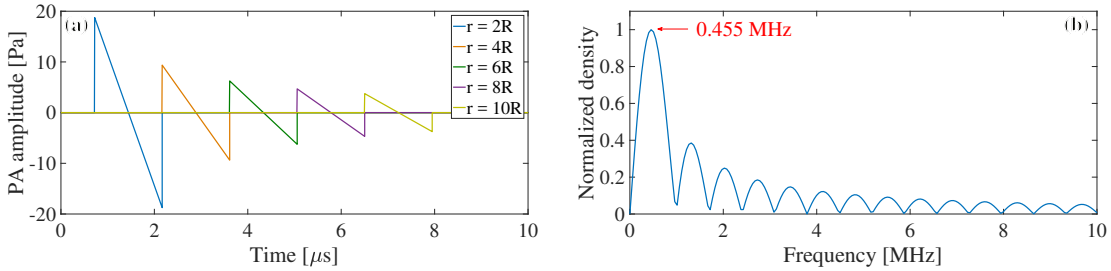


Figure 5.1. (a) The characteristic N-shaped photoacoustic waves generated from a spherical light absorber of $R = 250$ μm in radius for $p_0 = 75$ Pa. The amplitude of the photoacoustic wave decays with distance with respect to inverse distance law (see Equation 2.28), (b) Normalized power spectral density of this photoacoustic wave.

5.1. Theory and Method

In this section, we considered a spherical light absorber of 250 μm in radius to generate photoacoustic waves by delta heating, which was also discussed in Section 2.4. Now, we replotted the photoacoustic wave and its FFT counterpart for 250 μm size absorber shown in Figure 5.1a and Figure 5.1b, respectively. Here, we recall the fact that the amplitude of photoacoustic wave is decreasing with the distance from the absorber; thus, the distance between the absorber and the microcantilever is an important parameter for the oscillation amplitude.

On the other hand, wavelength of the generated photoacoustic wave is an important parameter to adjust the gap between the absorber and the cantilever. Particularly, a spherical absorber with a radius of 250 μm generates a photoacoustic wave that has a frequency of 0.455 MHz (with a peak amplitude) and other high frequency components up to several tens of MHz as shown in Figure 5.1b. A sound wave with a frequency of 0.455 MHz has a wavelength of about 760 μm in air, and the higher frequency components inside the wave packet has shorter wavelengths. Therefore, the distance between the absorber and the cantilever should be sufficiently large compared to the acoustic wavelength, so that its shape can be formed efficiently and the propagation along the gap is permitted.

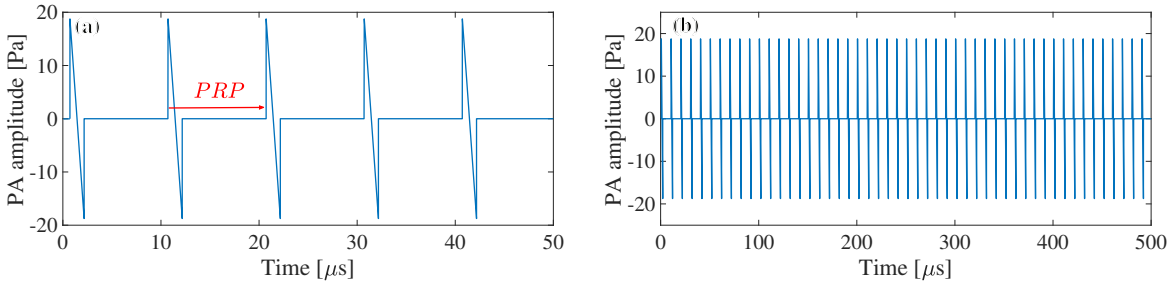


Figure 5.2. Two examples of numerically created consecutive photoacoustic waves comprising (a) 5 and (b) 50 waves, which are generated by a 100 kHz excitation laser for the values of $p_0 = 75$ Pa, $R = 250$ μm, and $r = 2R$. PA: Photoacoustic, PRP: Pulse repetition period.

5.1.1. The Creation of Consecutive Photoacoustic Waves

Investigating cumulative effects of the consecutive photoacoustic waves acting on the cantilever surface provides valuable information to characterize the cantilever oscillation, which cannot be obtained by regarding a single wave. To achieve such an approach, the single N-shaped photoacoustic wave was repeated numerically. The care was taken to present a realistic PRP by defining each period with respect to the time spanned between ascending peaks of the successive photoacoustic pulses. Figure 5.2a and Figure 5.2b show two examples of consecutive photoacoustic waves generated by a pulsed laser with PRF of 100 kHz for the values of $p_0 = 75$ Pa, $R = 250$ μm, and $r = 2R$. Note that the characteristic N-shaped photoacoustic wave is not perceptible in Figure 5.2b since the duration of the photoacoustic wave is very small compared to the PRP of the photoacoustic wave train. While the latter is simply the inverse of the PRF of the excitation laser, the former varies with respect to the radius of the light absorber and the speed of sound in the medium.

5.1.2. Microcantilevers Driven by Photoacoustic Pressure

The oscillation dynamics of the microcantilever is well described by the Euler-Bernoulli beam equation [133]. Here, the most straightforward approximation to model the dynamics is the one-dimensional simple harmonic oscillator under an external pho-

toacoustic excitation within a noisy environment as follows [129, 134]

$$m_{eff}\frac{d^2x}{dt^2} + \gamma\frac{dx}{dt} + k_{eff}x = F_{PA}(t) + \tilde{W}_N \tag{5.1}$$

where m_{eff}, x, γ, and k_{eff} are the effective mass, the vertical displacement of the free end, the damping coefficient, and the effective spring constant of the cantilever, respectively. The right hand side terms $F_{PA}(t)$ and $\tilde{W}_N$ are the driving forces which represent the force due to the photoacoustic pressure and the Gaussian white noise, respectively. The noise term $\tilde{W}_N$ is incorporated into the model to account for the main sources of noise such as shot noise of the photodetector, thermal noise of the cantilever, thermal drift in the system, and other ambient noise sources [135]. Energy transfer at the air-cantilever interface is based on the average force acting on the lever surface due to the photoacoustic wave packet. The approximation made here can be fairly regarded as realistic, since the duration of the photoacoustic wave is short, and the size of the microcantilever is small compared to the width of the photoacoustic wavefront. In addition, acoustic attenuation can also be taken into account. However, it is negligible for small distances (particularly for such frequencies). Thus, the plane wave approximation for the interaction between photoacoustic pressure wave and cantilever surface leads to a uniform pressure load on the cantilever surface such that the force is simply $F_{PA}(t) = P(t)A_{lever}$ where $P(t)$ is the photoacoustic wave as a function of time t at a certain distance $\mathbf{r}$, and A_{lever} is the one-side surface area of cantilever. Hence, the related force term due to the consecutive photoacoustic waves as a function of time can be defined as

$$F_{PA}(t) = \begin{cases} F_{PA} & \text{for } t{=}n \times PRP \text{ where n = 0, 1, 2,...} \\ 0 & \text{otherwise} \end{cases} \tag{5.2}$$

where $PRP = 1/PRF$. Note that for a conventional dynamic AFM model, in addition to the driving force, the interaction force between tip and sample surface is considered. Nevertheless, we use a cantilever clamped at one end and has no interaction with any sample on its free end. However, it is driven only by the random noise and the force due to external consecutive photoacoustic pressure waves separated by the PRP as

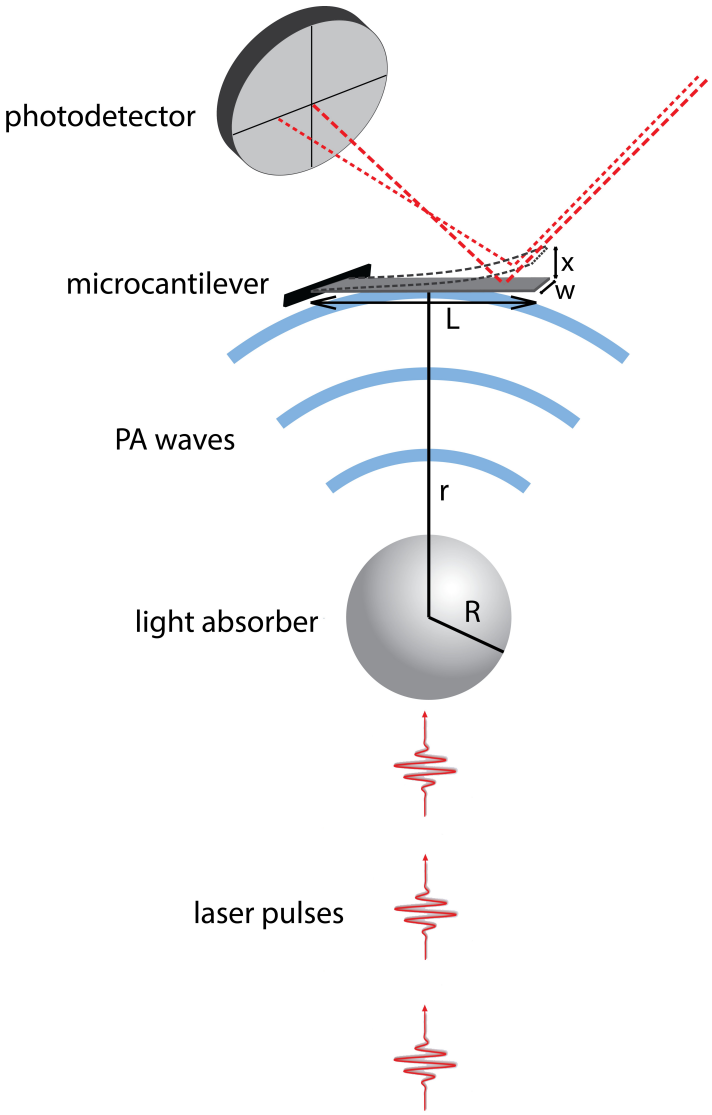


Figure 5.3. Schematic illustration of the setup for the microcantilever excitation by pulsed-laser-induced photoacoustic waves generated from a spherical light absorber.

shown in Figure 5.3.

The effective mass of cantilever for this case is defined as $m_{eff} = 0.647 m_{lever}$ [130] such that $m_{lever} = \rho_{lever} Lwh$ where L, w, and h are the length, width, and thickness of cantilever, respectively; and ρ_{lever} the density of cantilever material. Furthermore, the effective spring constant k_{eff} for the uniform pressure distribution is [130, 136]

$$k_{eff} = \frac{2}{3} Ew \left(\frac{h}{L}\right)^3 \tag{5.3}$$

where E is the Young's modulus for the cantilever material. The resonance frequency of the cantilever is then described as

$$f = \frac{1}{2\pi}\sqrt{\frac{k_{eff}}{m_{eff}}}. \tag{5.4}$$

It can be shown the above definition of the resonance frequency yields an equivalent result to that obtained by the Euler-Bernolli beam theory for the first mode [114, 134].

5.1.3. Oscillating Cantilever in a Viscous Fluid

We need to analyze the system in a medium due to excitation of microcantilever by photoacoustic waves. Besides, the light absorber and cantilever should be located in the same medium to avoid acoustic impedance mismatch between boundaries, where acoustic wave can be attenuated considerably due to the strong reflection. When oscillating in a viscous fluid, the resonant frequency of cantilever, f_{fluid}, decreases compared to the value in vacuum, f_{vacuum}, due to the drag force of the surrounding fluid acting on cantilever surface. The shift in the resonant frequency in a fluid is defined as [137, 138]

$$f_{fluid} = f_{vacuum}(1 + \frac{\pi\rho_{fluid}w}{4\rho_{lever}h})^{-\frac{1}{2}} \tag{5.5}$$

where ρ_{fluid} is the density of fluid. The resultant motion of the surrounding fluid due to the vibration of cantilever has considerable effects on the oscillation behavior, particularly in liquids. The effect is generally modeled considering an additional mass, m_{added}, to the cantilever's original mass. Hence, this additional mass results in an increase in the damping coefficient of the oscillation. While this effect in air can be negligible [139], there is value in considering that in the fluid particularly for high frequency cantilevers. For a rectangular cantilever beam, the additional mass term m_{added} and the resultant damping coefficient γ can be derived by the following expressions [139]

Table 5.1. Cantilevers used for simulations.

Cantilever	**L** (μ**m**)	**w** (μ**m**)	**h** (μ**m**)	k_{eff} **(N/m)**	**f (kHz)**
C1	450	30	2.5	0.58	16.9
C2	125	40	5.75	438.6	505.7

$$m_{added} = \rho_{fluid}\frac{\pi}{4}w^2 L\Gamma', \tag{5.6}$$

$$\gamma = \rho_{fluid}\frac{\pi}{4}w^2 L\omega_{fluid}\Gamma'' \tag{5.7}$$

where ω_{fluid} is the pulsation in fluid, and the parameters Γ' and Γ'' are defined by

$$\Gamma' = a_1 + a_2\frac{\delta}{w}, \tag{5.8}$$

$$\Gamma'' = b_1\frac{\delta}{w} + b_2(\frac{\delta}{w})^2 \tag{5.9}$$

forming a hydrodynamic function $\Gamma_{hydro} = \Gamma' + i\Gamma''$ for the oscillating cantilever. For an infinitely thin rectangular beam, the above parameters are approximated [139] for $a_1 = 1.0553$, $a_2 = 3.7997$, $b_1 = 3.8018$, $b_2 = 2.7364$. The length parameter δ corresponding to the fluid is defined by

$$\delta = \sqrt{\frac{2\eta}{\rho_{fluid}\omega_{fluid}}} \tag{5.10}$$

that gives the thickness of the thin viscous layer surrounding the cantilever in which the velocity decreases by a factor of $1/e$. The parameter η is the fluid viscosity. More detailed information about the additional mass and the resulting damping including the hydrodynamic function parameters can be found elsewhere [138, 139].

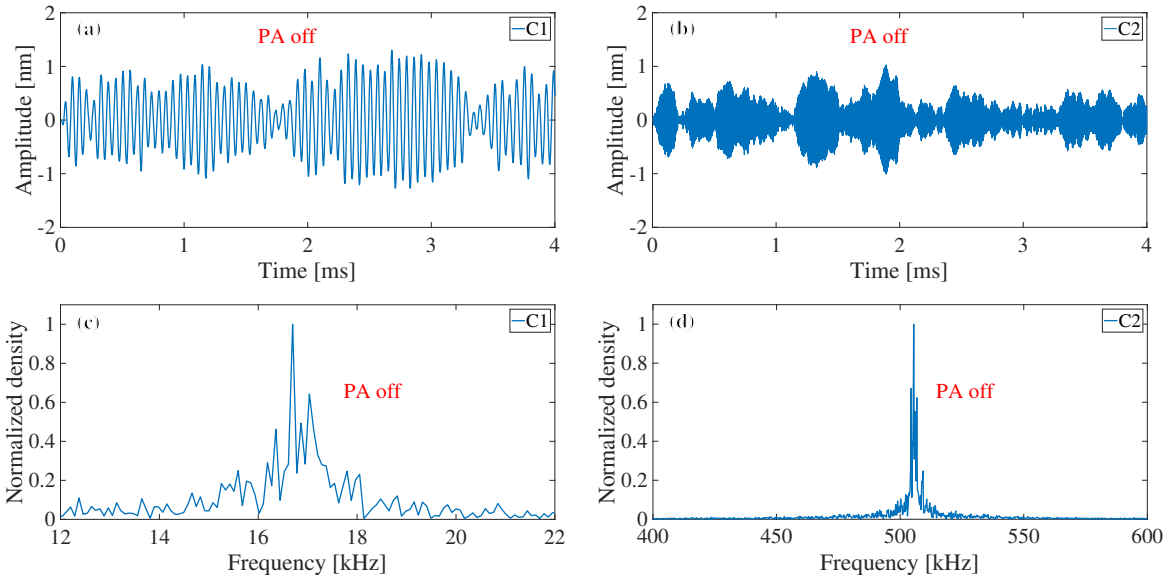


Figure 5.4. (a)-(b) Random oscillations of the cantilevers in time domain modeled by the Gaussian white noise with an RMS value of approximately 1 nm, (c)-(d) the corresponding normalized power spectral densities calculated by taking the FFT of these time domain random oscillations. PA: Photoacoustic.

5.2. Results

In order to simulate the oscillation behavior of the microcantilever, the related second-order differential equation (in Equation 5.1) was numerically solved by using the finite-difference method in MATLAB (Mathworks Inc., Natick, MA). The position and the velocity of the cantilever were assumed to be zero as an initial condition where the first photoacoustic wave reaches the cantilever surface. The simulations were performed in air environment at a temperature of 25 °C for two rectangular shaped silicon cantilevers C1 and C2 with different sizes and resonant frequencies listed in Table 5.1. The density, viscosity of air, and the speed of sound were taken as 1.184 $\mathrm{kg\,m^{-3}}$, 1.844×10^{-5} Pa s, and 346 $\mathrm{m\,s^{-1}}$, respectively. Also, the Young's modulus and density of silicon were taken as 169 GPa [140] and 2329 $\mathrm{kg\,m^{-3}}$ [141], respectively.

First, the random oscillations of the microcantilevers in the absence of the external photoacoustic waves (PA off) were analyzed. The root mean square (RMS) of the white noise including the all noise sources mentioned before was adjusted around 1 nm for both cantilevers. Here, the effects of the thermal noise of the cantilevers were

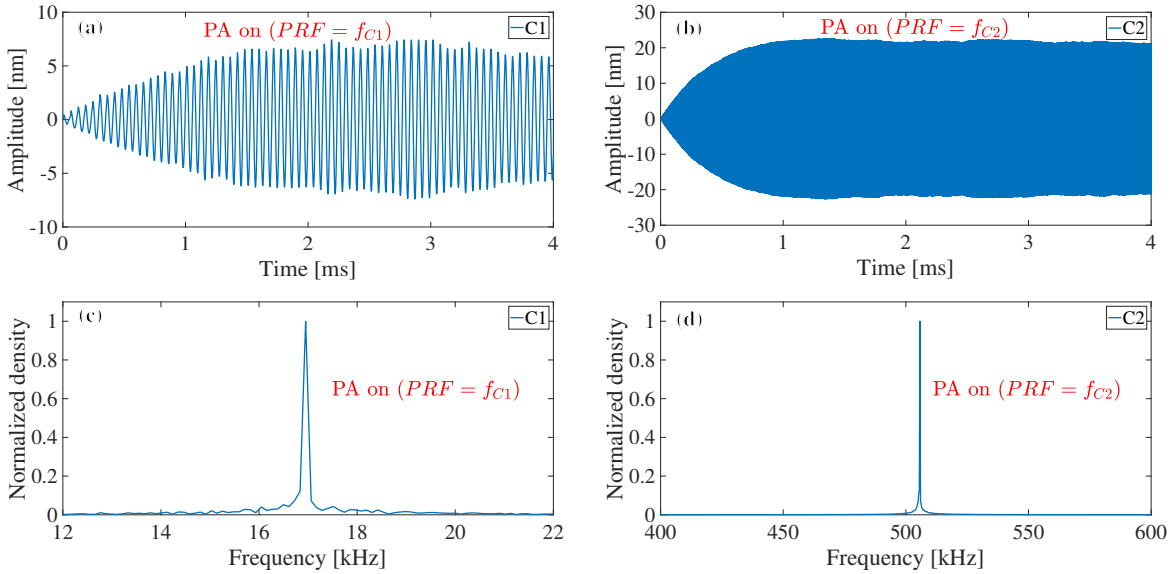


Figure 5.5. (a)-(b) The responses of the cantilevers to the consecutive photoacoustic waves when the PRF of the excitation laser matches to the fundamental resonant frequency, (c)-(d) the corresponding normalized power spectral densities calculated by taking the FFT of these time domain oscillations. PRF: Pulse repetition frequency.

ignored by considering the shot noise as the dominant noise source in our system. The simulated random oscillations with respect to time up to 4 ms are shown in Figure 5.4a and 5.4b. Next, the fast Fourier transform (FFT) of the random oscillations was taken, which reveals the power spectral density shown in Figure 5.4c and 5.4d for C1 and C2, respectively. Notice that C2 has a higher resonant frequency than C1, leading to a resonance curve with higher quality as expectedly.

The oscillation behaviors of the microcantilevers in the presence of the external photoacoustic waves (PA on) were investigated. Figure 5.5a and 5.5b show the oscillations with respect to time (again up to 4 ms) response to the PRF of the excitation laser that is equal to the natural resonance frequency values f_{C1} and f_{C2} of C1 and C2, respectively. As can be seen, when the PRF matches to the resonant frequency, the oscillation amplitude maximizes in a short time and then exhibits a steady-state behavior. Here, the radius of the light absorber was taken as 250 μm, and the initial photoacoustic pressure as 75 Pa on the surface of the absorber. The distance of the cantilever to the center of the spherical absorber was considered as 2000 μm which is

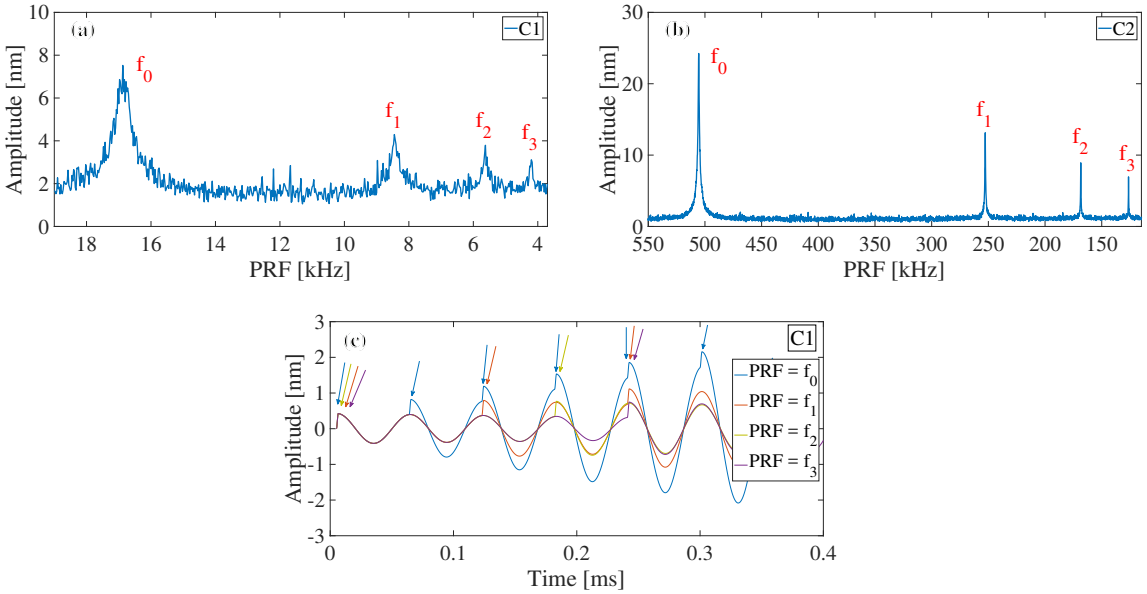


Figure 5.6. (a)-(b) Frequency response curves corresponding to the fundamental resonant frequencies and their lower harmonics up to 3^{rd} order for C1 and C2, respectively, (c) the time domain oscillations of C1 up to 0.4 ms driven by f_0, f_1, f_2, and f_3, in which the colored arrows show the inclusion of the photoacoustic waves.

larger than the acoustic wavelength, and ensures plane-wave approximation (e.g., after being emitted from an absorber with a radius of 250 μm and propagated through the medium for 1750 μm, the photoacoustic wavefront's interaction with the surface of the cantilevers considered in the present study can be fairly presumed as planar). Each single photoacoustic pressure wave has an amplitude of 4.7 Pa on the cantilever located at this distance (see Figure 5.1a). Furthermore, Figure 5.5c and Figure 5.5d show the FFTs of the oscillations at the resonance in which the clear maximums of the spectral densities correspond to the PRFs that are equal to the resonant frequencies.

Cantilevers can be excited to oscillate at relatively higher amplitudes by setting PRF of the laser to the integer fractions of the cantilever's fundamental frequency f_0. Each division of fundamental frequency by nth integer fraction gives nth lower harmonic frequency f_n. Figure 5.6a and Figure 5.6b show the maximum oscillation amplitudes obtained for each PRF within a range that encompasses driving frequencies up to 3^{rd} order of C1 and C2, respectively. Note that to obtain each of these data points, driven oscillations were computed with a high sampling rate, which imposes a considerable

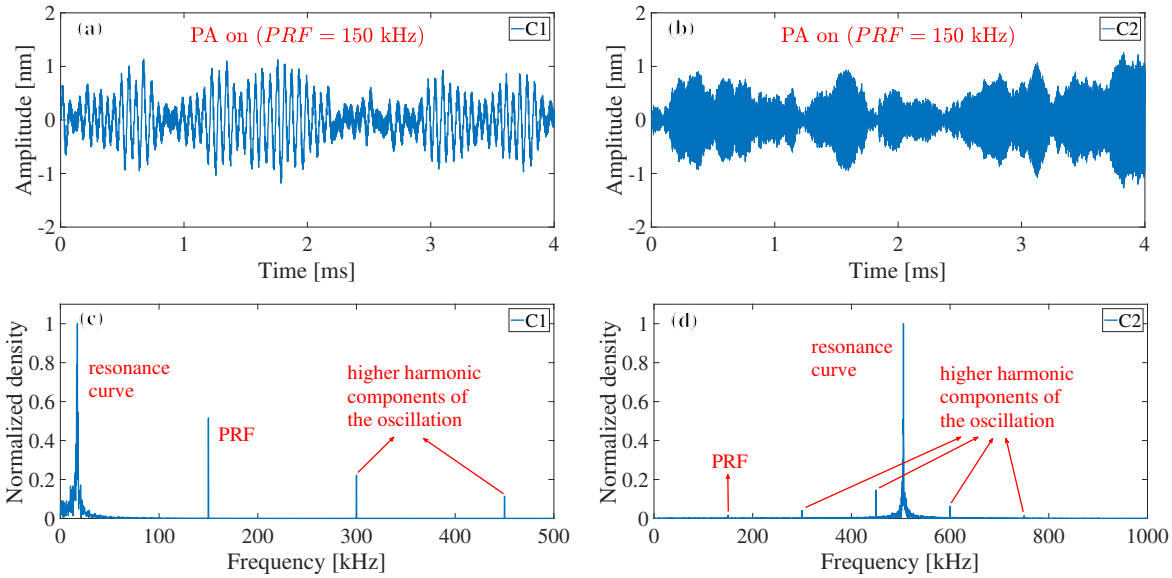


Figure 5.7. (a)-(b) The responses of the cantilevers to the consecutive photoacoustic waves with a repetition frequency of 150 kHz that does not match to any harmonic values of both cantilevers, (c)-(d) the corresponding normalized power spectral densities calculated by taking the FFT of these time domain oscillations.

computational overhead. Regarding the memory limits of the hardware available and the encompassed range of driving frequencies, PRF step sizes of 25 Hz and 50 Hz were selected to extract resonance curves for C1 and C2, respectively. The amplitudes of the curves decrease as the harmonic value increases as expected. For a better understanding of the physical origin of the effective response of the cantilever to the lower harmonic frequencies emerged in Figure 5.6a and Figure 5.6b, it is important to observe time domain oscillations (without noise) of the cantilever by applying PRF at these lower harmonic frequencies. The consecutiveness of the photoacoustic waves (PRP) plays an important role in determining the oscillation amplitude (see Figure 5.6c). When the cantilever is driven by f_0, the magnitude of the oscillation is elevated at its each period. Whereas it is driven by f_1, which equals to the half of f_0, the increment of the oscillation magnitude occurs once in two oscillation periods.

Off-resonance excitation of the cantilever leads to an oscillation at very low amplitudes. For example, the oscillations driven by the PRF of 150 kHz which is above of the resonance value of C1, below of the resonance value of C2, and does not correspond

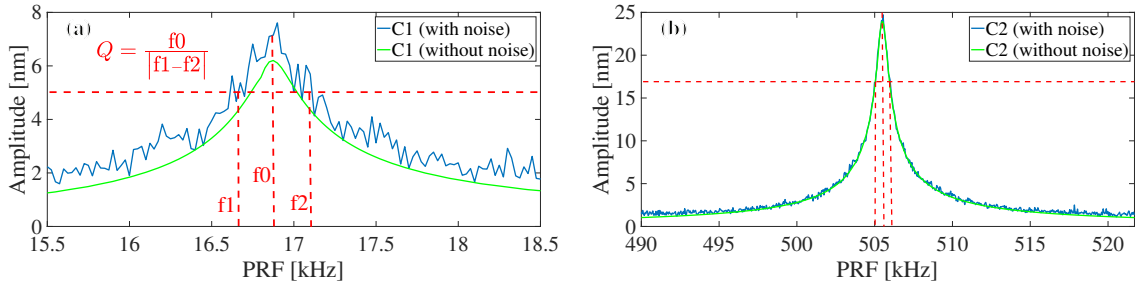


Figure 5.8. Frequency response curves of the microcantilevers simulated with and without noise. The correct positions for the vertical intersections for the data with noise were obtained by the data without noise. Then, the horizontal red lines correspond to $1/\sqrt{2}$ of the peak amplitude values of the curves. Q: Quality factor.

to any harmonic values for both, are shown in Figure 5.7a and Figure 5.7b. Notice that the oscillations with respect to time behave like random noises for both cantilevers in the manner of amplitude and characteristic. Besides, the normalized spectral densities shown in Figure 5.7c and Figure 5.7d for C1 and C2, respectively, reveal the characteristics of the oscillations. One can see that the densities corresponding to the driving frequency (i.e., PRF) and its resultant harmonics remain low compared to the resonance curve which indicates the random noise level. Therefore, the repetition rate of the photoacoustic waves, or the PRF of the excitation laser, has remarkable effects to drive the microcantilever effectively.

To obtain the quality factors of the cantilevers for the fundamental resonance frequencies, the frequency response curves (with and without noise) were utilized shown in Figure 5.8a and Figure 5.8b. These resonance curves were obtained by iterating PRF with a step size of 25 Hz within the respective ranges and recording the maximum oscillation amplitude for each iteration. The resonance values were determined to be 16.8 kHz and 505.5 kHz, which agree well with the theoretical calculations (see Table 5.1), with quality factors of 40 and 581 for C1 and C2, respectively.

The resonance amplitudes as a function of the distance between the optical absorber and the microcantilever were also investigated as shown in Figure 5.9a and Figure 5.9b. The oscillation amplitudes decay according to inverse distance law due to

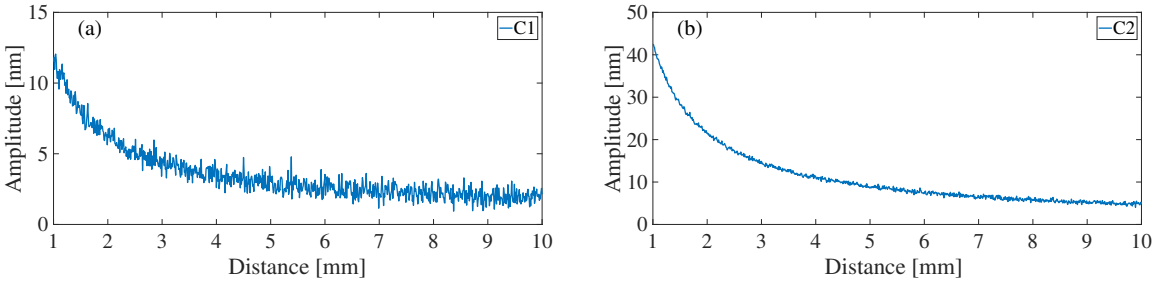


Figure 5.9. Oscillation amplitudes of the microcantilevers as a function of the distance between cantilever and the surface of the spherical absorber.

the fact that photoacoustic wave loses its power with distance as expected (see Figure 5.1a). It should be indicated here that when the distance is equal to an integer multiple of the half of the acoustic wavelength, a standing wave can be generated which may provide an easier energy transfer on the microcantilever, although the resultant increase in the oscillation amplitude is not remarkably high in this particular condition [114]. However, an analysis that examines the reflected sound wave from the lever surface should be performed to observe this effect which is not covered in our model that includes a wave propagation in one direction onto the microcantilever.

5.3. Discussion

The present study was designed to investigate microcantilever excitation by simulating pulsed-laser-induced photoacoustic waves generated from a spherical light absorber. The analysis of the cumulative effects of the consecutive waves on microcantilever oscillation undertaken here compromises a novel approach to such investigation. Both time and frequency domain results indicate that various standard AFM cantilevers can be effectively excited (e.g., driving at resonant or any other desired frequency) with steady-state oscillations and can be characterized (e.g., determining resonant frequency and quality factor from PRF response curves). Given that the most common types of microcantilever materials, e.g., silicon, silicon-nitride, gold, aluminum, etc., are profoundly reflective to acoustic waves, they can be utilized for actuation and characterization of AFM cantilevers or photoacoustic signal detection without the need of special coating on cantilever, or complex microfabrication processes.

We also indicate that microcantilevers can be used to detect small photoacoustic signals with the help of an increase in the oscillation amplitude by the cumulative effects of consecutive photoacoustic waves when working at the resonant frequency. While a single photoacoustic wave yields a deflection of about 0.43 nm for C1 and 0.07 nm for C2, which are not easily measurable levels within a noisy environment (e.g., by a four quadrant photodetector), the consecutive photoacoustic waves provide deflections of about 7 nm for C1 and 24 nm for C2 at the resonance (see Figure 5.5a and Figure 5.5b). This enhancement in the oscillation amplitude may be favorable for the detection of small photoacoustic signals which is not possible by the traditional detection tools.

Differential acoustic impedance of the absorber and the surrounding medium distorts the N-shape of the photoacoustic waves, and manipulates their propagation characteristics [142]. This condition has been commonly reported to challenge a non-contact photoacoustic detection in air medium [143–146]. In this regard, air-coupled materials such as aerogels [147,148] can be considered to be promising for utilizing in the medium considered in the present study, given that they have an acoustic impedance value around 0.01 MRayl [149,150], which is comparable to that of the air. Apart from the excitation in air medium, excitation in another viscous fluid such as water, which may possibly be necessary for AFM actuation or photoacoustic measurements, includes similar calculations mentioned in Section 5.1.3. However, the shift in the resonant frequency in water will be high due to strong hydrodynamic damping effect. Hence, oscillation amplitude will remain low even at the resonance, and may be below the measurable level. Besides, it may be possible to obtain oscillations at sufficiently high amplitudes in water as well. This can be achieved when cantilevers with frequencies in the MHz level are used, or photoacoustic waves are generated with higher pressure values by increasing the excitation laser energy and/or light absorption. It is worth noting that the noise level was set around 1 nm in this study. Therefore, there is still room for the improvement of minimum detectable level by the utilization of an experimental setup with a reduced noise level [151] that allows measuring smaller displacements and pressure values.

Possible exposure of the microcantilever to the pulsed-laser light which may not be completely shadowed by the photoacoustic absorber can be problematic. This is because it can manipulate the oscillation of microcantilever. Nevertheless, this effect can be eliminated with the precise alignment of the laser. On the other hand, such experimental setups cannot be easily obtained using commercial AFMs since they do not have enough space around the microcantilever for the photoacoustic instrumentation. Custom-made portable AFM heads [152] can permit configurations in which the excitation setup can be integrated to the system. In addition, tunability of the laser PRF plays an important role in the efficiency of the photoacoustic excitation. While this property is commonly not available in commercial lasers, custom developed fiber lasers can be equipped with it, permitting tunability of the PRF even up to MHz levels [6]. In conclusion, these needs highlight the importance of the advancements in the custom made AFM instrumentations and lasers, indicating a new potential application field.

The energy transfer at the air-cantilever interface in the present study is merely based on a uniform pressure distribution, which allows us to use plane-wave approximation for the interaction between photoacoustic wavefront and lever surface. This approach can be considered as realistic for this scenario in which the width of the wavefront at the interface is large enough compared to the length of the cantilever. A limitation of this study is that this assumption would be very rough for relatively small absorbers in close regions, where both the energy transfer and oscillation parameters should be modified.

6. DEVELOPMENT OF A CUSTOM-DESIGNED ATOMIC FORCE MICROS-COPY HEAD FOR ACOUSTIC AND PHOTOACOUSTIC SIGNAL DETECTION

In this chapter, we report a custom-designed atomic force microscopy (AFM) head system for both acoustic and photoacoustic signal detections utilizing microcantilevers as pressure sensors. The system allows such detections both in air and liquid environment. So, we performed experiments both in air and water medium. The air-coupled detection presents so-called non-contact detection taking the advantages of working without coupling medium to avoid the acoustic impedance mismatch between the boundaries. On the other hand, the water-coupled detection presents a potential alternative to the conventional detection methods providing a more sensitive detection. In order to test the performance of our system, we first detected acoustic signals arising from a headset that is controlled via a computer. Then, we focused on the detection of photoacoustic signals generated from black ink phantom on a petri dish. Here, we used the OPO laser mentioned in Chapter 1 as the photoacoustic excitation source.

6.1. Materials and Methods

The AFM head is custom-designed and can be operated for acoustic-photoacoustic detection as well as AFM imaging. A similar example of this custom system has recently been reported, which shows the feasibility of the system in AFM applications [152]. The base of the head is a custom-designed 3D-printed apparatus including the specified locations for integrating the instruments to be used for acoustic and photoacoustic detection. The cantilever holder is screwed to a piezo actuator (P-841.1, Physik Instrumente GmbH) from its bottom so that the piezo actuator is also screwed to the head from its top. Here, the piezo actuator is utilized for its self-applications for not only AFM actuation but also the determination of the deflection sensitivity of the cantilever relative to the applied force. A fiber-pigtailed laser diode ($\lambda = 650\,\text{nm}$, Oz Optics Ltd. Ottowa, Canada) is fixed on the top of the AFM-head with the help of a kinematic

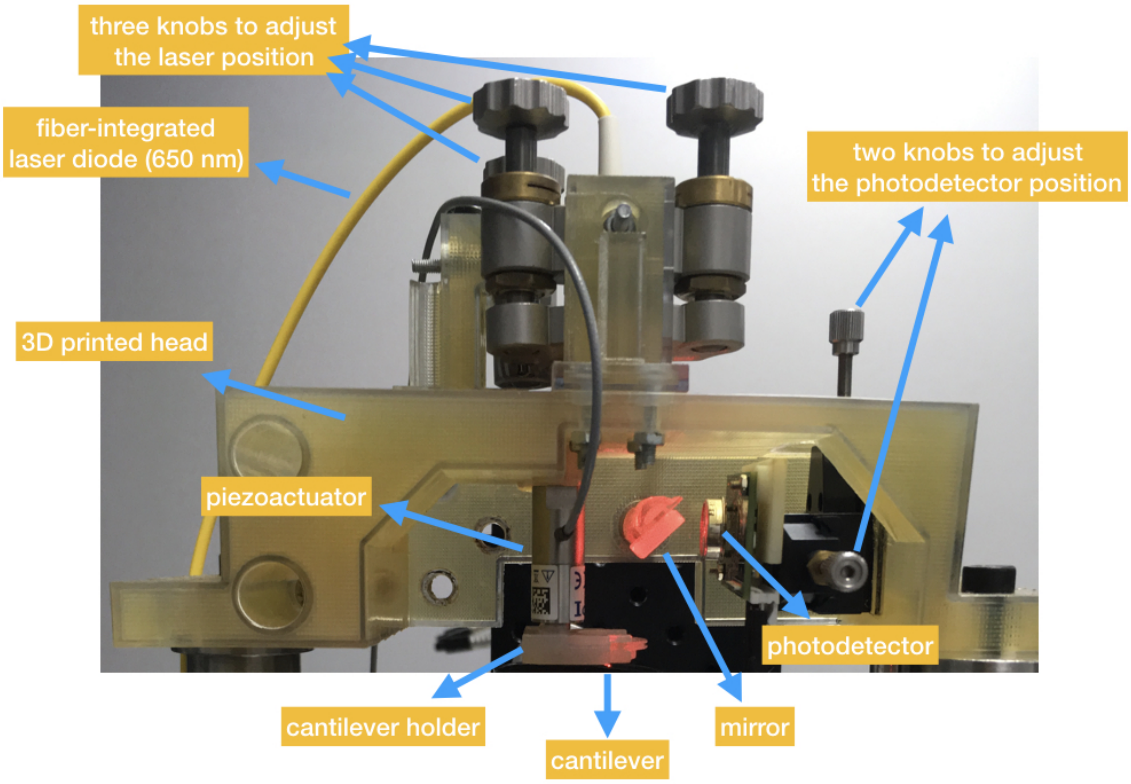


Figure 6.1. The photography of the AFM-head.

optical mount (Newport Corporation, CA, USA) to orient and focus the laser beam onto the cantilever. Here, the cantilever is mounted on the holder with the help of a custom-designed 3D-printed adapter that can be used both in air and liquid environment without sacrificing the laser alignment (some fine adjustments may be needed when the environment is changed). The reflected light from the cantilever surface is directed by a mirror (ValuMax Broadband Mirror, 12.7 mm Square, 488-694 nm) into a quadrant photodiode array (Pacific Silicon Sensor, CA, USA) which is mounted on a miniature two-axis translator (Thorlabs Inc. NJ, USA). The mirror has also a rotational degree of freedom with the help of a large actuator knob. Therefore, this custom-designed AFM-head provides multiple actuation capabilities by both the piezo actuator as a contact base-driven model and external acoustic-photoacoustic pressure waves as a non-contact driving model. The photography of the system is shown in Figure 6.1 in which the individual components are seen.

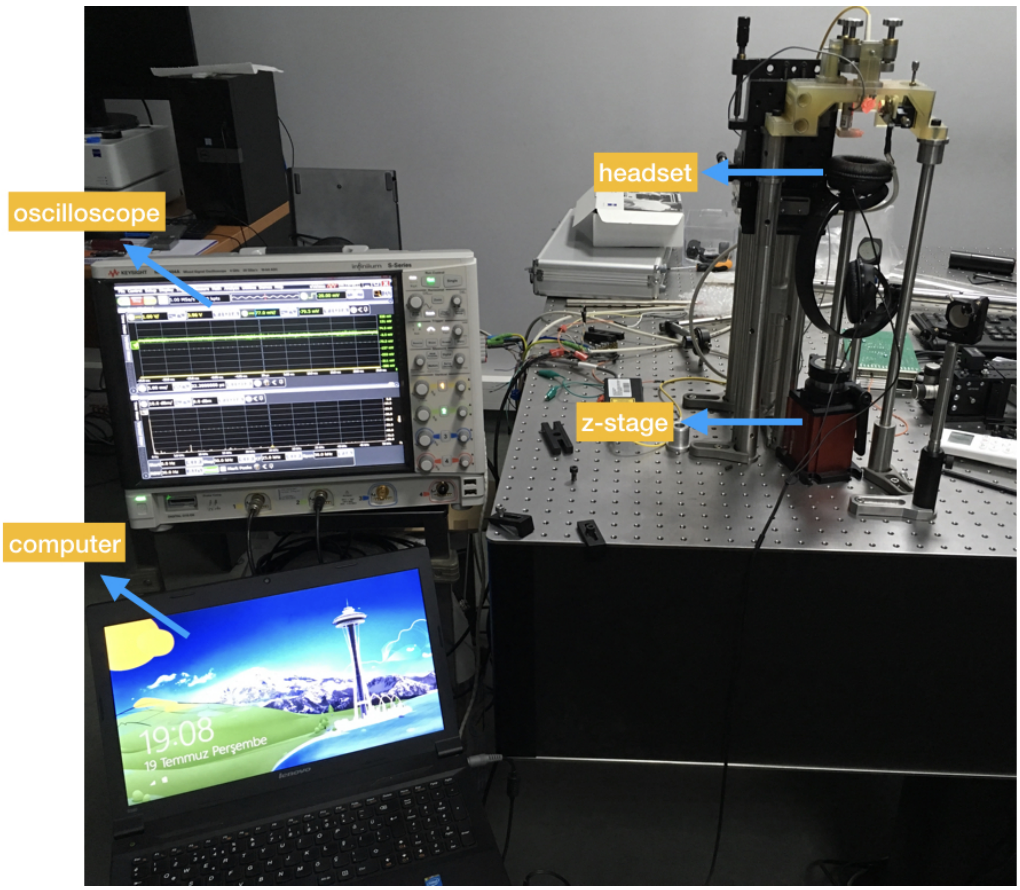


Figure 6.2. The photography of the AFM-head system for sound wave detection.

6.2. Sound Wave Detection Using the AFM-head System

In order to test the performance of our AFM-head as a pressure detector, we investigated the response of the microcantilever to the external sound waves. We used a personal headset as the sound source that was connected to a computer in which a self-written MATLAB code allows to adjust the frequency and the amplitude of the sound wave to a desired value. Here, we generated sinusoidal sound waves at various frequencies with the help of the code and sent these acoustic waves to microcantilevers via the headset which is located on an adjustable height stage to adjust its distance from the microcantilever. In the experiments, we used two separate microcantilevers with different resonant frequencies and geometric shapes; one is triangular (Bruker, SNL-10-D, ∼18 kHz, within a range of 12 to 24 kHz), other one is rectangular (Bruker, MLCT-B, ∼15 kHz, within a range of 10 to 20 kHz). The former has dimensions of 205 μm in length and 25 μm in width with a spring constant of 0.06 N/m, and the

latter has dimensions of 200 μm in length and 20 μm in width with a spring constant of 0.02 N/m. After the alignment procedure in which 650 nm laser light focused on the apex of the cantilever and the reflected light at the center of the photodiode, we monitored the oscillations of the microcantilevers on an oscilloscope from the output of the photodiode. The oscilloscope was connected to a computer for data acquisition. It should be noticed that we used the same computer for the data acquisition and the sound generation so that the synchronization was favorably realized between these two processes. The photography of the experimental setup is shown in Figure 6.2.

The response of the triangular microcantilever ($\sim$18 kHz) to the different acoustic frequencies is shown in Figure 6.3. The left column of the figure belongs to the time domain oscillations while the right column belongs to their FFT counterparts. Here, we used an oscilloscope (Keysight, InfiniiVision, DSOX3034T) to monitor the cantilever oscillation. We adjusted the z-distance as 3 cm which stands for the separation between the surface of the headset and the cantilever. We first monitored the random oscillations of the cantilever (Sound off) to observe the background noise of the system and the resonance curve of the cantilever in the absence of any external driving force. One can see in Figure 6.3g that the resonance curve of the cantilever appears around its resonant frequency value, as expected. This means that when we drive the cantilever with a frequency value within the resonance curve, the response will be relatively high to be the maximum at the value of the center of the curve. We also discovered the background noise at some certain frequency values probably due to the thermal drift in the system, the internal noise of the oscilloscope, and other ambient noise sources during the experiments. When the sound is on at 5 kHz, we can read this value in the FFT of the time domain oscillation which has not a distinct characteristic from the case of Sound off oscillation (Figure 6.3b and Figure 6.3h). Similar results appeared in the cases of Sound on at 15 kHz and 22 kHz (Figure 6.3c and Figure 6.3i, and Figure 6.3f and Figure 6.3l, respectively) that are the relatively close values to the resonance curve. Although the time domain oscillations seem to be like the oscillation in the case of Sound off, the FFTs provide the knowledge about the external sound source. It should be noted here that the response of the cantilever was supposed to be higher at 22 kHz, but the output performance of the headset decreases after 20 kHz. On the other

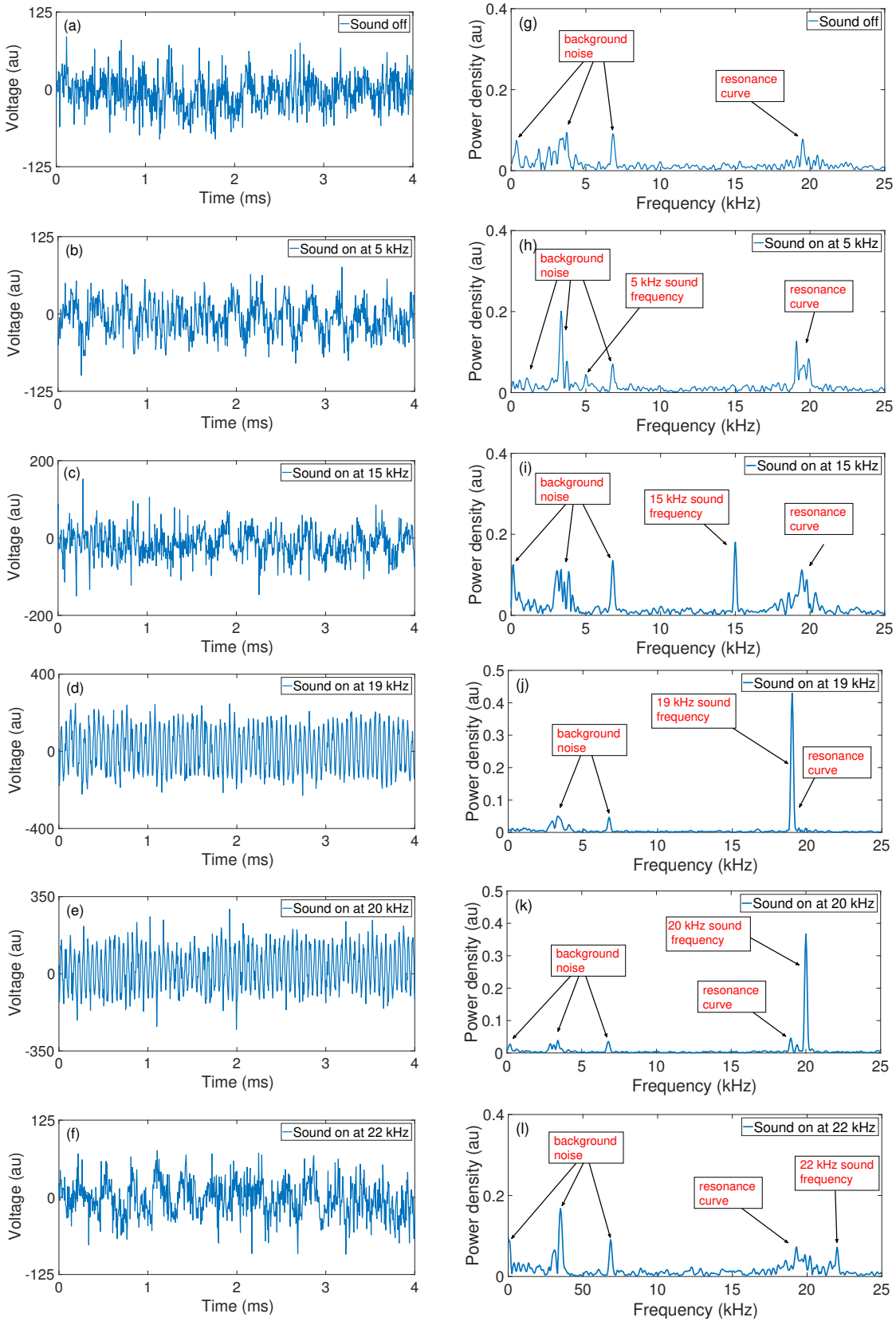


Figure 6.3. The responses of the microcantilever of ∼18 kHz to the various frequencies of sound waves arising from a headset. Maximum response occurs at 19 kHz.

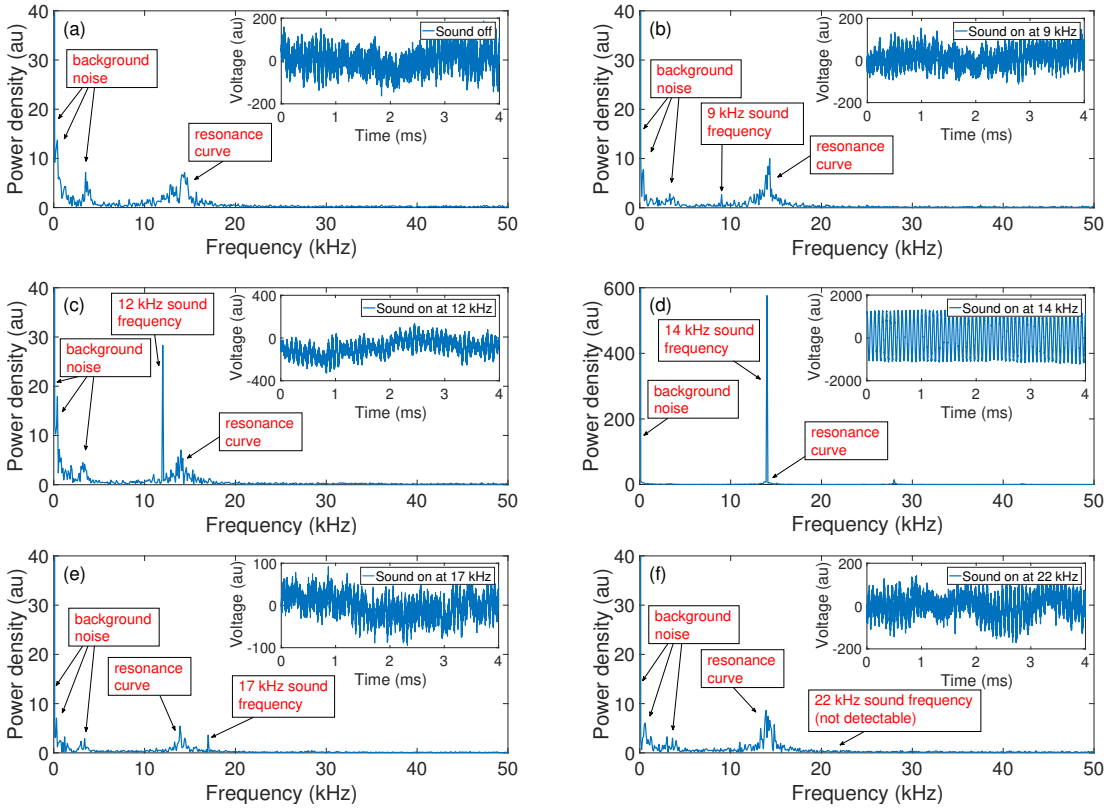


Figure 6.4. The responses of the microcantilever of ∼15 kHz to the various frequencies of sound waves arising from a headset. Maximum response occurs at 14 kHz.

hand, for the case of Sound on at 20 kHz (Figure 6.3e and Figure 6.3k) which is close to the resonance value, one can see the response of the microcantilever is higher in the manner of both the oscillation amplitude and the characteristic. Accordingly, the FFT of the oscillation yields the frequency value of the sound wave at a high power density compared to the background noise and the resonance curve. On the other hand, it can easily be seen that when the frequency of the sound wave corresponds to the resonant frequency of the microcantilever, the oscillation amplitude maximizes and becomes more steady-state. Furthermore, the corresponding FFT shows the clear maximum at 19 kHz by indicating the decrease in the density of the other frequency components including the background noise. Here, we note that the number of averaging was 4 for all measurements of the cantilever of 19 kHz.

Another experiment using the headset was conducted with the rectangular cantilever (∼15 kHz). The response of this cantilever to the external sinusoidal sound

waves was very similar to the case of ∼18 kHz cantilever. We excited the cantilever by sound waves of different frequencies. The response of the cantilever is shown in the set of the time domain oscillations and their FFT counterparts in Figure 6.4. In these experiments, we used a different oscilloscope (Keysight, MSOS404A) to monitor the oscillations. Figure 6.4a shows the random oscillations of the cantilever (Sound off) as the inset plot. Besides, the FFT of the random oscillations indicates the background noise of the system and the resonance curve, as expected. It should be noticed that the background noise has a different characteristic compared to the data recorded for the cantilever of ∼18 kHz. This is possibly due to using a different oscilloscope in this case and the environmental conditions. Furthermore, when the frequency of the sound wave is far from the resonant frequency of the cantilever, the resultant time domain oscillations do not provide reasonable knowledge about the external sound wave at first glance. In other words, the oscillations behave like random noise in the manner of amplitude and characteristic. However, when the sound frequency matches to the resonant frequency, the oscillation amplitude maximizes, and steady-state oscillations occur as shown in the inset plot of Figure 6.4d in which the FFT shows the clear maximum at the value of the sound frequency that is 14 kHz. We here note that the number of averaging was 32 for all measurements of the cantilever of ∼15 kHz. One can see the improvement in the stability of the time domain oscillations of ∼15 kHz cantilever compared to those of the ∼18 kHz cantilever due to the fact that the oscilloscope used for ∼15 kHz cantilever was the more advanced one, and the number of averaging was eight times higher.

As a result, our AFM-head system is well-capable of sensing the external sound waves. Over and above, more precise measurements can be obtained if we reduce the background noise and increase the number of averaging. On the other hand, in these experimental setups, we adjusted the z-distance between the headset and the microcantilever as 3 cm which is a relatively large distance. In smaller distances, we could obtain higher responses of the microcantilever.

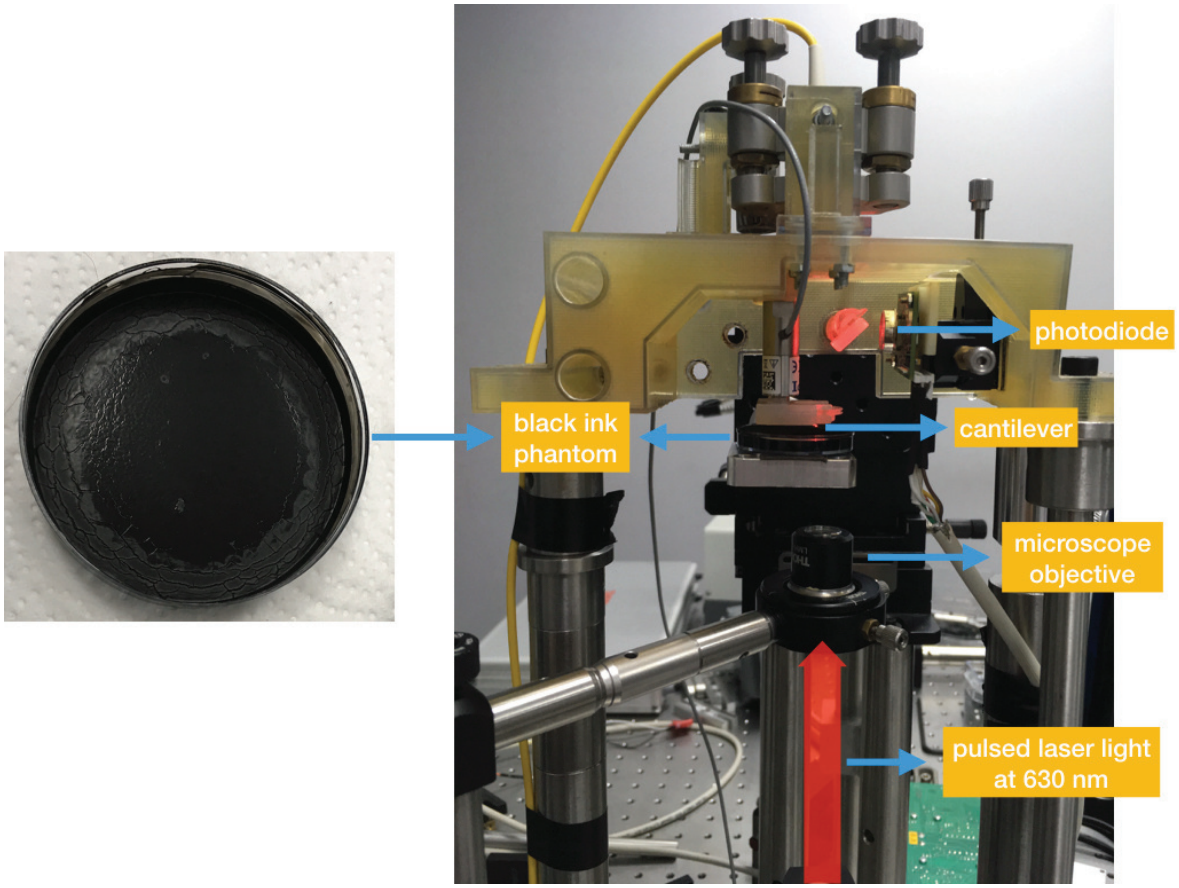


Figure 6.5. The black ink phantom used for photoacoustic generation in the AFM-head.

6.3. Photoacoustic Signal Detection Using the AFM-head System

In this section, apart from the acoustic detection mentioned in the previous part, we focused on photoacoustic detection using our AFM-head system in which the micro-cantilever was used as a pressure sensor. In this sense, we designed the experimental setup with the goal of photoacoustic generation using a sample and detection of the generated photoacoustic waves using a microcantilever. We conducted a series of experiments both in air and water medium for the proof-of-concept studies.

6.3.1. Sample Preparation

We prepared a black ink phantom inside a petri dish to be used for photoacoustic generation. First, the ink was injected into the petri dish via a needle to have an evenly

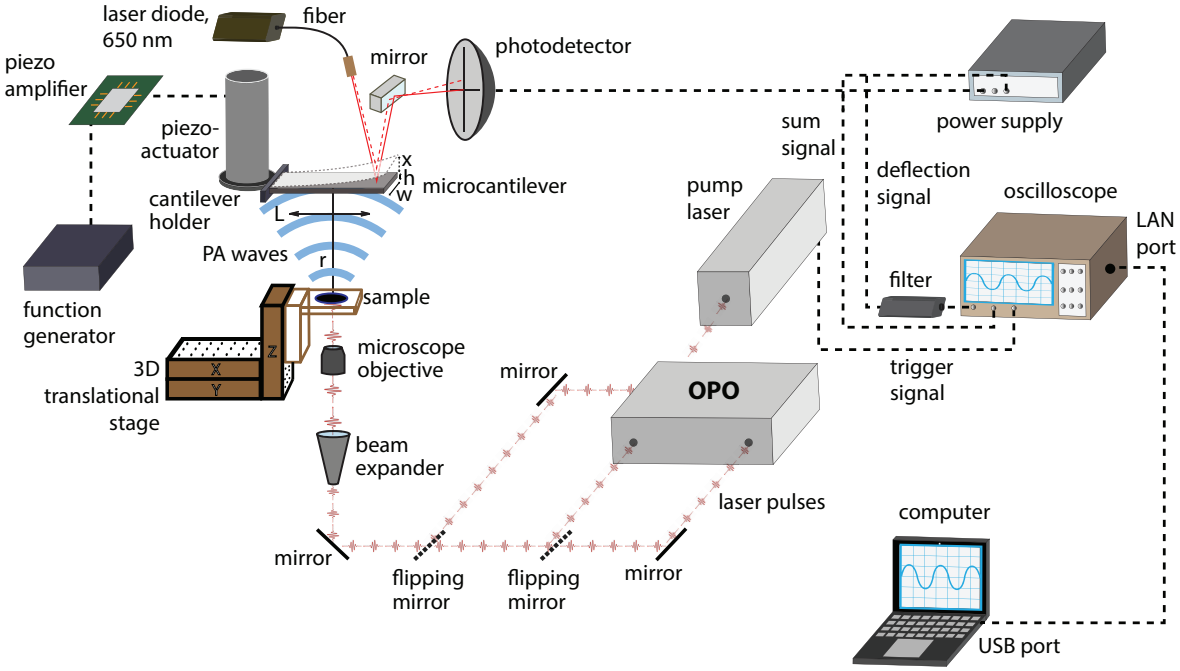


Figure 6.6. The schematic illustration of the experimental setup of photoacoustic signal detection by microcantilevers using our AFM-head system.

distributed fluid on the inner surface of the dish. We, then, waited for three days long in order for the liquid to achieve its solid state in order to avoid diffusion when we insert water into the petri dish. The photography of the sample is shown in Figure 6.5. It should be noticed that we used a spectrometer to ensure that the phantom is totally absorptive for the visible range. This was important to ensure that the deflection of the cantilever was only caused by the photoacoustic waves.

6.3.2. Experimental Setup

The photoacoustic generation unit in the experimental setup was initiated by the pulsed OPO laser mentioned in Chapter 1 which was placed on a vibration isolation table. We first aligned the pulsed laser light at 630 nm over the sample from its bottom through some optical components including mirrors, beam expander, a microscope objective (5x). The sample was located on a holder that was attached to a micrometer precision XYZ stage allowing to adjustment of the distance between the ink phantom and the cantilever. We used the rectangular cantilever (∼15 kHz) mentioned in the previous section. To monitor the oscillations, we used an oscilloscope (Keysight,

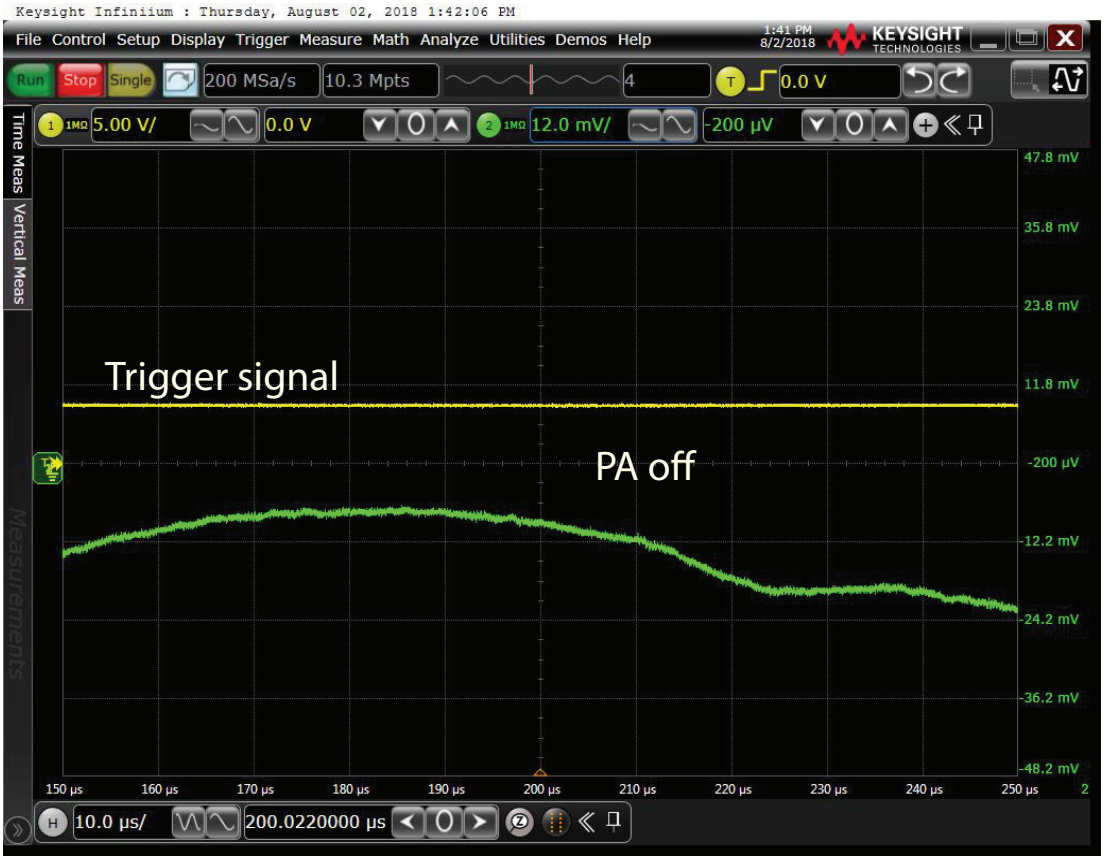


Figure 6.7. The screenshot image of the oscilloscope used for monitoring showing the values of the parameters, trigger signal, cantilever oscillation in the absence of photoacoustic waves (PA off).

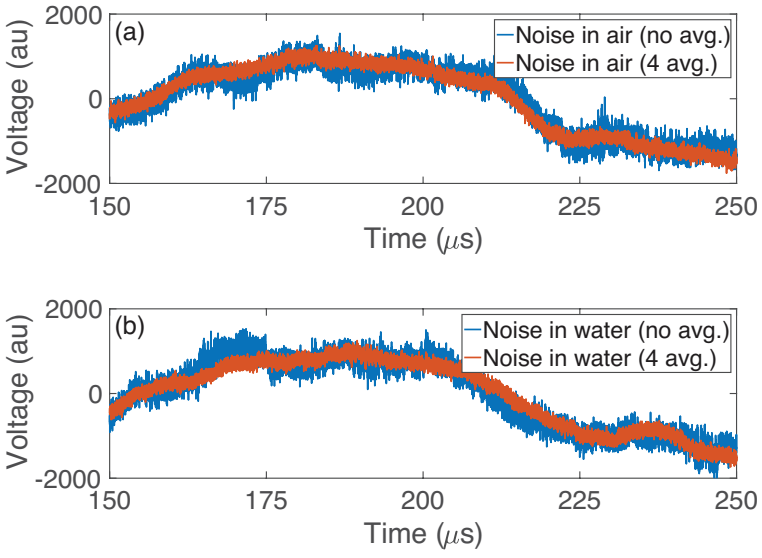


Figure 6.8. Random oscillations of the microcantilever (∼15 kHz) in (a) air and (b) water with no averaging and 4 averaging.

MSOS404A) triggered from the sync-out of the OPO laser for synchronization. The overall schematics of the experimental setup is shown in Figure 6.6. Figure 6.7 shows a screenshot of the oscilloscope indicating the trigger signal, random oscillation of the cantilever in the absence of photoacoustic waves (PA off) within the range of 150 μs and 250 μs, sampling rate (200 MSa/s), number of points for the record length of the data (10.3 Mpts).

Figure 6.8a and Figure 6.8b show the random oscillations of the microcantilever both in air and water medium by indicating the effect of taking average on the amplitude of the noise. Furthermore, here we see that the noise characteristics of the microcantilever are very similar for the air and water medium. In fact, the amplitude of the random oscillations is supposed to be lower in water compared to the amplitude in the air due to the damping effect. However, it seems that other noise sources in the system are dominant over the noise of the cantilever.

6.3.3. Air-coupled Photoacoustic Detection

We first conducted photoacoustic measurements of the ink phantom for air-coupled detection in which the generated photoacoustic waves from the ink reach the cantilever surface passing through the air medium. It should be noted here that the acoustic impedance mismatch between the solid ink and the air medium will cause the generated photoacoustic signal inside the ink to lose its power in the air due to reflection and scattering on the boundary. However, the response of the cantilever in air will be higher compared to the those in water because the damping rate in the air is lower compared to that of in water.

Figure 6.9 shows the set of the photoacoustic signals detected by the microcantilever in our AFM-head system with respect to varying z-distance which stands for the separation between the ink surface and the cantilever. The amplitude of the photoacoustic signal decreases with the increasing z-distance. This is in accordance with the fact that the photoacoustic wave loses its power with increasing distance mentioned in Section 1. In these measurements, the pulse energy of the laser was adjusted to 1 μJ

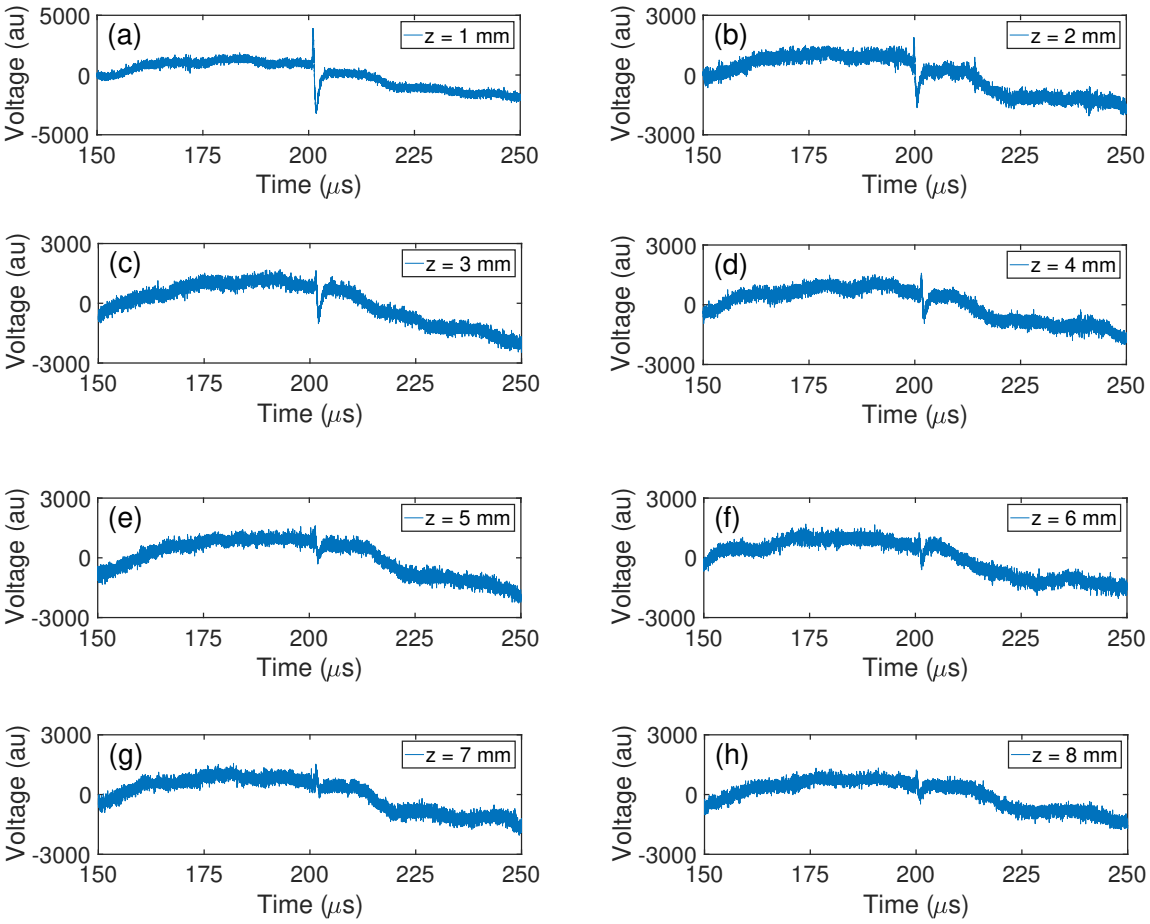


Figure 6.9. Photoacoustic signals arising from black ink phantom detected in air medium by using the AFM-head. Here, the z-parameter stands for the distance between the ink surface and the microcantilever (14 kHz in air), and the pulse energy is 1 μJ at 630 nm.

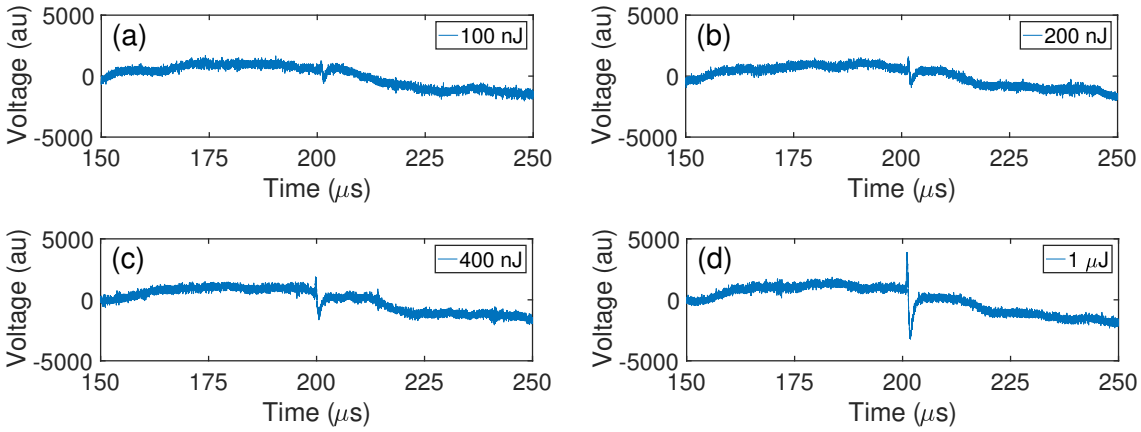


Figure 6.10. Photoacoustic signals arising from black ink phantom detected by a microcantilever (14 kHz in air) in air medium by using the AFM-head at pulse energies of (a) 100 nJ, (b) 200 nJ, (c) 400 nJ, and (d) 1 μJ at 630 nm. The distance between the ink surface and the microcantilever was adjusted as 1 mm.

at the wavelength of 630 nm.

On the other hand, we also investigated the response of the microcantilever to the laser-induced photoacoustic waves arising from the ink phantom generated by various pulse energy values. The results of these measurements including pulse energies of 100 nJ, 200 nJ, 400 nJ, and 1 μJ are shown in Figure 6.10. Here we observe that the increase in the pulse energy leads to an increase in the response of the cantilever in the manner of amplitude. This is what we expect according to the definition of the initial photoacoustic pressure which is proportional to the pulse energy of the excitation laser (see Equation 2.8).

6.3.4. Water-coupled Photoacoustic Detection

In this section, we placed the ink phantom and the cantilever in water to perform the water-coupled photoacoustic detection. We again used the cantilever of ~15 kHz for the detection. Similarly to the air-coupled detection, we took the measurements of the generated photoacoustic signals for the different z-distance indicating the separation between the ink surface and the cantilever. Figure 6.11 shows the set of the detected

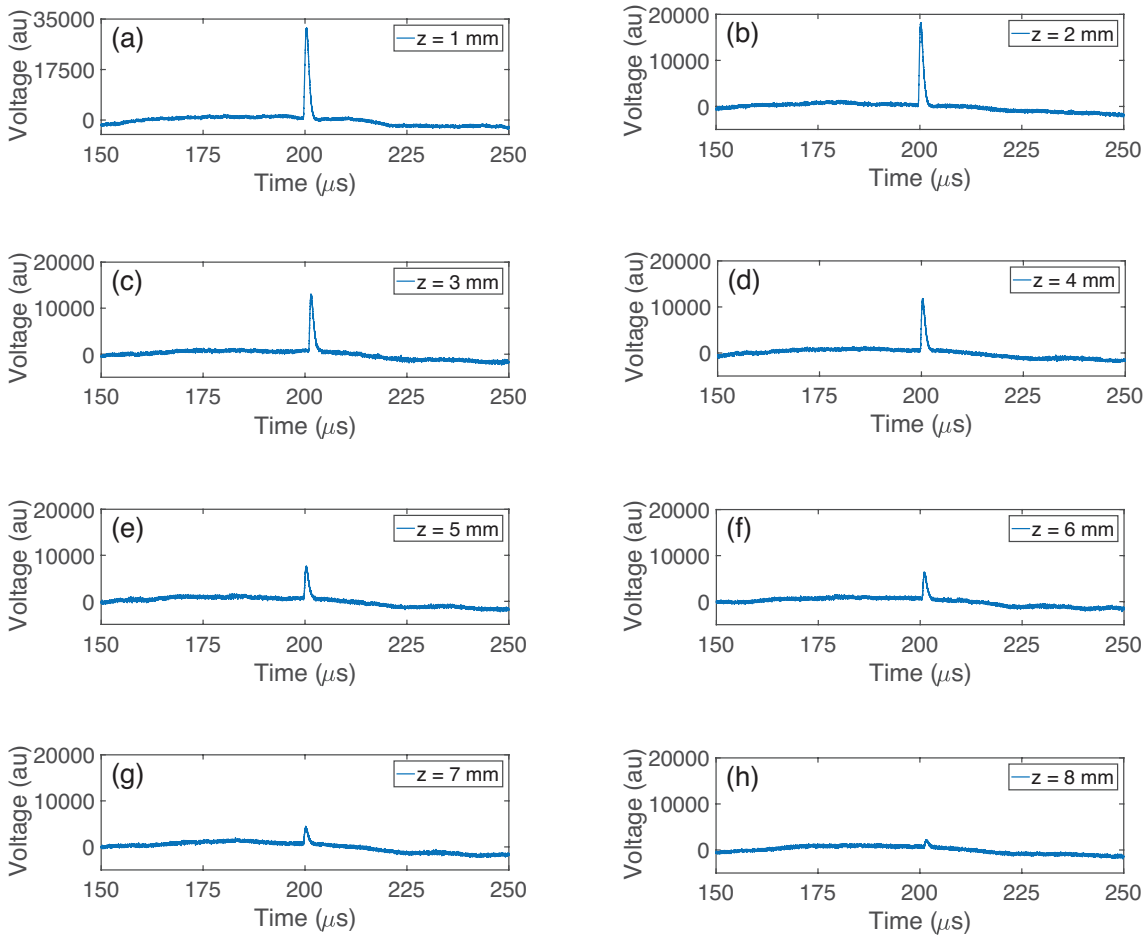


Figure 6.11. Photoacoustic signals arising from black ink phantom detected in water medium by using the AFM-head. Here, the z-parameter stands for the distance between the ink surface and the microcantilever (∼6 kHz in water), and the pulse energy is 1 μJ at 630 nm.

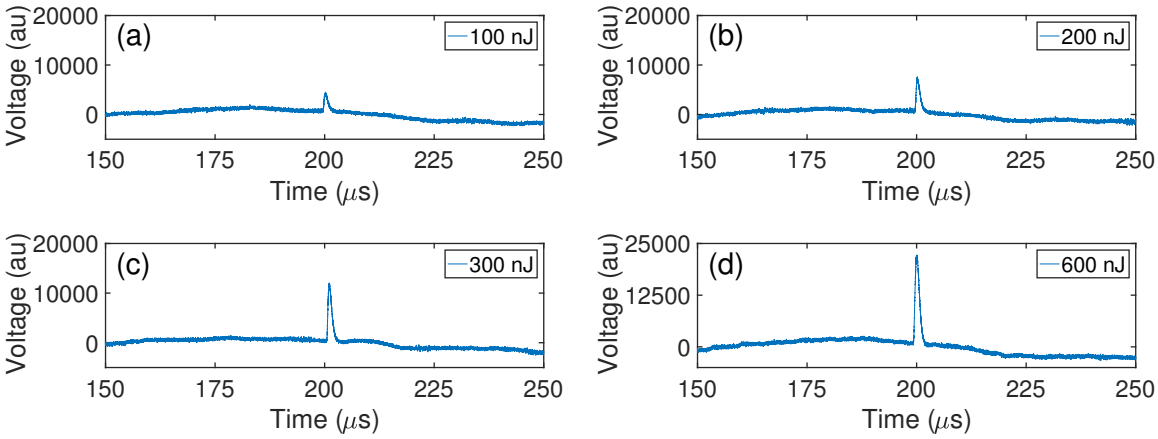


Figure 6.12. Photoacoustic signals arising from black ink phantom detected in water by a microcantilever (∼6 kHz in water) using the AFM-head at pulse energies of (a) 100 nJ, (b) 200 nJ, (c) 400 nJ, and (d) 600 nJ at 630 nm. The distance between the ink surface and the microcantilever was adjusted as 1 mm.

photoacoustic signals in water arising from the same ink phantom. Again, we used the OPO laser for the photoacoustic excitation. As expected, the amplitude of the photoacoustic signal decreases while z-distance increases. In these measurements, the pulse energy of the laser was again adjusted to the value of 1 μJ which is the same value in the air-coupled detection.

Here, we also conducted some photoacoustic measurements for varying pulse energies in water-coupled detection. The results of these measurements including pulse energies of 100 nJ, 200 nJ, 400 nJ, and 600 nJ are shown in Figure 6.10.

6.4. Discussion

We have successfully developed a custom-designed atomic force microscopy head system which is very compact, stable, portable, relatively cheap, sensitive, and also provides acoustic and photoacoustic detection both in air and water medium. The signal-to-noise ratios of the photoacoustic signals obtained with our AFM-head system using cantilevers are very high, particularly when compared to those of ultrasonic piezoelectric transducers in Chapter 4. Particularly, when we take the air-coupled ultrasonic detection methods into consideration that are usually performed by using

air-coupled transducers, acoustic impedance mismatch between sample and air causes attenuation of ultrasonic waves at the boundary which makes the detection very difficult. To compensate this effect, higher pulse energies should be applied to sample in order to generate photoacoustic waves with high initial pressures so that the signals may become detectable with these detectors. However, microcantilevers are very sensitive in air because the damping ratio is very low in air medium. Therefore, even small photoacoustic pressures can apply forces that yield cantilever deflections at the measurable levels for photodetectors. On the other hand, this condition is reversed in water medium. Although the damping ratio for microcantilevers is very high in water, acoustic impedance values of samples are closer to that of water compared to the air. Thus, the attenuation of the ultrasonic waves at the boundary is not so high and much more acoustic pressure arising from the sample reaches to cantilever surface yielding relatively large deflections. For our measurements, when we compare the detected signals both in air and water medium for the same source-detector distances and pulse energy values, we observe that the signal to noise ratios in water are higher than those in air (see Figure 6.9 and Figure 6.11, and Figure 6.10 and Figure 6.12). Besides, the high damping effect onto the microcantilever surface in water can easily be recognized in these figures so that the shapes of the detected signals are different in air and water.

7. CONCLUSION

We have presented an all-fiber-based pulsed laser developed particularly for OR-PAM, in which the laser has unique properties such as having adjustable pulse repetition frequency between 65 kHz-1 MHz, pulse duration between 5-10 ns, pulse energy up to 10 μJ, and wavelength tunability between 450-1100 nm by its supercontinuum output, and 532 nm, 355 nm, 266 nm from its harmonic generation unit obtained by a separate output of 1064 nm. When we compare this laser to all-fiber-based laser systems, the developed system enhances the wavelength tunability with a pulse repetition frequency up to 1 MHz which is very important to decrease data acquisition time in PAM. It should be noted here that it is very challenging to have high pulse energies for laser systems having fiber components due to relatively low damage thresholds of fibers. For all that, pulse energy values of our fiber laser are higher than PCF-coupled supercontinuum cases and comparable to the output values of a specially designed fiber laser with tapered PCF mentioned in Section 3.2. Here, pulse energy values obtained with SRS peaks can be surpassed within the near-infrared region with the same bandwidth, but in the visible region by utilizing filters having wider bandwidths. Additionally, our fiber laser providing all-fiber integrity and high PRF with the help of FPGA is very compact, portable, relatively cheap, and do not require external cooling unit as in OPO laser. It is also mostly immune to mechanical and thermal perturbations as well as being misalignment free. All in all, our fiber laser having maximum flexibility on its parameters may pave the way for spectroscopic PAM applications via widely tunable fiber laser technologies.

Besides, we have built a custom designed PAM system in which either the fiber laser as mentioned earlier or the OPO laser were able to be used as the photoacoustic excitation source. To achieve this, we have co-aligned the outputs of these two lasers in a same optical path so that any of them might be made passive utilizing a flipping mirror when desired. In this PAM system, we used ultrasonic piezoelectric transducers as the photoacoustic detection sensor, and the system was able to change the detector according to sample to be detected. As a preliminary study, we have concentrated

on the generation of photoacoustic signals from various samples such as black ink phantom and horse tail-hair. After completing this phase, we have worked on image reconstruction using the generated signals by scanning the sample. Using MAP, we have obtained the photoacoustic images of the samples. Afterward, we have used a resolution test target to determine the resolution of our PAM system and achieved a lateral resolution of 2.68 μm. This value is good enough to image a single cell when the sizes of cells are taken into consideration (e.g., the size of an RBC is around 8 μm in diameter). Furthermore, we have demonstrated the multispectral property of our PAM system by imaging the test target with various wavelengths. Moreover, we have imaged RBCs, and various cells within a PDMS phantom using both the OPO laser and the fiber laser as the excitation source. All these results indicate the feasibility of the developed system for diagnostic classification of cells.

On the other hand, under the objective of this thesis, we have done analyses of microcantilevers that are excited by photoacoustic waves. This study was essential before building an AFM-head system utilizing microcantilevers as the photoacoustic sensor. Apart from photoacoustic detection, an analysis of microcantilever excitation by photoacoustic waves particularly for AFM actuation was another objective of this study. Thus, we have designed and coded a model to investigate the effects of consecutive photoacoustic waves, arising from a spherical light absorber illuminated by short laser pulses. So, we have examined the cumulative effects of the consecutive photoacoustic waves on the oscillation of microcantilever by taking the pulse repetition frequency of the laser into account. With this connection, we have analyzed the oscillation characteristics of two rectangular microcantilevers with different resonant frequencies. Here, our study shows that photoacoustic waves can provide steady-state oscillations of microcantilevers particularly when the pulse repetition frequency matches to the fundamental resonant frequency of microcantilever or its lower harmonics. Some of the issues emerging from these findings may find application area in atomic force microscopy actuation and photoacoustic signal detection.

We have presented a custom-designed AFM-head which aims at detection of both acoustic and photoacoustic signals. This system is portable, compact, relatively cheap, and also very sensitive when compared to the traditional detection tools mentioned in Introduction. Furthermore, a detection system which allows measuring acoustic and photoacoustic waves both in air and water is always preferable since the conventional tools are generally produced for only air-coupled detection or water-coupled detection. For example, ultrasonic piezoelectric transducers that are the most commonly used for photoacoustic detection are produced either for measurements in the air called air-coupled transducer or in water called water immersion transducer. However, we have performed acoustic and photoacoustic detection in both media with our AFM-head system using cantilevers as pressure sensors. This work in which we have aimed at photoacoustic signal detection can be used to create photoacoustic images of samples by 2D raster scanning as in traditional methods which we have presented various results in Chapter 4. This objective of the AFM-head system requires an appropriate experimental setup, an accurate signal analysis, and image reconstruction procedures so that it was left as future work.

REFERENCES

1. Bell, A. G., "Upon the Production and Reproduction of Sound by Light", *Journal of the Society of Telegraph Engineers*, Vol. 9, No. 34, pp. 404–426, 1880.

2. Fan, Y., A. Mandelis, G. Spirou and I. Alex Vitkin, "Development of a Laser Photothermoacoustic Frequency-Swept System for Subsurface Imaging: Theory and Experiment", *The Journal of the Acoustical Society of America*, Vol. 116, No. 6, pp. 3523–3533, 2004.

3. Maslov, K. I. and L. V. Wang, "Photoacoustic Imaging of Biological Tissue with Intensity-Modulated Continuous-Wave Laser", *Journal of Biomedical Optics*, Vol. 13, No. 2, p. 024006, 2008.

4. Lashkari, B. and A. Mandelis, "Photoacoustic Radar Imaging Signal-to-Noise Ratio, Contrast, and Resolution Enhancement Using Nonlinear Chirp Modulation", *Optics Letters*, Vol. 35, No. 10, pp. 1623–1625, 2010.

5. Wang, L. V. and H.-I. Wu, *Biomedical optics: principles and imaging*, John Wiley & Sons, 2012.

6. Aytac-Kipergil, E., A. Demirkiran, N. Uluc, S. Yavas, T. Kayikcioglu, S. Salman, S. G. Karamuk, F. O. Ilday and M. B. Unlu, "Development of a Fiber Laser with Independently Adjustable Properties for Optical Resolution Photoacoustic Microscopy", *Scientific Reports*, Vol. 6, p. 38674, 2016.

7. Tam, A. C., "Applications of Photoacoustic Sensing Techniques", *Reviews of Modern Physics*, Vol. 58, No. 2, p. 381, 1986.

8. Petschke, A. and P. J. La Rivière, "Comparison of Intensity-Modulated Continuous-Wave Lasers with a Chirped Modulation Frequency to Pulsed Lasers for Photoacoustic Imaging Applications", *Biomedical Optics Express*, Vol. 1,

No. 4, pp. 1188–1195, 2010.

9. Yao, J. and L. V. Wang, "Sensitivity of Photoacoustic Microscopy", *Photoacoustics*, Vol. 2, No. 2, pp. 87–101, 2014.

10. Wang, L. V. and S. Hu, "Photoacoustic Tomography: In vivo Imaging from Organelles to Organs", *Science*, Vol. 335, No. 6075, pp. 1458–1462, 2012.

11. Zhang, C., K. Maslov and L. V. Wang, "Subwavelength-resolution label-free photoacoustic microscopy of optical absorption in vivo", *Optics Letters*, Vol. 35, No. 19, pp. 3195–3197, 2010.

12. Hu, S., K. Maslov and L. V. Wang, "Second-Generation Optical-Resolution Photoacoustic Microscopy with Improved Sensitivity and Speed", *Optics Letters*, Vol. 36, No. 7, pp. 1134–1136, 2011.

13. Song, L., K. Maslov and L. V. Wang, "Multifocal Optical-Resolution Photoacoustic Microscopy In Vivo", *Optics Letters*, Vol. 36, No. 7, pp. 1236–1238, 2011.

14. Hu, S. and L. V. Wang, "Optical-Resolution Photoacoustic Microscopy: Auscultation of Biological Systems at the Cellular Level", *Biophysical Journal*, Vol. 105, No. 4, pp. 841–847, 2013.

15. Ma, R., A. Taruttis, V. Ntziachristos and D. Razansky, "Multispectral Optoacoustic Tomography (MSOT) Scanner for Whole-body Small Animal Imaging", *Optics Express*, Vol. 17, No. 24, pp. 21414–21426, 2009.

16. Li, L., L. Zhu, C. Ma, L. Lin, J. Yao, L. Wang, K. Maslov, R. Zhang, W. Chen, J. Shi *et al.*, "Single-Impulse Panoramic Photoacoustic Computed Tomography of Small-animal Whole-body Dynamics at High Spatiotemporal Resolution", *Nature Biomedical Engineering*, Vol. 1, No. 5, p. 0071, 2017.

17. Nasiriavanaki, M., J. Xia, H. Wan, A. Q. Bauer, J. P. Culver and L. V. Wang,

"High-Resolution Photoacoustic Tomography of Resting-State Functional Connectivity in the Mouse Brain", *Proceedings of the National Academy of Sciences*, Vol. 111, No. 1, pp. 21–26, 2014.

18. Yao, J., L. Wang, J.-M. Yang, K. I. Maslov, T. T. Wong, L. Li, C.-H. Huang, J. Zou and L. V. Wang, "High-Speed Label-Free Functional Photoacoustic Microscopy of Mouse Brain in Action", *Nature Methods*, Vol. 12, No. 5, p. 407, 2015.

19. Wang, L. V., "Tutorial on Photoacoustic Microscopy and Computed Tomography", *IEEE Journal of Selected Topics in Quantum Electronics*, Vol. 14, No. 1, pp. 171–179, 2008.

20. Kruger, R. A., P. Liu, Y. R. Fang and C. R. Appledorn, "Photoacoustic Ultrasound (PAUS)-Reconstruction Tomography", *Medical Physics*, Vol. 22, No. 10, pp. 1605–1609, 1995.

21. Zhang, H. F., K. Maslov and L. V. Wang, "In Vivo Imaging of Subcutaneous Structures Using Functional Photoacoustic Microscopy", *Nature Protocols*, Vol. 2, No. 4, p. 797, 2007.

22. Allen, T. J. and P. C. Beard, "Pulsed Near-Infrared Laser Diode Excitation System for Biomedical Photoacoustic Imaging", *Optics Letters*, Vol. 31, No. 23, pp. 3462–3464, 2006.

23. Ku, G. and L. V. Wang, "Deeply Penetrating Photoacoustic Tomography in Biological Tissues Enhanced with an Optical Contrast Agent", *Optics Letters*, Vol. 30, No. 5, pp. 507–509, 2005.

24. Kim, C., T. N. Erpelding, L. Jankovic, M. D. Pashley and L. V. Wang, "Deeply Penetrating In Vivo Photoacoustic Imaging Using a Clinical Ultrasound Array System", *Biomedical Optics Express*, Vol. 1, No. 1, pp. 278–284, 2010.

25. Niederhauser, J. J., M. Jaeger, R. Lemor, P. Weber and M. Frenz, "Combined Ultrasound and Optoacoustic System for Real-time High-contrast Vascular Imaging In Vivo", *IEEE Transactions on Medical Imaging*, Vol. 24, No. 4, pp. 436–440, 2005.

26. Fronheiser, M. P., S. A. Ermilov, H.-P. F. Brecht, A. Conjusteau, R. Su, K. Mehta and A. A. Oraevsky, "Real-time Optoacoustic Monitoring and Three-dimensional Mapping of a Human Arm Vasculature", *Journal of Biomedical Optics*, Vol. 15, No. 2, p. 021305, 2010.

27. Wang, L. V., "Multiscale Photoacoustic Microscopy and Computed Tomography", *Nature Photonics*, Vol. 3, No. 9, p. 503, 2009.

28. Beard, P., "Biomedical Photoacoustic Imaging", *Interface Focus*, p. rsfs20110028, 2011.

29. Zhang, E. and P. Beard, "Broadband Ultrasound Field Mapping System Using a Wavelength Tuned, Optically Scanned Focused Laser Beam to Address a Fabry Perot Polymer Film Sensor", *IEEE Transactions on Ultrasonics, Ferroelectrics, and Frequency Control*, Vol. 53, No. 7, pp. 1330–1338, 2006.

30. Beard, P., F. Perennes, E. Draguioti and T. Mills, "Optical Fiber Photoacoustic–Photothermal Probe", *Optics Letters*, Vol. 23, No. 15, pp. 1235–1237, 1998.

31. Hamilton, J. D., T. Buma, M. Spisar and M. O'Donnell, "High Frequency Optoacoustic Arrays Using Etalon Detection", *IEEE Transactions on Ultrasonics, Ferroelectrics, and Frequency Control*, Vol. 47, No. 1, pp. 160–169, 2000.

32. Preisser, S., W. Rohringer, M. Liu, C. Kollmann, S. Zotter, B. Fischer and W. Drexler, "All-optical Highly Sensitive Akinetic Sensor for Ultrasound Detection and Photoacoustic Imaging", *Biomedical Optics Express*, Vol. 7, No. 10, pp. 4171–4186, 2016.

33. Zhang, C., S.-L. Chen, T. Ling and L. J. Guo, "Review of Imprinted Polymer Microrings as Ultrasound Detectors: Design, Fabrication, and Characterization", *IEEE Sensors Journal*, Vol. 15, No. 6, pp. 3241–3248, 2015.

34. Li, H., B. Dong, Z. Zhang, H. F. Zhang and C. Sun, "A Transparent Broadband Ultrasonic Detector Based on an Optical Micro-ring Resonator for Photoacoustic Microscopy", *Scientific Reports*, Vol. 4, p. 4496, 2014.

35. Ashkenazi, S., C.-Y. Chao, L. J. Guo and M. O'donnell, "Ultrasound Detection Using Polymer Microring Optical Resonator", *Applied Physics Letters*, Vol. 85, No. 22, pp. 5418–5420, 2004.

36. Ling, T., S.-L. Chen and L. J. Guo, "Fabrication and Characterization of High Q Polymer Micro-ring Resonator and Its Application as a Sensitive Ultrasonic Detector", *Optics express*, Vol. 19, No. 2, pp. 861–869, 2011.

37. Leinders, S., W. Westerveld, J. Pozo, P. Van Neer, B. Snyder, P. O'Brien, H. Urbach, N. de Jong and M. D. Verweij, "A Sensitive Optical Micro-machined Ultrasound Sensor (OMUS) Based on a Silicon Photonic Ring Resonator on an Acoustical Membrane", *Scientific Reports*, Vol. 5, p. 14328, 2015.

38. De Brabander, G. N., J. T. Boyd and G. Beheim, "Integrated Optical Ring Resonator with Micromechanical Diaphragms for Pressure Sensing", *IEEE Photonics technology letters*, Vol. 6, No. 5, pp. 671–673, 1994.

39. Monifi, F., B. Peng, S. K. Ozdemir, L. Ma, K. Maslov, L. Wang and L. Yang, "Ultrasound Sensing Using a Fiber Coupled Silica Microtoroid Resonator Encapsulated in a Polymer", *Photonics Conference (IPC), 2013 IEEE*, pp. 215–216, IEEE, 2013.

40. Chistiakova, M. V. and A. M. Armani, "Photoelastic Ultrasound Detection Using Ultra-high-Q Silica Optical Resonators", *Optics Express*, Vol. 22, No. 23, pp. 28169–28179, 2014.

41. Zeng, L., G. Liu, D. Yang and X. Ji, "3D-visual Laser-diode-based Photoacoustic Imaging", *Optics Express*, Vol. 20, No. 2, pp. 1237–1246, 2012.

42. Zeng, L., G. Liu, D. Yang and X. Ji, "Portable Optical-Resolution Photoacoustic Microscopy with a Pulsed Laser Diode Excitation", *Applied Physics Letters*, Vol. 102, No. 5, p. 053704, 2013.

43. Zeng, L., G. Liu, D. Yang and X. Ji, "Cost-Ffficient Laser-Diode-Induced Optical-resolution Photoacoustic Microscopy for Two-Dimensional/Three-Dimensional Biomedical Imaging", *Journal of Biomedical Optics*, Vol. 19, No. 7, p. 076017, 2014.

44. Wang, T., S. Nandy, H. S. Salehi, P. D. Kumavor and Q. Zhu, "A Low-cost Photoacoustic Microscopy System with a Laser Diode Excitation", *Biomedical Optics Express*, Vol. 5, No. 9, pp. 3053–3058, 2014.

45. Kolkman, R. G., W. Steenbergen and T. G. van Leeuwen, "In Vivo Photoacoustic Imaging of Blood Vessels with a Pulsed Laser Diode", *Lasers in Medical Science*, Vol. 21, No. 3, pp. 134–139, 2006.

46. Zeng, L., Z. Piao, S. Huang, W. Jia and Z. Chen, "Label-free Optical-resolution Photoacoustic Microscopy of Superficial Microvasculature Using a Compact Visible Laser Diode Excitation", *Optics Express*, Vol. 23, No. 24, pp. 31026–31033, 2015.

47. Maslov, K., G. Stoica and L. V. Wang, "In Vivo Dark-Field Reflection-Mode Photoacoustic Microscopy", *Optics Letters*, Vol. 30, No. 6, pp. 625–627, 2005.

48. Zhang, H. F., K. Maslov, G. Stoica and L. V. Wang, "Functional Photoacoustic Microscopy for High-Resolution and Noninvasive In Vivo Imaging", *Nature Biotechnology*, Vol. 24, No. 7, p. 848, 2006.

49. Maslov, K., H. F. Zhang, S. Hu and L. V. Wang, "Optical-Resolution Photoacous-

tic Microscopy for In Vivo Imaging of Single Capillaries", *Optics Letters*, Vol. 33, No. 9, pp. 929–931, 2008.

50. Favazza, C. P., L. V. Wang, O. W. Jassim and L. A. Cornelius, "In Vivo Photoacoustic Microscopy of Human Cutaneous Microvasculature and a Nevus", *Journal of Biomedical Optics*, Vol. 16, No. 1, p. 016015, 2011.

51. Li, L., R. J. Zemp, G. F. Lungu, G. Stoica and L. V. Wang, "Photoacoustic Imaging of lacZ Gene Expression In Vivo", *Journal of Biomedical Optics*, Vol. 12, No. 2, p. 020504, 2007.

52. Krumholz, A., J. Yao, L. V. Wang, T. Fleming, W. E. Gillanders *et al.*, "Photoacoustic Microscopy of Tyrosinase Reporter Gene In Vivo", *Journal of Biomedical Optics*, Vol. 16, No. 8, p. 080503, 2011.

53. Wang, T., Y. Yang, U. Alqasemi, P. D. Kumavor, X. Wang, M. Sanders, M. Brewer and Q. Zhu, "Characterization of Ovarian Tissue Based on Quantitative Analysis of Photoacoustic Microscopy Images", *Biomedical Optics Express*, Vol. 4, No. 12, pp. 2763–2768, 2013.

54. Song, K. and L. V. Wang, "Deep Reflection-Mode Photoacoustic Imaging of Biological Tissue", *Journal of Biomedical Optics*, Vol. 12, No. 6, p. 060503, 2007.

55. Song, K. H., C. Kim, K. Maslov and L. V. Wang, "Noninvasive In Vivo Spectroscopic Nanorod-Contrast Photoacoustic Mapping of Sentinel Lymph Nodes", *European Journal of Radiology*, Vol. 70, No. 2, pp. 227–231, 2009.

56. Yao, D.-K., K. I. Maslov, L. V. Wang, R. Chen and Q. Zhou, "Optimal Ultraviolet Wavelength for In Vivo Photoacoustic Imaging of Cell Nuclei", *Journal of Biomedical Optics*, Vol. 17, No. 5, p. 056004, 2012.

57. Li, C., A. Aguirre, J. K. Gamelin, A. Maurudis, Q. Zhu and L. V. Wang, "Real-Time Photoacoustic Tomography of Cortical Hemodynamics in Small Animals",

Journal of Biomedical Optics, Vol. 15, No. 1, p. 010509, 2010.

58. Ai, M., W. Shu, T. Salcudean, R. Rohling, P. Abolmaesumi and S. Tang, "High Energy Laser Pulse Coupling in a Multimode Fiber For Photoacoustic Tomography", *Photons Plus Ultrasound: Imaging and Sensing 2016*, Vol. 9708, p. 97084H, International Society for Optics and Photonics, 2016.

59. Cao, R., J. P. Kilroy, B. Ning, T. Wang, J. A. Hossack and S. Hu, "Multispectral Photoacoustic Microscopy Based on an Optical–Acoustic Objective", *Photoacoustics*, Vol. 3, No. 2, pp. 55–59, 2015.

60. Zhang, C., K. I. Maslov, J. Yao and L. V. Wang, "In Vivo Photoacoustic Microscopy with 7.6-μm Axial Resolution Using a Commercial 125-MHz Ultrasonic Transducer", *Journal of Biomedical Optics*, Vol. 17, No. 11, p. 116016, 2012.

61. Billeh, Y. N., M. Liu and T. Buma, "Spectroscopic Photoacoustic Microscopy Using a Photonic Crystal Fiber Supercontinuum Source", *Optics Express*, Vol. 18, No. 18, pp. 18519–18524, 2010.

62. Lee, C., S. Han, S. Kim, M. Jeon, M. Y. Jeon, C. Kim and J. Kim, "Combined Photoacoustic and Optical Coherence Tomography Using a Single Near-Infrared Supercontinuum Laser Source", *Applied Optics*, Vol. 52, No. 9, pp. 1824–1828, 2013.

63. Lee, C., M. Jeon, M. Y. Jeon, J. Kim and C. Kim, "In Vitro Photoacoustic Measurement of Hemoglobin Oxygen Saturation Using a Single Pulsed Broadband Supercontinuum Laser Source", *Applied Optics*, Vol. 53, No. 18, pp. 3884–3889, 2014.

64. Shu, X., M. Bondu, B. Dong, A. Podoleanu, L. Leick and H. F. Zhang, "Single All-Fiber-Based Nanosecond-Pulsed Supercontinuum Source for Multispectral Photoacoustic Microscopy and Optical Coherence Tomography", *Optics Letters*, Vol. 41, No. 12, pp. 2743–2746, 2016.

65. Koeplinger, D., M. Liu and T. Buma, "Photoacoustic Microscopy with a Pulsed Multi-Color Source Based on Stimulated Raman Scattering", *Ultrasonics Symposium (IUS), 2011 IEEE International*, pp. 296–299, IEEE, 2011.

66. Loya, A. K., J. Dumas and T. Buma, "Photoacoustic Microscopy with a Tunable Source Based on Cascaded Stimulated Raman Scattering in a Large-Mode Area Photonic Crystal Fiber", *Ultrasonics Symposium (IUS), 2012 IEEE International*, pp. 1208–1211, IEEE, 2012.

67. Ferrari, M. R., J. L. Farland and T. Buma, "Photoacoustic Microscopy Using Four-Wave Mixing in a Multimode Fiber", *Ultrasonics Symposium (IUS), 2015 IEEE International*, pp. 1–4, IEEE, 2015.

68. Buma, T., B. C. Wilkinson and T. C. Sheehan, "Near-Infrared Spectroscopic Photoacoustic Microscopy Using a Multi-Color Fiber Laser Source", *Biomedical Optics Express*, Vol. 6, No. 8, pp. 2819–2829, 2015.

69. Liu, M. and T. Buma, "Wavelength Agile Photoacoustic Microscopy with a Photonic Crystal Fiber supercontinuum source", *Photons Plus Ultrasound: Imaging and Sensing 2011*, Vol. 7899, p. 789944, International Society for Optics and Photonics, 2011.

70. Bondu, M. M., C. D. Brooks, C. Jakobsen, K. Oakes, P. M. Moselund, L. Leick, O. Bang and A. Podoleanu, "High Energy Supercontinuum Sources Using Tapered Photonic Crystal Fibers for Multispectral Photoacoustic Microscopy", *Journal of Biomedical Optics*, Vol. 21, No. 6, p. 061005, 2016.

71. Hajireza, P., A. Forbrich and R. Zemp, "In-Vivo Functional Optical-Resolution Photoacoustic Microscopy with Stimulated Raman Scattering Fiber-Laser Source", *Biomedical Optics Express*, Vol. 5, No. 2, pp. 539–546, 2014.

72. Serebryannikov, E. and A. Zheltikov, "Supercontinuum Generation Through Cascaded Four-Wave Mixing in Photonic-Crystal Fibers: When Picoseconds Do It

Better", *Optics Communications*, Vol. 274, No. 2, pp. 433–440, 2007.

73. Dudley, J. M., G. Genty and S. Coen, "Supercontinuum Generation in Photonic Crystal Fiber", *Reviews of Modern Physics*, Vol. 78, No. 4, p. 1135, 2006.

74. Boucon, A., T. Sylvestre, K. P. Huy, J.-C. Beugnot, G. Mélin, H. Maillotte and J. M. Dudley, "Supercontinuum Generation by Nanosecond Dual-Pumping Near the Two Zero-Dispersion Wavelengths of a Photonic Crystal Fiber", *Optics Communications*, Vol. 284, No. 1, pp. 467–470, 2011.

75. Wadsworth, W. J., N. Joly, J. C. Knight, T. A. Birks, F. Biancalana and P. S. J. Russell, "Supercontinuum and Four-Wave Mixing with Q-switched Pulses in Endlessly Single-Mode Photonic Crystal Fibres", *Optics Express*, Vol. 12, No. 2, pp. 299–309, 2004.

76. Dudley, J. M., L. Provino, N. Grossard, H. Maillotte, R. S. Windeler, B. J. Eggleton and S. Coen, "Supercontinuum Generation in Air–Silica Microstructured Fibers with Nanosecond and Femtosecond Pulse Pumping", *JOSA B*, Vol. 19, No. 4, pp. 765–771, 2002.

77. Shi, W., P. Hajireza, P. Shao, A. Forbrich and R. J. Zemp, "In Vivo Near-Realtime Volumetric Optical-Resolution Photoacoustic Microscopy Using a High-Repetition-Rate Nanosecond Fiber-Laser", *Optics Express*, Vol. 19, No. 18, pp. 17143–17150, 2011.

78. Shi, W., P. Shao, P. Hajireza, A. Forbrich and R. J. Zemp, "In Vivo Dynamic Process Imaging Using Real-Time Optical-Resolution Photoacoustic Microscopy", *Journal of Biomedical Optics*, Vol. 18, No. 2, p. 026001, 2013.

79. Hajireza, P., W. Shi and R. Zemp, "Label-Free In Vivo Fiber-Based Optical-Resolution Photoacoustic Microscopy", *Optics Letters*, Vol. 36, No. 20, pp. 4107–4109, 2011.

80. Shi, W., S. M. Kerr, I. A. Utkin, J. C. Ranasinghesagara, L. Pan, Y. B. Godwal, R. J. Zemp and R. Fedosejevs, "Optical Resolution Photoacoustic Microscopy Using Novel High-Repetition-Rate Passively Q-switched Microchip and Fiber Lasers", *Journal of Biomedical Optics*, Vol. 15, No. 5, p. 056017, 2010.

81. Wang, Y., K. I. Maslov, Y. Zhang, S. Hu, L.-M. Yang, Y. Xia, J. Liu and L. V. Wang, "Fiber-Laser-Based Photoacoustic Microscopy and Melanoma Cell Detection", *Journal of Biomedical Optics*, Vol. 16, No. 1, p. 011014, 2011.

82. Nedosekin, D. A., M. Sarimollaoglu, E. V. Shashkov, E. I. Galanzha and V. P. Zharov, "Ultra-Fast Photoacoustic Flow Cytometry with a 0.5 MHz Pulse Repetition Rate Nanosecond Laser", *Optics Express*, Vol. 18, No. 8, pp. 8605–8620, 2010.

83. Piao, Z., L. Zeng, Z. Chen and C.-S. Kim, "Q-switched Erbium-doped Fiber Laser at 1600 nm for Photoacoustic Imaging application", *Applied Physics Letters*, Vol. 108, No. 14, p. 143701, 2016.

84. Hajireza, P., A. Forbrich, Y. Jiang, W. Shi and R. Zemp, "In Vivo Multi-Wavelength Optical-Resolution Photoacoustic Microscopy with Stimulated Raman Scattering Fiber-Laser Source", *Photons Plus Ultrasound: Imaging and Sensing 2013*, Vol. 8581, p. 858129, International Society for Optics and Photonics, 2013.

85. Hajireza, P., A. Forbrich and R. J. Zemp, "Multifocus Optical-Resolution Photoacoustic Microscopy Using Stimulated Raman Scattering and Chromatic Aberration", *Optics Letters*, Vol. 38, No. 15, pp. 2711–2713, 2013.

86. Allen, T., M. Berendt, J. Spurrell, S. Alam, E. Zhang, D. Richardson and P. Beard, "Novel Fibre Lasers as Excitation Sources for Photoacoustic Tomography and Microscopy", *Photons Plus Ultrasound: Imaging and Sensing 2016*, Vol. 9708, p. 97080W, International Society for Optics and Photonics, 2016.

87. Mahmud, M. S., A. Forbrich, P. Shao, W. Shi and R. J. Zemp, "A Tunable MOPA Laser for Real-Time Optical Resolution Photoacoustic Microscopy", *Photons Plus Ultrasound: Imaging and Sensing 2015*, Vol. 9323, p. 93233V, International Society for Optics and Photonics, 2015.

88. Chen, H., S. Chen, J. Wang, Z. Chen and J. Hou, "35 W High Power All Fiber Supercontinuum Generation in PCF with Picosecond MOPA Laser", *Optics Communications*, Vol. 284, No. 23, pp. 5484–5487, 2011.

89. Ilday, F. Ö., H. Lim, J. Buckley and F. Wise, "Practical All-Fiber Source of High-Power, 120-fs Pulses at 1 μm", *Optics Letters*, Vol. 28, No. 15, pp. 1362–1364, 2003.

90. Diebold, G., T. Sun and M. Khan, "Photoacoustic Monopole Radiation in One, Two, and Three Dimensions", *Physical Review Letters*, Vol. 67, No. 24, p. 3384, 1991.

91. Erkol, H. and M. B. Unlu, "Spectral Power Density of the Random Excitation for the Photoacoustic Wave Equation", *AIP Advances*, Vol. 4, No. 9, p. 097103, 2014.

92. Erkol, H., E. Aytac-Kipergil and M. B. Unlu, "Photoacoustic Radiation Force on a Microbubble", *Physical Review E*, Vol. 90, No. 2, p. 023001, 2014.

93. Gusev, V. and A. Karabutov, "Laser Optoacoustics AIP", *New York*, p. 304, 1993.

94. Xu, M. and L. V. Wang, "Photoacoustic Imaging in Biomedicine", *Review of Scientific Instruments*, Vol. 77, No. 4, p. 041101, 2006.

95. Hoelen, C. and F. De Mul, "A New Theoretical Approach to Photoacoustic Signal Generation", *The Journal of the Acoustical Society of America*, Vol. 106, No. 2, pp. 695–706, 1999.

96. Yao, D.-K., K. Maslov, K. K. Shung, Q. Zhou and L. V. Wang, "In Vivo Label-Free Photoacoustic Microscopy of Cell Nuclei by Excitation of DNA and RNA", *Optics Letters*, Vol. 35, No. 24, pp. 4139–4141, 2010.

97. Yao, D.-K., R. Chen, K. Maslov, Q. Zhou and L. V. Wang, "In Vivo Imaging of Cell Nuclei by Photoacoustic Microscopy Without Staining", *Photons Plus Ultrasound: Imaging and Sensing 2012*, Vol. 8223, p. 82231X, International Society for Optics and Photonics, 2012.

98. Maker, P., R. Terhune, M. Nisenoff and C. Savage, "Effects of Dispersion and Focusing on the Production of Optical Harmonics", *Physical Review Letters*, Vol. 8, No. 1, p. 21, 1962.

99. Eckardt, R. and J. Reintjes, "Phase Matching Limitations of High Efficiency Second Harmonic Generation", *IEEE Journal of Quantum Electronics*, Vol. 20, No. 10, pp. 1178–1187, 1984.

100. Møller, U., S. T. Sørensen, C. Larsen, P. M. Moselund, C. Jakobsen, J. Johansen, C. L. Thomsen and O. Bang, "Optimum PCF tapers for blue-enhanced supercontinuum sources", *Optical fiber technology*, Vol. 18, No. 5, pp. 304–314, 2012.

101. Stone, J. M. and J. C. Knight, "Visibly "white" light generation in uniform photonic crystal fiber using a microchip laser", *Optics express*, Vol. 16, No. 4, pp. 2670–2675, 2008.

102. Sørensen, S. T., U. Møller, C. Larsen, P. Moselund, C. Jakobsen, J. Johansen, T. Andersen, C. Thomsen and O. Bang, "Deep-blue supercontinnum sources with optimum taper profiles–verification of GAM", *Optics express*, Vol. 20, No. 10, pp. 10635–10645, 2012.

103. Niermann, B., I. Budunoğlu, K. Gürel, M. Böke, F. Ö. Ilday and J. Winter, "Application of a mode-locked fiber laser for highly time resolved broadband absorption spectroscopy and laser-assisted breakdown on micro-plasmas", *Journal*

of physics D: Applied physics, Vol. 45, No. 24, p. 245202, 2012.

104. Jiang, W., E. Papa, H. Fischer, S. Mardyani and W. C. Chan, "Semiconductor Quantum Dots as Contrast Agents for Whole Animal Imaging", *TRENDS in Biotechnology*, Vol. 22, No. 12, pp. 607–609, 2004.

105. Michalet, X., F. Pinaud, L. Bentolila, J. Tsay, S. Doose, J. Li, G. Sundaresan, A. Wu, S. Gambhir and S. Weiss, "Quantum Dots for Live Cells, In Vivo Imaging, and Diagnostics", *Science*, Vol. 307, No. 5709, pp. 538–544, 2005.

106. Rhyner, M. N., A. M. Smith, X. Gao, H. Mao, L. Yang and S. Nie, "Quantum Dots and Multifunctional Nanoparticles: New Contrast Agents for Tumor Imaging", , 2006.

107. Shashkov, E. V., M. Everts, E. I. Galanzha and V. P. Zharov, "Quantum Dots as Multimodal Photoacoustic and Photothermal Contrast Agents", *Nano Letters*, Vol. 8, No. 11, pp. 3953–3958, 2008.

108. Mallidi, S., G. P. Luke and S. Emelianov, "Photoacoustic Imaging in Cancer Detection, Diagnosis, and Treatment Guidance", *Trends in Biotechnology*, Vol. 29, No. 5, pp. 213–221, 2011.

109. Avigo, C., N. Di Lascio, P. Armanetti, C. Kusmic, L. Cavigli, F. Ratto, S. Meucci, C. Masciullo, M. Cecchini, R. Pini *et al.*, "Organosilicon phantom for photoacoustic imaging", *Journal of biomedical optics*, Vol. 20, No. 4, p. 046008, 2015.

110. Strohm, E. M., M. C. Kolios, D. K. Hwang, B.-U. Moon and S. S. Tsai, "Development of a microfluidic device with integrated high frequency ultrasound probe for particle characterization", *Ultrasonics Symposium (IUS), 2014 IEEE International*, pp. 1960–1963, IEEE, 2014.

111. Avigo, C., P. Armanetti, C. Masciullo, N. Di Lascio, L. Cavigli, F. Ratto, R. Pini, M. Cecchini, C. Kusmic, F. Faita *et al.*, "Novel Organosilicon Phantoms as Testing

Material for Photoacoustic Imaging", *Design and Quality for Biomedical Technologies IX*, Vol. 9700, p. 97000I, International Society for Optics and Photonics, 2016.

112. Strohm, E. M., E. S. Berndl and M. C. Kolios, "Probing Red Blood Cell Morphology Using High-Frequency Photoacoustics", *Biophysical Journal*, Vol. 105, No. 1, pp. 59–67, 2013.

113. Strohm, E. M., M. J. Moore and M. C. Kolios, "Single Cell Photoacoustic Microscopy: A Review", *IEEE Journal of Selected Topics in Quantum Electronics*, Vol. 22, No. 3, pp. 137–151, 2016.

114. Gao, N., D. Zhao, R. Jia and D. Liu, "Microcantilever Actuation by Laser Induced Photoacoustic Waves", *Scientific Reports*, Vol. 6, p. 19935, 2016.

115. Putman, C. A., K. O. Van der Werf, B. G. De Grooth, N. F. Van Hulst and J. Greve, "Tapping mode atomic force microscopy in liquid", *Applied physics letters*, Vol. 64, No. 18, pp. 2454–2456, 1994.

116. Minne, S., S. Manalis and C. Quate, "Parallel atomic force microscopy using cantilevers with integrated piezoresistive sensors and integrated piezoelectric actuators", *Applied Physics Letters*, Vol. 67, No. 26, pp. 3918–3920, 1995.

117. Huefner, M., A. Pivonka, J. Kim, C. Ye, M. A. Blood-Forsythe, M. Zech and J. E. Hoffman, "Microcantilever Q Control via Capacitive Coupling", *Applied Physics Letters*, Vol. 101, No. 17, p. 173110, 2012.

118. Schäffer, T., J. Cleveland, F. Ohnesorge, D. Walters and P. Hansma, "Studies of Vibrating Atomic Force Microscope Cantilevers in Liquid", *Journal of Applied Physics*, Vol. 80, No. 7, pp. 3622–3627, 1996.

119. Carrasco, C., P. Ares, P. de Pablo and J. Gómez-Herrero, "Cutting Down the Forest of Peaks in Acoustic Dynamic Atomic Force Microscopy in Liquid", *Review*

of Scientific Instruments, Vol. 79, No. 12, p. 126106, 2008.

120. Pini, V., B. Tiribilli, C. M. C. Gambi and M. Vassalli, "Dynamical Characterization of Vibrating AFM Cantilevers Forced by Photothermal Excitation", *Physical Review B*, Vol. 81, No. 5, p. 054302, 2010.

121. Yamashita, H., N. Kodera, A. Miyagi, T. Uchihashi, D. Yamamoto and T. Ando, "Tip-Sample Distance Control Using Photothermal Actuation of a Small Cantilever for High-Speed Atomic Force Microscopy", *Review of Scientific Instruments*, Vol. 78, No. 8, p. 083702, 2007.

122. Ilic, B., S. Krylov and H. G. Craighead, "Theoretical and Experimental Investigation of Optically Driven Nanoelectromechanical Oscillators", *Journal of Applied Physics*, Vol. 107, No. 3, p. 034311, 2010.

123. Umeda, K.-i., N. Oyabu, K. Kobayashi, Y. Hirata, K. Matsushige and H. Yamada, "High-Resolution Frequency-Modulation Atomic Force Microscopy in Liquids Using Electrostatic Excitation Method", *Applied Physics Express*, Vol. 3, No. 6, p. 065205, 2010.

124. Herruzo, E. T. and R. Garcia, "Frequency Response of an Atomic Force Microscope in Liquids and Air: Magnetic versus Acoustic Excitation", *Applied Physics Letters*, Vol. 91, No. 14, p. 143113, 2007.

125. Michels, T. and I. W. Rangelow, "Review of Scanning Probe Micromachining and its Applications Within Nanoscience", *Microelectronic Engineering*, Vol. 126, pp. 191–203, 2014.

126. Onaran, A. G., F. L. Degertekin, B. Hadimioglu, T. Sulchek and C. Quate, "Actuation of Atomic Force Microscope Cantilevers by Acoustic Radiation Pressure", *Ultrasonics Symposium, 2001 IEEE*, Vol. 1, pp. 509–512, IEEE, 2001.

127. Huber, T. M., B. C. Abell, D. C. Mellema, M. Spletzer and A. Raman, "Mode-

Selective Noncontact Excitation of Microcantilevers and Microcantilever Arrays in Air Using the Ultrasound Radiation Force", *Applied Physics Letters*, Vol. 97, No. 21, p. 214101, 2010.

128. Degertekin, F., B. Hadimioglu, T. Sulchek and C. Quate, "Actuation and Characterization of Atomic Force Microscope Cantilevers in Fluids by Acoustic Radiation Pressure", *Applied Physics Letters*, Vol. 78, No. 11, pp. 1628–1630, 2001.

129. Kuusela, T. and J. Kauppinen, "Photoacoustic Gas Analysis Using Interferometric Cantilever Microphone", *Applied Spectroscopy Reviews*, Vol. 42, No. 5, pp. 443–474, 2007.

130. Koskinen, V., J. Fonsen, K. Roth and J. Kauppinen, "Progress in Cantilever Enhanced Photoacoustic Spectroscopy", *Vibrational Spectroscopy*, Vol. 48, No. 1, pp. 16–21, 2008.

131. Rakovskỳ, J. and O. Votava, "A Simple Photoacoustic Detector for Highly Corrosive Gases", *Review of Scientific Instruments*, Vol. 88, No. 1, p. 013103, 2017.

132. Demirkiran, A., A. Karakuzu, H. Erkol, H. Torun and M. B. Unlu, "Analysis of microcantilevers excited by pulsed-laser-induced photoacoustic waves", *Optics express*, Vol. 26, No. 4, pp. 4906–4919, 2018.

133. Stark, R. W. and W. M. Heckl, "Fourier Transformed Atomic Force Microscopy: Tapping Mode Atomic Force Microscopy Beyond the Hookian Approximation", *Surface Science*, Vol. 457, No. 1, pp. 219–228, 2000.

134. Garcia, R. and R. Perez, "Dynamic Atomic Force Microscopy Methods", *Surface Science Reports*, Vol. 47, No. 6, pp. 197–301, 2002.

135. Yaralioglu, G., A. Atalar, S. Manalis and C. Quate, "Analysis and Design of an Interdigital Cantilever as a Displacement Sensor", *Journal of Applied Physics*, Vol. 83, No. 12, pp. 7405–7415, 1998.

136. Rabe, U., K. Janser and W. Arnold, "Vibrations of Free and Surface-Coupled Atomic Force Microscope Cantilevers: Theory and Experiment", *Review of Scientific Instruments*, Vol. 67, No. 9, pp. 3281–3293, 1996.

137. Lindholm, U. S., D. D. Kana, W.-H. Chu and H. N. Abramson, "Elastic Vibration Characteristic of Cantilever Plates in Water", *Journal of Ship Research*, Vol. 9, No. 1, p. 50, 1962.

138. Sader, J. E., "Frequency Response of Cantilever Beams Immersed in Viscous Fluids with Applications to the Atomic Force Microscope", *Journal of Applied Physics*, Vol. 84, No. 1, pp. 64–76, 1998.

139. Maali, A., C. Hurth, R. Boisgard, C. Jai, T. Cohen-Bouhacina and J.-P. Aimé, "Hydrodynamics of Oscillating Atomic Force Microscopy Cantilevers in Viscous Fluids", *Journal of Applied Physics*, Vol. 97, No. 7, p. 074907, 2005.

140. Hopcroft, M. A., W. D. Nix and T. W. Kenny, "What is the Young's Modulus of Silicon?", *Journal of Microelectromechanical Systems*, Vol. 19, No. 2, pp. 229–238, 2010.

141. Pierron, O., C. Abnet and C. Muhlstein, "Methodology for Low-and High-Cycle Fatigue Characterization with kHz-Frequency Resonators", *Sensors and Actuators A: Physical*, Vol. 128, No. 1, pp. 140–150, 2006.

142. Sun, J. and B. S. Gerstman, "Photoacoustic Generation for a Spherical Absorber with Impedance Mismatch with the Surrounding Media", *Physical Review E*, Vol. 59, No. 5, p. 5772, 1999.

143. Kolkman, R. G., E. Blomme, T. Cool, M. Bilcke, T. G. van Leeuwen, W. Steenbergen, K. A. Grimbergen and G. J. den Heeten, "Feasibility of Noncontact Piezoelectric Detection of Photoacoustic Signals in Tissue-Mimicking Phantoms", *Journal of Biomedical Optics*, Vol. 15, No. 5, p. 055011, 2010.

144. Hochreiner, A., J. Bauer-Marschallinger, P. Burgholzer, B. Jakoby and T. Berer, "Non-Contact Photoacoustic Imaging Using a Fiber Based Interferometer with Optical Amplification", *Biomedical Optics Express*, Vol. 4, No. 11, pp. 2322–2331, 2013.

145. Rousseau, G., A. Blouin and J.-P. Monchalin, "Non-Contact Photoacoustic Tomography and Ultrasonography for Tissue Imaging", *Biomedical Optics Express*, Vol. 3, No. 1, pp. 16–25, 2012.

146. Kim, K. H., W. Luo, C. Zhang, C. Tian, L. J. Guo, X. Wang and X. Fan, "Air-Coupled Ultrasound Detection Using Capillary-Based Optical Ring Resonators", *Scientific Reports*, Vol. 7, No. 1, p. 109, 2017.

147. Meier, S. R., M. L. Korwin and C. I. Merzbacher, "Carbon Aerogel: a New Nonreflective Material for the Infrared", *Applied Optics*, Vol. 39, No. 22, pp. 3940–3944, 2000.

148. Fu, T., J. Tang, K. Chen and F. Zhang, "Visible, Near-Infrared and Infrared Optical Properties of Silica Aerogels", *Infrared Physics & Technology*, Vol. 71, pp. 121–126, 2015.

149. Gerlach, R., O. Kraus, J. Fricke, P.-C. Eccardt, N. Kroemer and V. Magori, "Modified SiO2 Aerogels as Acoustic Impedance Matching Layers in Ultrasonic Devices", *Journal of Non-Crystalline Solids*, Vol. 145, pp. 227–232, 1992.

150. Álvarez-Arenas, T. G., "Acoustic Impedance Matching of Piezoelectric Transducers to the Air", *IEEE Transactions on Ultrasonics, Ferroelectrics, and Frequency Control*, Vol. 51, No. 5, pp. 624–633, 2004.

151. Liu, Y., H. Miao, V. Aksyuk and K. Srinivasan, "Wide Cantilever Stiffness Range Cavity Optomechanical Sensors for Atomic Force Microscopy", *Optics Express*, Vol. 20, No. 16, pp. 18268–18280, 2012.

152. Sevim, S., N. Shamsudhin, S. Ozer, L. Feng, A. Fakhraee, O. Ergeneman, S. Pané, B. J. Nelson and H. Torun, "An Atomic Force Microscope with Dual Actuation Capability for Biomolecular Experiments", *Scientific Reports*, Vol. 6, p. 27567, 2016.